Enzymatic Carboxylation of Resorcinol in Aqueous Triethanolamine: First Steps Towards a Lab-Scale Production Process

Vom Promotionsausschuss der
Technischen Universität Hamburg
Zur Erlangung des akademischen Grades

Doktor der Naturwissenschaften (Dr. rer. nat.)

genehmigte Dissertation

von
Daniel Ohde

aus
Berlin

2022

1. Gutachter: Prof. Dr. rer. nat. Andreas Liese

2. Gutachter: Prof. Dr.-Ing. Michael Schlüter

Vorsitzender: Prof. Dr.-Ing. habil. Dr. h.c. Stefan Heinrich

Tag der mündlichen Prüfung: 10.12.2021

DOI: https://doi.org/10.15480/882.4115

Daniel Ohde, ORCID iD: https://orcid.org/0000-0002-5482-3534

Abstract

Carbon dioxide is crucial for life on earth as it is an integral part of a vast number of biological processes. In these processes, enzymes such as carboxylases, decarboxylases and oxidoreductases are used to integrate CO_2 into various substrates. In particular, some decarboxylases are able to form C-C bonds using CO_2 as C1 substrate without any cofactors. Especially, their ability to selectively carboxylate complex substrates makes these enzymes valuable for production of chemicals in industrial processes. However, for making these biotransformations able to compete with conventional chemical processes, several limitations need to be overcome. In this work, primarily strategies are investigated to overcome severely limited reaction yields. For that, the carboxylation of resorcinol to 2,6-dihydroxybenzoic acid (DHBA) by the enzyme 2,6-DHBA decarboxylase from *Rhizobium* sp. is chosen as model reaction system. This reaction is limited by a low conversion of the phenolic substrate due to the high thermodynamic stability of CO_2 and HCO_3^-, respectively. It is shown that this biotransformation can be combined and improved with an amine-based carbon capture technology. Triethanolamine (TEA) being a tertiary amine and the model solvent of this work, absorbs gaseous CO_2 achieving high dissolved inorganic carbon concentrations in aqueous solutions. This property is beneficial to achieve a high C1 substrate concentration for the enzymatic carboxylation pushing the reaction equilibrium in favor of the carboxylation instead of the decarboxylation. The reaction system is characterized in detail, achieving new insights into the reaction mechanism. Furthermore, a concept of a process is developed to obtain 2,6-DHBA in high purity from the biotransformation while recycling the applied solvents.

Correlation of the theoretical CO_2 loading of aqueous TEA revealed the reaction yield to be dependent on the achieved dissolved inorganic carbon concentration in the reaction medium. In combination with kinetic investigations, the active C1 substrate is revealed. Different strategies to enhance the reaction yield are explored with varying degree of success including the application of CO_2 pressure, *in situ* product crystallization and *in situ* product removal. In the process, an enzyme inhibition at high dissolved inorganic carbon concentrations is revealed. Overall, the finding of a suitable product adsorber for *in situ* product removal enabled reaction yields above 80%. The adsorber was characterized in detail and showed competitive adsorption of the phenolic substrate slowing the reaction and reducing the overall productivity. Nevertheless, an easy downstream process to obtain 2,6-DHBA in a purity above

99.8% was established, in which solvents including triethanolamine are recyclable for reuse.

A first 3 l lab-scale process was performed with the adsorber giving insights into the feasibly of a biocatalytic process to produce carboxylated phenols. In the process, microbubble gassing was applied for the absorption of CO_2 in the TEA-based reaction medium, which improved the mass transfer rate and efficiency of the saturation process reducing the waste of unreacted CO_2 and related costs. The liquid properties of TEA enabled easy production of bubbles in the micrometer scale increasing the surface to volume ratio. This is shown to improve the mass transfer and to reduce foaming. Furthermore, reaching a bubble diameter below 100 µm results in a rapid bubble dissolution assisted by enhanced Laplace pressure, which was demonstrated with bubble size distribution measurements and mass transfer simulations. At the same time, an active CO_2 gassing during the biotransformation was shown to influence the productivity dependent on the rate of surface area generation.

The gained insights into the amine-based enzymatic carboxylation helps to promote the applicability of this process getting closer to competing with the current state of the art chemical Kolbe-Schmitt process to produce carboxylated phenolic compounds.

Kurzfassung

Kohlenstoffdioxid bildet das Rückgrat für das Leben auf der Erde, weil CO_2 ein integraler Bestandteil vieler biologischer Prozesse, wie der Photosynthese ist. Enzyme, wie Carboxylasen, Decarboxylasen und Oxidoreduktasen werden in diesen Reaktionen genutzt, um CO_2 in verschiedene Substrate zu fixieren. Einige Decarboxylasen haben die Besonderheit, dass diese C-C-Verbindungen ohne Kofaktoren und nur mit CO_2 als C1-Substrat katalysieren können. Diese Eigenschaft und die Fähigkeit auch komplexe Substrate selektiv zu carboxylieren, macht diese Enzyme wertvoll zur Produktion von Chemikalien im industriellen Maßstab. Bevor diese Biotransformation gegenüber den konventionellen chemischen Verfahren konkurrenzfähig werden, müssen einige Limitationen überwunden werden. In dieser Arbeit werden vorrangig verschiedene Strategien aufgezeigt, um bisher stark limitierte Reaktionsausbeuten zu steigern. Es wurde die Carboxylierung von Resorcinol zu 2,6-Dihydroxybenzoesäure (DHBA) durch das Enzym 2,6-DHBA Decarboxylase als Modellsystem bearbeitet. In dieser Reaktion können nur geringe Substratumsätze erzielt werden, da das C1 Substrat, CO_2 oder Bicarbonat, eine hohe thermodynamischen Stabilität aufweist. Es wird gezeigt, dass diese Biotransformation mit der Technologie der CO_2-Abscheidung durch Nutzung von Aminen kombiniert und verbessert werden kann. Für die Untersuchungen wurde das tertiäre Amin Triethanolamin (TEA) ausgewählt. TEA absorbiert CO_2, wodurch hohe Konzentrationen an gelösten CO_2 Spezies in wässrigen Lösungen erzielt werden. Somit werden hohe Konzentration des C1 Substrates ermöglicht. Dadurch wird das Reaktionsgleichgewicht in Richtung der Carboxylierung verschoben. Das gesamte Reaktionssystem wurde charakterisiert und neue Erkenntnisse, vor allem im Bezug zum Reaktionsmechanismus, gewonnen. Des Weiteren wurde ein Konzept für einen Prozess erarbeitet, um biokatalytisch produziertes 2,6-DHBA in hoher Reinheit zu gewinnen, bei gleichzeitiger Ermöglichung der Rezyklierung von Lösungsmitteln.

Die Korrelation der theoretischen CO_2-Beladung von wässrigen TEA Lösungen zeigt, dass die Reaktionsausbeute von der Konzentration von gelöstem anorganischem Kohlenstoff im Reaktionsmedium abhängt. Weiterhin konnte das aktive C1 Substrat mit diesen, aber auch Ergebnissen von kinetischen Untersuchungen identifiziert werden. Zur Steigerung der Ausbeute wurden verschiedene Strategien mit unterschiedlichem Erfolg untersucht, inklusive Erhöhung des CO_2 Drucks, *in situ* Produktkristallisation und *in situ* Produktisolierung durch Adsorption. Bei den Untersuchungen zeigte sich, dass die Aktivität des Enzyms bei hohen gelösten CO_2 Konzentrationen abnimmt ähnlich einer Inhibierung.

Schließlich wurde ein Adsorber gefunden, der sich zur *in situ* Produktentfernung eignet. So konnte die Reaktionsausbeute auf über 80% gesteigert werden. Die Charakterisierung dieses Adsorbers zeigte, dass auch Substrat gebunden wird, wodurch sich die Reaktion verlangsamt und die Produktivität sinkt. Mit diesem Adsorber war es möglich ein Verfahren zur einfachen Produktisolierung zu entwickeln, mit dem Produktreinheiten über 99,8% erzielt wurden. Weiterhin konnte gezeigt werden, dass die verwendeten Lösungsmittel, inklusive TEA, wiederverwendet werden können.

Eine erste Maßstabsvergrößerung des Prozesses in einem 3 l Reaktor wurde durchgeführt, bei dem die Anwendbarkeit des Adsorbers und der enzymatischen Carboxylierung von Phenolen im Allgemeinen bemessen wurden. Die Implementierung einer Mikroblasenbegasung zur Absorption von CO_2 in wässrigen TEA Lösungen verbesserte die Stoffübergangsrate und die Effizienz des Einlösens von CO_2. Das steigerte die Nutzung von CO_2 durch Verringerung des Anteiles von sich nicht eingelösten CO_2 im Gasstrom, was wiederum Kosten reduziert. Die Stoffeigenschaften von TEA begünstigen die Erzeugung von Blasen im Mikrometerbereich. Es konnte gezeigt werden, dass die erhöhte spezifische Oberfläche von Mikroblasen und das beschleunigte Einlösen durch den steigenden LaPlace-Druck den hohen Massentransport verursacht und dadurch die Schaumbildung minimiert. Dazu dienten Messungen der Blasengrößenverteilung, Massentransportraten und Simulationen des Massentransportes. In Versuchen mit einer aktiven CO_2 Begasung war die Produktivität zudem abhängig von der Generierungsrate der Gas-Flüssig-Oberfläche.

Die erzielten Erkenntnisse bringen die enzymatische Carboxylierung, kombiniert mit Aminen, näher zu einer industriellen Umsetzung. Dabei ist noch ausstehend, ob der Prozess mit der etablierten chemischen Carboxylierung von Phenolen, dem Kolbe-Schmitt Prozess, konkurrieren kann.

Contents

List of Used Abbreviations and Symbols

Abbreviations

‘CO_2’	CO_2 and H_2CO_3
2,3-DHBD	2,3-dihydroxybenzoic acid decarboxylase
2,3-DHBA	2,3-dihydroxybenzoic acid
2,6-DHBA	2,6-dihydroxybenzoic acid
2,6-DHBD	2,6-dihydroxybenzoic acid decarboxylase
BSD	bubble size distribution
CFE	cell-free extract
CV	column volume
DIC	dissolved inorganic carbon concentration
FDH	formate dehydrogenase
KdcA	branched-chain α-keto acid decarboxylase
LDH	lactate dehydrogenase
LeuDH	leucine dehydrogenase
MTOB	4-methylthio-2-oxobutanoate
ICD	indole-3-carboxylate decarboxylase
PAD	phenolic acid decarboxylase
PCD	pyrrole-2-carboxylate decarboxylase
PDC	pyruvate
RCF	relative centrifugal force
SCTE	standard CO_2 transfer efficiency
SGTE	standard gas transfer rate
SGTR	standard gas transfer rate
SOTE	standard oxygen transfer efficiency
SOTR	standard oxygen transfer rates
SV	specific volume
TEA	triethanolamine
TFA	trifluoroacedic acid
Tris	tris(hydroxymethyl)aminomethane
TBA-Br	tetrabutylammonium bromide

Symbols

a	$m^2\ m^{-3}$	specific surface area
$\dot{a}$	$m^2\ min^{-1}$	surface area generation rate
c^*	mM	gas saturation concentration
$k_L a$	h^{-1}	volumetric mass transfer coefficient
k_L	$m\ s^{-1}$	mass transfer coefficient
ε_G	-	gas hold-up
ε_F	-	foam hold-up
V_l	l	liquid volume
$\dot{w}_G$	$ml\ min^{-1}$	gassing rate
S	-	gas saturation

r	m	radius
K_{eq}	mM^{-1}	equilibrium constant
g	$m\ s^{-2}$	gravitational acceleration
$K_{M,i}$	mM	Michaelis-Menten constant of individual reactant i
v	$\mu mol\ min^{-1}\ mg^{-1}$	reaction rate
v_{max}	$\mu mol\ min^{-1}\ mg^{-1}$	maximum reaction rate
Q	$mol\ mol^{-1}$	CO_2 loading
Q_{max}	$mol\ mol^{-1}$	maximum CO_2 loading
d_{32}	µm	Sauter mean diameter
v_B	$m\ s^{-1}$	bubble rising velocity
d_B	m	bubble diameter
h	m	reactor height
p	Pa	pressure
p_{atm}	Pa	atmospheric pressure
T	K	temperature
σ	$N\ m^{-1}$	surface tension
η	Pa s	dynamic viscosity
ρ	$kg\ m^{-3}$	density
H	$mol\ m^{-3}\ Pa^{-1}$	Henry’s constant
D	$m^2\ s^{-1}$	diffusion coefficient
q_i	$mol\ g^{-1}$	amount adsorbed on the surface
$q_{m,i}$	$mol\ g^{-1}$	maximum capacity of the adsorbant
b_i	-	isotherm parameter
c_i	mM	adsorbate concentration at equilibrium
d_i	-	isotherm parameter
n	-	isotherm exponent
m	-	isotherm exponent
K	-	Freundlich coefficients

1. Introduction

1.1. The Value of Carbon Dioxide

Carbon dioxide is a molecule of key importance as it is the main carbon source for life on Earth. Photosynthetic organisms like plants, algae and cyanobacteria continuously consume CO_2 and water to synthesize carbohydrates by utilization of light energy with oxygen being produced as waste product. In this way, energy-rich organic compounds are produced, which are metabolized by aerobic organisms in respiration to provide them with energy. In nature, the concentration of atmospheric CO_2 is generally regulated by photosynthetic organisms and geological phenomena. Geological phenomena include, among others volcanos as natural sources of CO_2, carbonate rocks and water, where CO_2 is dissolved. At 25 °C and 1 atm, CO_2 dissolves with a solubility of 32.9 mM in water [1]. This high solubility leads to the majority of CO_2 being stored in water sources such as saltwater, groundwater and ice. In water, dissolved CO_2 forms H_2CO_3 (Eq. 1). Carbonic acid is a double proton acid, which is in equilibrium with HCO_3^- (Eq. 2) having a theoretical pKa of 3.6. However, experimental determination of aqueous CO_2 and H_2CO_3 concentration is difficult. For that reason both equilibria, Eq. 1 and Eq. 2 are combined to Eq. 3, which gives the experimentally determinable pKa of 6.5. In a further equilibrium, HCO_3^- dissociates to CO_3^{2-} according to Eq. 4 having a pKa of 10.3.

$$CO_2 + H_2O \rightleftharpoons H_2CO_3 \qquad \text{Eq. 1}$$

$$H_2CO_3 + H_2O \rightleftharpoons HCO_3^- + H_3O^+ \qquad \text{Eq. 2}$$

$$CO_2 + 2\ H_2O \rightleftharpoons HCO_3^- + H_3O^+ \qquad \text{Eq. 3}$$

$$HCO_3^- + H_2O \rightleftharpoons CO_3^{2-} + H_3O^+ \qquad \text{Eq. 4}$$

These CO_2 equilibria play a major role in maintaining stable pH values in various systems. In humans, the blood is buffered to a pH of around 7.4 [2]. At these rather neutral pH values, the majority of dissolved inorganic carbon is present as bicarbonate as illustrated in Figure 1. Sport activity leads to an increased metabolism, which increases CO_2 levels in the blood, which decreases the pH [3]. Prolonged disturbance of the pH balance causes health issues. Acidosis happens when body fluids contain too many acids, while alkalosis occurs at higher pH. In the ocean, the CO_2 buffer contributes to maintain a saltwater pH typically to a range between 7.5 and 8.4 [4]. It is expected that rising atmospheric CO_2 level leads to acidification of the ocean [5]. However, the oceanic system is complex as other factors contribute to the pH like temperature and mineral content. Disruption of this equilibrium has an impact on calcifying and non-calcifying organism present in the ocean. It is expected that the carbon fixation rates in some photosynthetic organisms increases, while broader implications for ocean ecosystems are not well understood, yet [5].

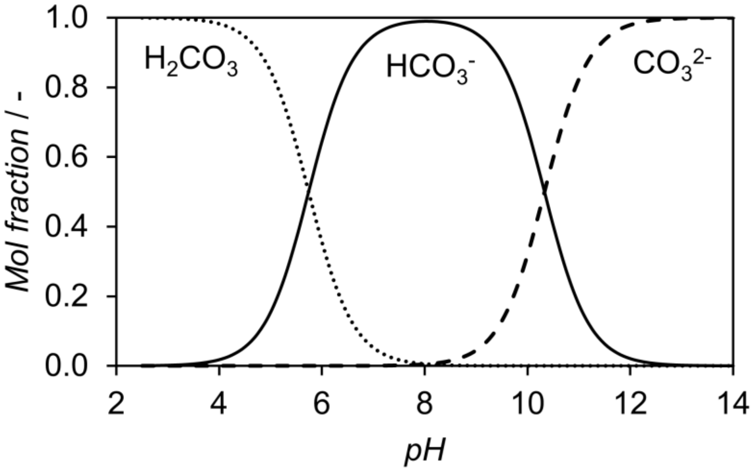

Figure 1: Distribution of aqueous CO_2 species.

Industrialization increased the CO_2 emissions and the importance of CO_2 further, especially in regard to industrial applications, environmental impact and society as a whole. Commonly known, CO_2 is used in the production of carbonated beverages such as soda water, beer and sparkling wine. However, several industrial processes exist that consume CO_2 for the production of chemicals [6]. Urea, which is primarily used as fertilizer was produced in an excess of 218 Mt/yr on global scale in 2019 [7].This utilized around 170 Mt/yr CO_2 as raw material [8]. In different processes, methanol is produced by dry reforming or CO_2 reforming of methane and hydrogenation of CO_2 [9]. However, most methanol is produced from natural gas or goal via a syngas production step. The global methanol production is expected to increase from 148 Mt/yr in 2019 to 311 Mt/yr by 2030 [10]. An increase in the methanol price from 400 €/t by factor of 1.8, an almost 2.5 times decrease in H_2 prices or CO_2 being priced at approximately 222 €/t would make the CO_2-based processes superior over the conventional syngas process [11], which demonstrates the enormous potential of CO_2-based processes. Even carboxylic acid derivates can be prepared in a mixture of CO_2 and a phenolic compound reacting at high pressure and temperature known as the Kolbe-Schmitt reaction [12]. A prominent carboxylic acid derivate that is produced in this way is salicylic acid, which is the precursor to Aspirin. Further processes that utilize CO_2 as raw material are capable of producing formic acid, polymers and a range of other products [6]. In a different application, liquid and solid CO_2 are used as important refrigerants. Solid CO_2, which is also known as dry ice, always has a temperature below −78.5 °C under atmospheric pressure independent of the surrounding air temperature. Furthermore, some fire extinguisher use CO_2, which work by displacing oxygen and starving of flames. CO_2 is even used as solvent in the form of supercritical CO_2 in different extraction processes, such as the decaffeination to remove caffeine from coffee [13]. Supercritical CO_2 forms in a certain elevated pressure and temperature range, where it behaves as a supercritical fluid adopting properties between a gas and a liquid.

Overall, CO_2 is increasingly used in various processes. However, CO_2 emissions simultaneously increase due to burning of fossil fuels to meet the increasing energy demand. Furthermore, other CO_2 emitting processes like the production of cement contribute and pose a risk to disturbing the carbon cycle. In particular, CO_2 is a greenhouse gas, which is directly linked to the global temperature. Since industrialization, CO_2 rapidly accumulates in the atmosphere as shown by regular measurements taken at Mauna Loa, Hawaii (Figure 2). Growing worldwide efforts are focusing on reducing greenhouse gas emission with the optimization of existing and developing technologies being targeted to reduce and recycle CO_2 [14,15]. Furthermore, the reduction of greenhouse gas emission is necessary to achieve the aims of the Paris Agreement from 2016 within the United Nations Framework Convention on Climate Change. Introduction of a market price for CO_2 is expected to promote the previously mentioned CO_2-based processes and dissuade from producing unnecessary CO_2 emission.

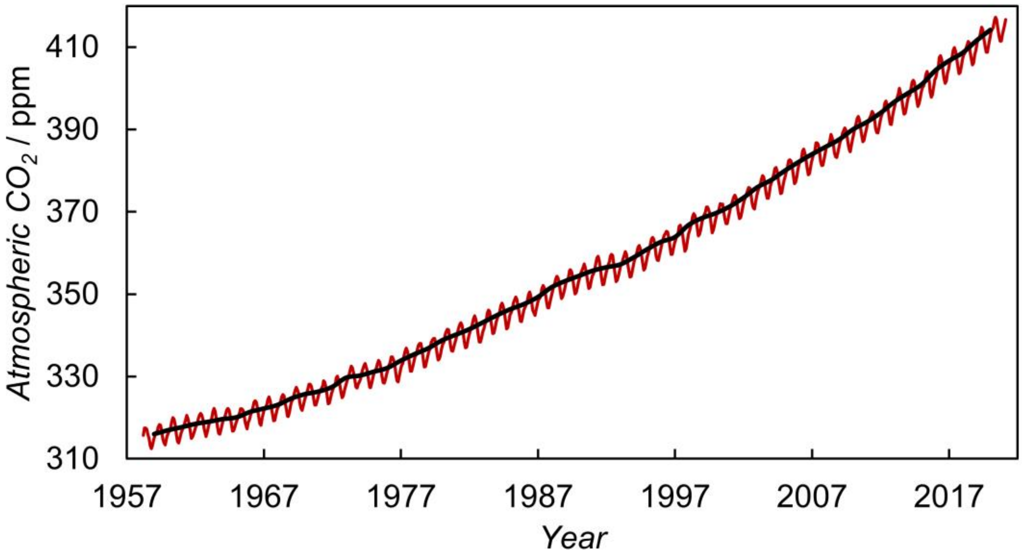

Figure 2: Monthly (red) and annual mean (black) atmospheric CO_2 measured at Mauna Loa Observatory. [16]

Already, the European Union introduced the European Union Emissions Trading System, where certificates are issued, which allow for a certain amount of CO_2 emission. These certificates can be traded and fines occur when CO_2 emissions exceed the allowance based on held certificates. This and similar systems are expected to promote the development of new alternative and green processes to replace fossil-based economies. Among other technologies, biocatalytic processes have a high potential to provide these qualities with recent research focusing on enzymatic carboxylation reactions.

1.2. Utilization of CO_2 for Chemical and Enzymatic Carboxylations

The most important carboxylation reaction is performed by ribulose-1,5-bisphosphat-carboxylase/-oxygenase, abbreviated to RuBisCO. RuBisCO is probably the most abundant enzyme on earth with an estimated total weight of 40 Mt, which correlates to around 5 kg /person [17]. It catalyzes the carboxylation of ribulose-1,5-bisphosphate, which is the first major step of carbon fixation in plants and other photosynthetic organisms. In this way, energy-rich molecules such as glucose are produced. In general, carboxylation can be described as an insertion of CO_2 in a C-H bond, which requires a heterolytic cleavage and carbanion formation. However, the proceeding of this type of reaction is limited due to the thermodynamic stability of CO_2 as it only has a standard Gibbs free energy of formation of -394 kJ mol^{-1} [18]. This low value of the starting material means that it will not react easily, which causes thermodynamic limitations. Furthermore, kinetic limitations arise for the decarboxylation through stabilization of the carbanion. In total, only redox transformations and redox neutral transformations can be performed as CO_2 has an oxidation state of +4. Enzymes perform redox transformations efficiently by using energy rich cofactors to activate substrates. In this way, CO_2 can be reduced to carbon monoxide, formate and methanol, among other products. In contrast, carboxylation represents a redox neutral transformation. In the same way as the redox transformations, carboxylation reactions in metabolic pathways evolved to utilize different strategies to make the biotransformation exergonic. For one, light is harnessed in photosynthetic organisms, which use this energy source to activate substrates to drive the carboxylation performed by RuBisCO. In contrast, redox equivalents such as NAD(P)H are directly used in the carboxylation. For example, the crotonoyl-CoA carboxylase catalyzes the reductive carboxylation of the aliphatic enoyl-CoA ester, crotonoyl-CoA to produce ethylmalonyl-CoA [19]. In the reductive reaction step, the transformation of NADPH to $NADP^+$ is exergonic and drives the otherwise unfavorable energonic carboxylation step [20]. In a similar way, a coupled hydrolysis of energy rich compounds such as adenosine triphosphate provides the thermodynamic driving force for substrate carboxylation. Prominent example are the adenosine triphosphate and biotin-dependent acetyl-CoA and propionyl-CoA carboxylase, which are key enzymes in the hydroxypropionate cycle of autotrophic CO_2 fixation to produce the intermediates malonyl-CoA and methylmalonyl-CoA, respectively [21]. In these reactions, CO_2 acts as electrophile. In contrast, bicarbonate acts as nucleophile due to an even higher thermodynamic stability with -600 kJ mol^{-1}. Still, reactions with bicarbonate can proceed through the specified energy supplementation mechanism. Supplementation of energy is essential to drive the carboxylation efficiently, which is also necessary in chemical carboxylation.

In the Kolbe-Schmitt process, CO_2 is used at high pressure and temperature to carboxylate various compounds [22]. It is a commercial process, but is limited by a lower selectivity compared to the enzymatic counterpart. Resorcinol is an important substrate for the chemical carboxylation as the produced derivates have a wide range of applications in agricultural, industrial and pharmaceutical processes [22]. Chemical carboxylation of resorcinol produces primarily mono- and dicarboxylated derivates. The required selectivity can be modulated to a certain extend by selection of suitable catalysts. For example, 2,6-dihydroxybenzoic acid (2,6-DHBA) can be synthesized under anhydrous condition with potassium carbonate in the presence of carbon dioxide and dimethyl formamide solvent [23,24].

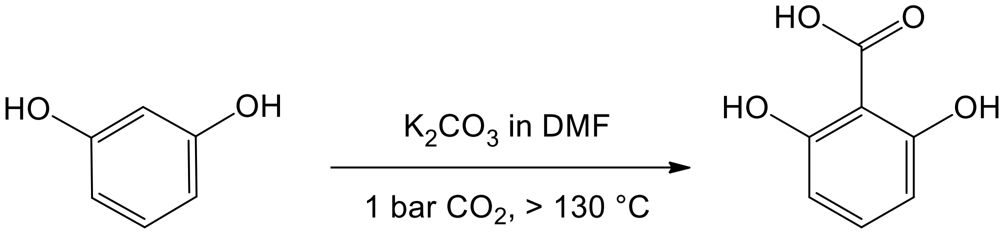

Figure 3: Chemical Carboxylation of resorcinol to yield 2,6-DHBA.

Alternatively, mixtures of 2,4-DHBA and 2,6-DHBA prepared from resorcinol can be treated to selectively decompose 2,4-DHBA to yield 2,6-DHBA in a high purity [25].

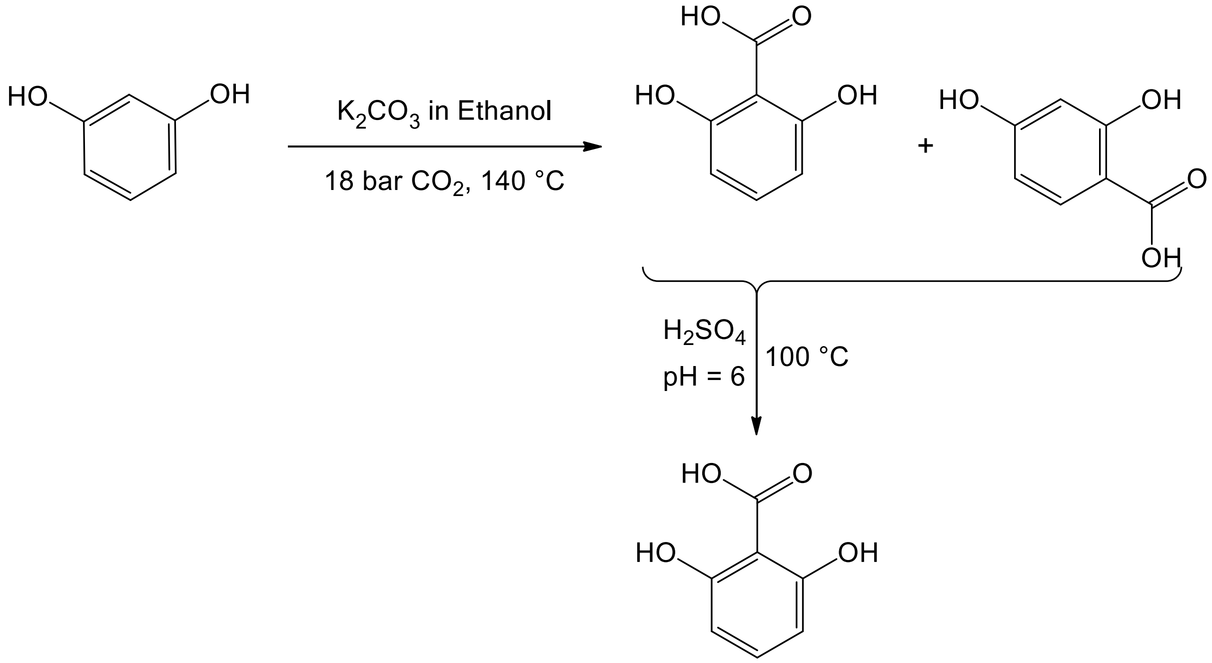

Figure 4: Chemical Carboxylation of resorcinol to yield a mixture of 2,4-DHBA and 2,6-DHBA, which is treated to selectively decompose 2,4-DHBA to yield pure 2,6-DHBA.

2,6-DHBA is used as valuable intermediate for a wide range of applications. This includes, among other processes, production of herbicide such as bispyribac [26], synthesis of anilides being used as therapeutics against parasites [27] and production of azo compounds for dying of polyesters [28]. In addition, 2,6-DHBA is used to synthesize lanthanide complexes, which have luminescent properties [29]. In summary, the global 2,6-DHBA market size was 4.2 billion USD in 2019 [30]. At the same time, the dihydroxybenzene (catechol, resorcinol, hydroquinone) market size was 9.4 billion USD in 2019 [31]. This demonstrates the value and need for carboxylation.

In contrast to the Kolbe-Schmitt process, which suffers from poor selectivity and needs to be performed at high temperatures and high CO_2 pressures [12], enzymes can perform these reactions at a much higher selectivity and under mild conditions. This makes the biocatalytic carboxylation of phenols the biological equivalent to the chemical Kolbe-Schmitt reaction, especially as both reactions proceed through the formation of intermediate enolates [32]. Several decarboxylases were found to catalyze the carboxylation even without any additional cofactors and prior activation step of the phenolic substrate. These enzymes are part of the lyase enzyme class and efficiently perform decarboxylation reactions in nature. Only some of these enzymes can perform reversible reactions. Therefore, these rare enzymes showing reversibility are often referred to as reversible decarboxylases, when primarily being used for carboxylation. The biocatalytic carboxylation has the potential to replace the chemical Kolbe-Schmitt process. Especially, the avoidance of harsh reaction conditions and the prevention of side product formation by achieving high regioselectivities [33] is desired. Furthermore, the generally increased interest in green and sustainable processes [34] as well as the growing concern for a rising atmospheric CO_2 level and climate change promotes research of green chemistry with several reversible decarboxylases being in the focus of recent research [35–37]. In green chemistry, toxic and/or hazardous reagents and solvents are avoided by utilization of raw and preferably renewable materials with the goal to eliminate waste in the manufacturing of chemical products [38]. In this regard, Anastas and Warner introduced the 12 principles of green chemistry in 1998 in their book Green Chemistry: Theory and Practice [39]. In Table 1, these principles are listed and associated with qualities of biocatalysis. Enzymes are biological catalysts that are produced from renewable resources and are biodegradable. Furthermore, they are essentially non-hazardous and non-toxic. At the same time, enzymatic reactions are generally performed in aqueous systems under mild conditions. They often only require ambient temperature and atmospheric pressure conditions. In addition, separate functional group activation, protection and deprotection steps are generally unnecessary due to their high selectivity. In turn, this generates less waste compared to conventional organic syntheses as more economical synthesis routes are possible.

Table 1: Biocatalysis and the 12 principles of green chemistry. [34]

	Green Chemistry Principles	**Biocatalysis**
1	Waste prevention	Significantly reduced waste
2	Atom economy	More atom and step economic routes
3	Less hazardous reactions	Generally low toxicity
4	Design for safer chemicals	-
5	Safer solvents and auxiliaries	Usually aqueous non-toxic systems
6	Energy efficiency	Mild conditions
7	Renewable feedstocks	Enzymes are renewable
8	Reduce derivatization	Avoids protection/deprotection steps
9	Catalysis	Enzymes are biological catalysts
10	Design for degradation	Not really relevant but enzymes themselves are biodegradable
11	Real-time analysis	Compatible with biocatalytic processes
12	Inherently safer chemistry	Safe conditions as enzymes perform efficient under mild conditions

This comparison demonstrates that biocatalysis is highly compatible with green chemistry and an integral part of achieving a more green and sustainable circular economy [40]. However, the drawback of utilization of biocatalysis is often that biocatalysts are unstable under the preferred reaction conditions and have limitations to achieve high conversions. Especially, for the enzymatic carboxylation, the unfavorable thermodynamic equilibrium strongly favors the decarboxylation over the carboxylation reaction due to the high thermodynamic stability of CO_2 and HCO_3^-. As a result, even at high C1 substrate concentration only a low conversion is possible. High C1 substrate concentrations can be achieved by application of CO_2 pressure as well as using carbonate salts in excess such as $KHCO_3$, which has a solubility of around 4 M at 30 °C [41]. However, even at 3 M aqueous $KHCO_3$, only 30% conversion of catechol to 2,3-DHBA is reported for the carboxylation by the 2,6-dihydroxybenzoic acid decarboxylase from *Rhizobium sp.* (2,6-DHBD) [35]. This corresponds to an equilibrium constant K_{eq} of $1.6*10^{-4}$ mM^{-1}. Generally, the equilibrium constant is calculated by Eq. 1, where equilibrium concentration of the product is divided by the equilibrium concentration of the substrates. In enzymatic carboxylation, there are two substrates, the C1 substrate and the 'main' substrate that gets carboxylated. In the case of using bicarbonate as C1 substrate, water as second product is produced.

$$K_{eq} = \frac{c_{product,\ eq}}{c_{substrate\ 1,\, eq} \cdot c_{substrate\ 2,\, eq}} \qquad \text{Eq. 5}$$

Usually, enzymes have activities not only for their natural substrate, but also molecules with a similar structure to the natural substrate that also fits into the binding pocket of the enzyme. For example, 2,6-DHBD accepts several substrates besides its natural substrate resorcinol such as catechol, 5-methylresorcinol, resveratrol, piceatannol and gnetol [42,43]. Depending on the substrate, different yields can be achieved. This is highlighted in the previous mentioned study, in which catechol carboxylation resulted in only 30% conversion, whereas resorcinol carboxylation was enhanced achieving a slightly higher conversion of 36% at 3 M aqueous $KHCO_3$ [44]. In contrast to using carbonate salts as C1 substrate source, different amines can be used due to their affinity for CO_2. Consequently, amines absorb CO_2 to provide the C1 substrate for the enzymatic carboxylation as already demonstrated by Pesci *et al.* (2017). They found that the application of different amines at an aqueous concentration of 1 M significantly increases the carboxylation conversion of catechol performed by 2,3-DHBD from *Aspergillus oryzae* compared to using 1 M $KHCO_3$ [45]. This shows the potential to combine enzymatic carboxylation with the CO_2 amine-mediation also known as amine-based carbon capture and amine scrubbing.

1.3. Amine-based Carbon Capture

CO_2 capture is the most mature industrial scale technology to counter the rising atmospheric CO_2 and reduce CO_2 emission.[46] Worldwide effort is expended to optimize existing and developing technologies making them more economical and reducing in that way CO_2 emissions, which is of major interest and required to achieve the pledges in the Paris Agreement[14,15]. The CO_2 capture technology is based on the chemical absorption of CO_2 out of exhaust gases and exhaled air in solvents. Especially, amines are in the focus of the research to further improve the CO_2 capture process. Amines have a high affinity to CO_2 and highly efficient amines as well as amine blends are utilized in industry[46]. Depending on the applied amine, CO_2 is absorbed via different mechanisms[47,48] (Figure 5). Primary and secondary amines first form a zwitterion (Figure 5 reaction 1), which undergoes deprotonation by a base to form a carbamate (Figure 5 reaction 2). However, in the case that the amine, which is also a base, is sterically hindered, the zwitterion reacts with water to form bicarbonate (Figure 5 reaction 3). Otherwise, the carbamate undergoes hydrolysis due to its low stability producing bicarbonate in the process (Figure 5 reaction 4). The sum of these reaction can represented as reaction 5 in Figure 5. In contrast to primary and secondary amines, tertiary amines produce carbonates directly via a base-catalyzed hydration mechanism without intermediate zwitterion and carbamate formation (Figure 5 reaction 6).

Zwitterion Formation

$$AmH + CO_2 \xrightleftharpoons{1} AmH^+COO^-$$

Carbamate Formation

$$AmH^+COO^- + B \xrightarrow{2} AmCOO^- + BH^+$$

Zwitterion Hydrolysis

$$AmH^+COO^- + H_2O \xrightarrow{3} AmH_2^+ + HCO_3^-$$

Carbamate Hydrolysis

$$AmCOO^- + H_2O \xrightarrow{4} AmH + HCO_3^-$$

Summary of the Zwitterion Mechanism

$$AmH + H_2O + CO_2 \xrightleftharpoons{5} AmH_2^+ + HCO_3^-$$

Base-Catalyzed Hydration Mechnism

$$R_3N + H_2O + CO_2 \xrightarrow{6} R_3N^+H + HCO_3^-$$

Figure 5: Reaction mechanisms of the CO_2 conversion to HCO_3^- by primary and secondary amines (reactions 1-5) as well as tertiary amines (reaction 6) in aqueous solution.

It is reported that tertiary amines can also directly react with CO_2 to from carbamates[49]. However, this mechanism only contributes to the CO_2 binding significantly at very high pH above 12[50]. Amines are alkaline by nature and these pH values are at most only achieved for a very short duration in highly concentrated amine solutions due CO_2 absorption, which lowers the pH by reacting with water (Eq. 1 - Eq. 4). Chemisorption of CO_2 can be performed in aqueous and non-aqueous solvents, which primarily affects the energy requirement for the solvent regeneration, where a large quantity of heat energy needs to be supplied to break the chemical bond between CO_2 and absorbent. In addition, the necessary sensible heat and latent heat of vaporization of solvents need to be considered [51]. In turn, this high energy requirement is the major technological barrier [52], which limits wide-scale implementation of CO_2 capture in large-scale applications. Adaption of CO_2 capture in coal-fired power plants reduces the electrical efficiency by about 9% for conventional solvents [53]. Typical solvent regeneration is performed at up to 120 °C [46] using the diminishing solubility of CO_2 in amines at increasing temperatures. Application of 30% aqueous monoethanolamine representing a conventional solvent has an energy requirement of about 4000 kJ/kg CO_2 due to additional energy being required for CO_2 stripping, pumps, blowers, etc. [54]. Therefore, current research focuses on improving the CO_2 absorption process and reducing the required temperature for the regeneration of the solvent [55–58].

Establishing an efficient CO_2 mass transfer has the potential to lower the energy requirement and, therefore, cost for blowers and pumps introducing the liquid and flue gas into the absorption column. Additionally, the amount of residual CO_2 emission in the exhaust gas can be reduced. The main factors to contribute to an efficient mass transfer are a direct gas-liquid phase contact, a large interfacial contact area and a sufficient contact time. Gas dispersion and residence time of gas bubbles is governed by the properties and operation of a multiphase reactor. Conventional bubbly flows utilize bubbles, which have diameter in the range of several millimeters. As a characteristic of their large size in relation to bubbles in the micrometer scale, they have a low volume specific surface and in consequence provide less interfacial contact area, resulting in slower volume-specific mass transfer rates. However, millimeter scale bubbles induce a buoyancy-driven flow causing a significant convection, which is beneficial for mixing. In comparison, bubbles in the micrometer scale generate much less convection as the bubble buoyancy is less dominant due to having rising velocities in the range of only several micrometer per second. As a result, the mass transfer is dominated by diffusion. In consequence of these different characteristics, microscale bubbles were classified according to their size in the ISO 20480-1, illustrated in Figure 6. Fine bubbles include ultrafine bubbles being in the nanoscale and microbubbles, which have a volume equivalent diameter in the range from 1 µm up to 100 µm. The remaining fraction of microscale bubbles can be called submillibubbles as they are just below millimeter scale bubbles (millibubbles) in size.

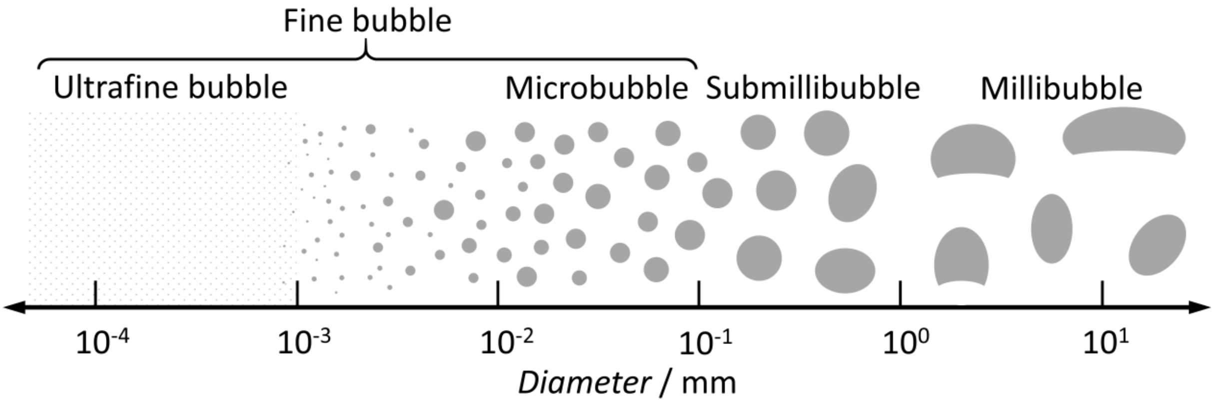

Figure 6: Classification of bubbles depending on volume equivalent bubble diameter.

Microbubbles have a high volume specific surface area resulting in high mass transfer rates, which enables even a quick complete dissolution of microbubbles in the surrounding liquid [59,60]. Already, microbubble gassing is implemented in several commercial processes such as chemical hydrogenation in state of the art ejector loop reactors [61]. In Japanese aquacultures, microbubble aeration is used showing beneficial growth promotion effects [62]. In addition, microbubble gassing is used as a separation method, such as microbubble air flotation to remove oil from aqueous emulsions [63]. Various methods, which utilize different physical effects in gas-liquid flows are used to generate microbubbles [60]. Improved manufacturing methods enabled production of sintered materials with mean pore sizes in the magnitude of 1 µm and below. These materials can be used for microbubble aeration as well. Furthermore, generation of small bubbles is benefited by having a medium with low surface tension and high viscosity as well as providing additional shear forces to act on the sintered frit [64]. Alternatively, a two-phase nozzle producing high shear forces can be used to disperse the gaseous phase resulting in bubbles with diameters of several micrometers. A more energy demanding method is the pressurized dissolution method, where a solution is saturated with a gas at high pressure producing an oversaturated solution compared to ambient conditions. Releasing this solution through a reducing valve into ambient conditions, microbubbles form due to the lowered solubility.

Already, research increasingly focuses on improving the CO_2 utilization and absorption process with microbubble gassing techniques in various CO_2 capture systems such as microalgae cultivation in photobioreactors [65] and amine scrubbing in microreactors [66]. Furthermore, application of microbubbles for the production of calcium carbonate improves the qualities of the obtained precipitated calcium carbonate [67]. Even direct addition of carbonic anhydrase in the amine-based CO_2 capture is shown to improve the mass transfer significantly reducing the overall costs of the process [68]. However, some challenges of the CO_2 capture technology remain including the degradation of primary and secondary amines by oxygen, corrosion by the formation of acids and finding of a suitable storage location for the sequestrated CO_2 [69]. Currently, the most advanced approach uses geological formations for long-term storage [70]. This approach has the risk that CO_2 can leak into the atmosphere through gaps in the geological formation, which is potentially dangerous to life in the surrounding area. Furthermore, the risk of potentially causing an earthquake exists as CO_2 is injected at high pressures deep underground, which can lead to formation of fractures and seismicity in case the pressure is too high [71]. Instead, other processes and current research is focusing on utilizing the sequestrated CO_2 as cheap and readily available resource [35,72]. An overview of potential applications of CO_2 is given in Figure 7.

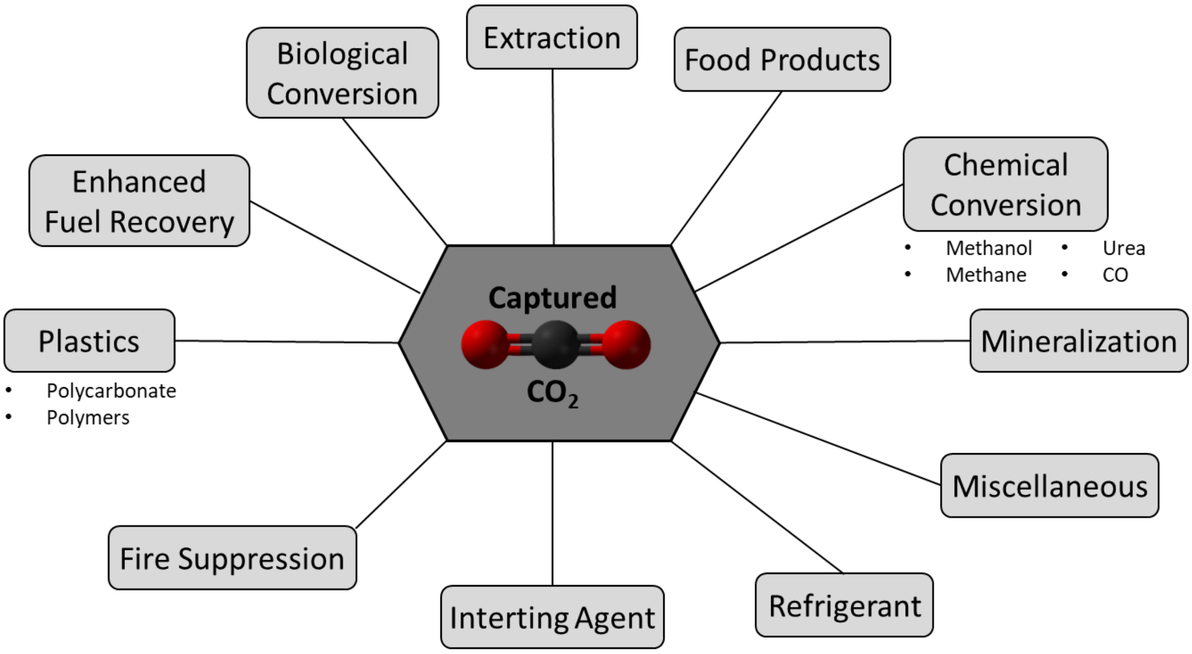

Figure 7: Applications for CO_2 use and reuse. [73]

The application of CO_2 loaded aqueous amine solution for enzymatic carboxylation, reported by Pesci *et al.* (2017), is a promising approach to circumvent the need for a temperature-based regeneration of the amine and for finding a safe long-term storage solution as well as enhancing the carboxylation itself [45]. In this reaction, the CO_2 bound in the liquid phase as hydrogen carbonate is consumed as C1 substrate for the carboxylation of phenolic substrates. The application of amines increases the resulting concentration of CO_2. Therefore, the thermodynamic reaction equilibrium, which is generally limited due to the high thermodynamic stability of CO_2 and HCO_3^-, [44] shifts towards the carboxylation, increasing the yield of the carboxylated product. In this reaction system, a separate CO_2 loading of the aqueous amine solutions has to be performed due to the alkaline nature of amines. Otherwise, the biocatalyst deactivates as most are only stable and active in a narrow pH range, such as the 2,6-DHBD from *Agrobacterium tumefaciens* IAM12048, which is reported to achieve the highest activity at pH 8.5 [74]. In contrast to using carbonate salts as C1 substrate donor, the amine-mediated carboxylation has the huge advantage of using gaseous CO_2 as substrate source. Furthermore, the same benefits of using microbubble gassing can be applied to enhance the mass transfer and CO_2 utilization making the CO_2 saturation process faster and more cost efficient.

1.4. Aim of the Thesis

In this work, the carboxylation of resorcinol to 2,6-DHBA by 2,6-DHBD from *Rhizobium sp.* is combined with the amine-based CO_2 capture technology to enhance product yields using gaseous CO_2 as C1 substrate. Triethanolamine (TEA) being one of the first utilized tertiary amines for industrial amine scrubbing[75] is chosen as model solvent based on the published results in the study by Pesci *et al.* (2017), demonstrating a significant enhancement of the reaction yield[45]. The selected biocatalytic carboxylation reaction system is investigated with the goal to design a biotechnological process. Therefore, different aspects of reaction and process engineering including microbubble gassing are examined to provide new insights into the amine-mediated carboxylation and help to promote the applicability of this system for industry. The objectives of this work are the following:

- The enzyme kinetics and reaction thermodynamic in aqueous TEA are to be elucidated. In this way, the influence of different TEA concentration and CO_2 loadings on the biotransformation are assessed. Furthermore, the characterization provides information to optimize the conversion of resorcinol.
- Enhancing the reaction yield is required to make the biocatalytic carboxylation economically feasible. Following Le Chatelier's principle, CO_2 pressure is used to increase the C1 substrate concentration, shifting the reaction equilibrium towards the product. Therefore, the influence of CO_2 pressure on the carboxylation needs to be studied.
- Further strategies are expected to be necessary to enhance the reaction yield. Therefore, implementation of an *in situ* product removal is assessed as it has the benefit of improving reaction rates and yields. Different materials need to be investigated for *in situ* product removal by precipitation or adsorption to a solid phase.
- Based on the findings, a downstream process to obtain 2,6-DHBA in high purity is to be designed. This gives insights to evaluate the process efficiency and cost. At the same time, the possibility to recycle used solvents and added compounds can be investigated, which reduces material costs.
- As an integral part of the amine-mediated carboxylation, the CO_2 gassing is investigated. Sufficient C1 substrate for the biotransformation can only be provided by supply of gaseous CO_2. Saturation of aqueous amine solutions with CO_2 can be performed by surface gassing or bubble gassing. However, a bigger gas-liquid interfacial area is beneficial to increase the mass transfer. Therefore, different bubble gassing techniques are evaluated with the focus on achieving

smaller bubbles, especially microbubbles, efficiently. The resulting mass transfer and bubble size distribution at different conditions need to be determined. In this way, the gassing efficiency of microbubble and submillibubble gassing can be compared.

Implementation of biocatalysis to produce carboxylated fine chemicals integrates aspects of the principles of green chemistry and has the potential to replace chemical Kolbe-Schmitt processes. This work aims to solve challenges of the biocatalytic carboxylation from a bioprocess engineering perspective. Simultaneously, remaining challenges, which prevent the green alternative to the chemical Kolbe-Schmitt from being economically viable, are highlighted. Furthermore, approaches to solve these challenges are presented beyond a pure bioprocess engineering point of view.

2. Enzymatic Carboxylation of Resorcinol

2.1. Triethanolamine-Mediated Carboxylation

The biocatalytic carboxylation of phenols is known to suffer from unfavorable thermodynamics [76]. Examples are the carboxylation of catechol and resorcinol. For catechol, up to 14% conversion [45] and 32% conversion [35] are reported in a typical biotransformation with 10 mM catechol in 1 M aqueous $KHCO_3$ and 3 M $KHCO_3$ at 30°C, respectively. In comparison, 37% conversion were reported for the carboxylation of 10 mM resorcinol in saturated aqueous $KHCO_3$ [77]. The successful shifting of the reaction equilibrium to higher conversions was demonstrated by Pesci *et al.*, who applied amines such as triethanolamine (TEA) [45]. It was demonstrated that primary, secondary and tertiary amines act as an efficient CO_2 mediator to provide the C1 substrate. This improved the conversion when comparing the aqueous $KHCO_3$ system with amines at a concentration of 1 M. From the work of Pesci *et al.* on using different amines for the enzymatic carboxylation [45], TEA is chosen as a promising mediator.

In general, aqueous triethanolamine solutions are alkaline. Introduction of CO_2 into the medium forms bicarbonate by reacting with TEA and water, which lowers the pH until the equilibrium is reached at CO_2 saturation level. In this way, CO_2 saturated solutions of 1 M and 4 M TEA are measured to reach a pH of 7.5 and 8.3 at CO_2 saturation, respectively. The dissolved CO_2 is subsequently utilized by the 2,6-DHBD from *Rhizobium sp.* for carboxylation of phenols, such as resorcinol and catechol. In both cases, the equilibrium yield is determined at different aqueous TEA concentrations (Figure 8 and Figure 9). For the carboxylation of catechol, the achieved equilibrium yield increases up to 25.6% at 3 M TEA. Even higher yields are achieved for the carboxylation of resorcinol, which is studied in more detail. For this biotransformation, an almost stable equilibrium of around 42% is reached above 2 M TEA.

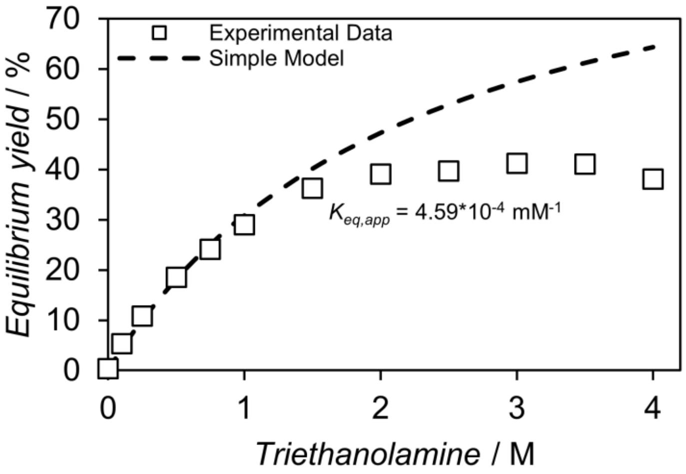

Figure 8: Equilibrium yield at different TEA concentrations with regression of the equilibrium constant using initial TEA concentrations up to 0.75 M in Eq. 7 (Simple Model). The aqueous TEA solutions were saturated with CO_2 before addition of resorcinol and 2,6-DHBD (16.4 U/mg) to final concentrations of 80 mM and 0.38 mg/ml, respectively. The reaction medium was incubated at 30°C for 24 h and 48 h in a closed vessel with no difference between both time intervals.

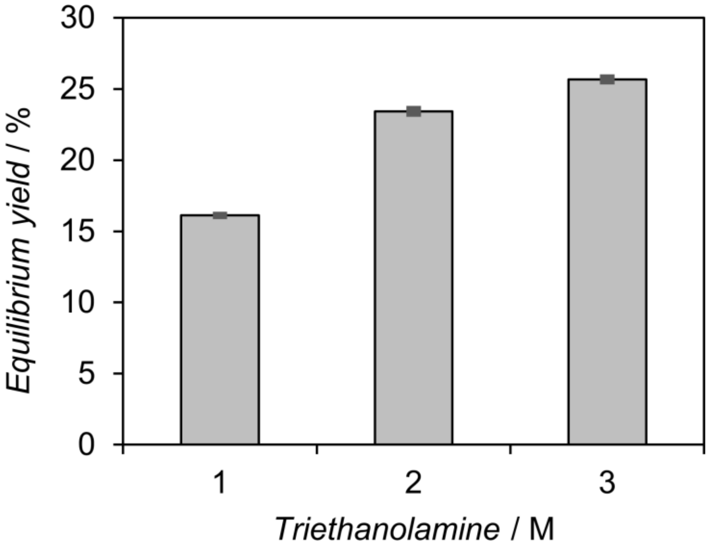

Figure 9: Equilibrium yield for the carboxylation of 80 mM catechol to 2,3-dihydroxybenzoic acid by 10 mg/ml whole cells containing 2,6-dihydroxybenzoic acid decarboxylase in CO_2 saturated triethanolamine at 30 °C. The experiments were performed as duplicated.

The higher yields for resorcinol compared to catechol carboxylation are consistent with studies that utilized aqueous $KHCO_3$ as C1 substrate source. Carboxylation of resorcinol and catechol in 3 M $KHCO_3$ by 2,6-DHBD from *Pandoraea sp.* 12B-2 enabled yields of 48 % and 25 % at 30 °C, respectively [78]. The difference is based on the thermodynamic properties of both aromatic compounds, which determine the productivity and the reaction equilibrium. As shown in Figure 10, the electron-releasing substituent effect of both hydroxyl groups create an electron-rich C2 position. In contrast, the ortho position of the second hydroxyl group creates less electron-rich C3 and C6 positions. This influences the chemical properties, such as redox potential [79] and antioxidant capacity [80] of the dihydroxybenzene isomers. It was shown that the oxidation potential shifts according to the second hydroxyl group position with the meta position (hydroquinone) causing the lowest potential followed by catechol (ortho) and finally resorcinol (para) having the highest positive potential [79].

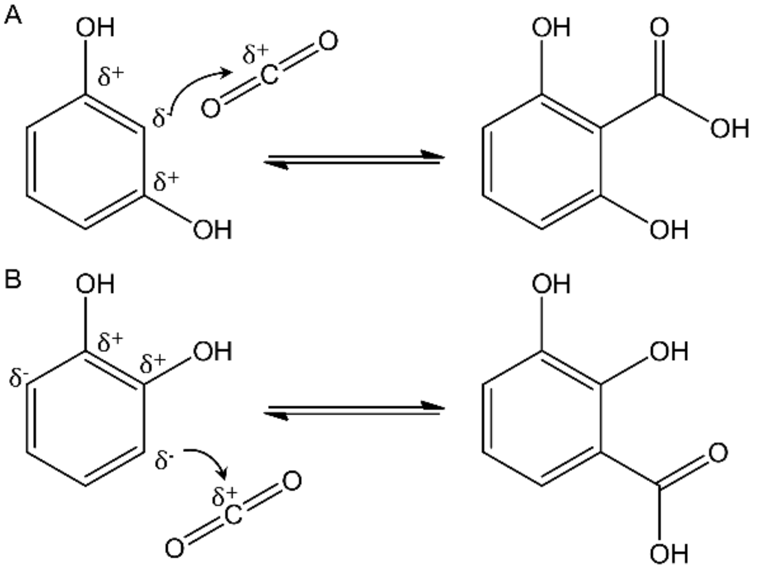

Figure 10: Charge distribution of resorcinol (A) and catechol (B).

The peculiar plateau for the carboxylation of resorcinol in aqueous TEA in Figure 8 was further evaluated by trying to fit the reaction equilibrium constant to the experimental data. Reaching the reaction equilibrium, the forward and backward reaction velocities are equal, resulting in constant equilibrium concentrations of substrates and product. Therefore, the equilibrium position is expressed as equilibrium constant K_{eq}, which relates substrate and product concentration (Eq. 6). Inserting Eq. 6 into the equilibrium yield equation (Eq. 7), the experimental yield can be fitted to the theoretical equilibrium yield. By fitting of the experimential yield of up to 0.75 M TEA (Figure 8) an apparent equilibrium constant of $K_{eq,app} = 4.59 * 10^{-4}$ mM^{-1} is calculated. For this calculation, TEA is assumed to be the second substrate concentration (Simple Model).

$$K_{eq} = \frac{c_{DHBA,eq}}{c_{resorcinol,eq} \cdot c_{C1\ substrate,eq}} \qquad \text{Eq. 6}$$

$$\mathrm{Y_{eq}} = \frac{\mathrm{c_{DHBA,eq}}}{\mathrm{c_{resorcinol,0}}} = \mathrm{K_{eq}} \frac{\mathrm{c_{resorcinol,eq}}}{\mathrm{c_{resorcinol,0}}} \cdot \mathrm{c_{C1\ substrate,eq}} \qquad \text{Eq. 7}$$

The inclusion of all data points in the Simple Model resulted in a poor regression with a R^2 of 0.786. It can be seen in Figure 8 that the difference between the experimental and calculated equilibrium yield increases at higher TEA concentration. This indicates that the assumption of a proportional C1 substrate to TEA concentration applies only for low TEA concentrations. Therefore, it is necessary to incorporate the correct correlation, which enables calculation of the C1 substrate concentration based on the aqueous TEA concentration. Then, the actual C1 substrate concentration can be applied in the model. For TEA, it is known that the solubility of CO_2 in aqueous TEA is strongly dependent on the molar ratio of TEA and water [81]. TEA as an example of tertiary amines forms bicarbonate in a base-catalytic mechanism with CO_2 and a hydroxide ion [48,82]. For the solubility of CO_2 in aqueous TEA, several correlation are reported. [83,84] Jou *et al.* (1985) utilized the method of Kent and Eisenberg (1976) using equilibrium constants to correlate solubility data empirically [84,85]. This approach is used in Figure 11 to calculate theoretical concentrations of CO_2, HCO_3^- and CO_3^{2-} in aqueous TEA at 101.3 kPa and 30 °C. It is clear that the majority of dissolved inorganic carbon (DIC), which is the sum of aqueous species of inorganic compounds, equilibrates to bicarbonate in aqueous TEA. As a result of CO_2 gassing, aqueous CO_2 forms H_2CO_3 in water, which is highly unstable at physiological pH and quickly decomposes into HCO_3^- and H^+. At higher pH, bicarbonate dissociates further to CO_3^{2-} and H^+. As the applied CO_2 solubility correlation is based on an empirical model, DIC calculation gets inaccurate above the correlated concentrations. This limits the applicable solubility model to TEA concentrations of only up to 5 mol/L [84]. This empirical approach is used to correlate the equilibrium yield data to an equilibrium constant (Complex Model I)

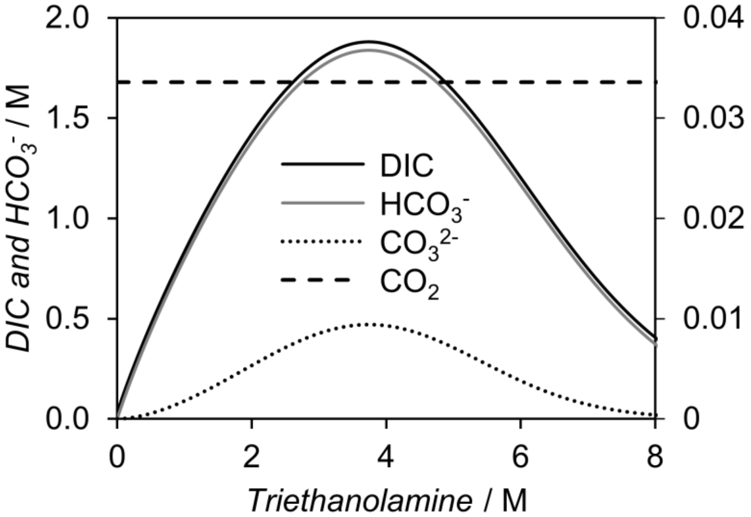

Figure 11: Distribution of dissolved inorganic carbon (DIC) species in aqueous TEA at 100 kPa based on the correlation of Jou *et al.* (1985).

A different approach to calculate the DIC even at very high aqueous TEA concentrations relies on knowing the CO_2 loading capacity Q, which is defined as the ratio of bound molecules of CO_2 per molecule of amine. The CO_2 loading is fitted in Figure 12 to data from literature [81,83,84] at 101.3 kPa with linear expressions (Eq. 8) that takes into consideration the concentration of pure TEA $c_{TEA,max}$ and the maxium CO_2 loading Q_{max} at temperatures between 25 and 125 °C.

$$Q = -\frac{Q_{max}}{c_{TEA,max}} \cdot c_{TEA} + Q_{max} \qquad \text{Eq. 8}$$

Therefore, the boundaries of this model (Complex model II) are defined by the molar ratio of water and TEA. The theoretical maximum CO_2 loading is reached in pure water as there is no amine dissolved. In contrast to pure water, the CO_2 loading approaches zero in pure TEA. This gives an alternative description of the base-catalized adsorption mechanism of tertiary amines, which is dependent on the water content. In consequence of increasing the TEA ratio, less water molecules are present to react with CO_2 to form bicarbonate. In pure TEA, no water is available, which prevents carbonate formation. At 25 °C, fitting Eq. 8 to the data from literature, a Q_{max} of 1.01 mol CO_2 per mol TEA is calculated with a R^2 of 0.977. This value of Q_{max} agrees with the often referred value of 1.0 mol/mol as the CO_2 binding capacity of tertiary amines [48,86]. The highest concentration of DIC can be achieved at 50% (v/v) TEA. Maintaining this ratio was especially important in the first industrial plants that used aqueous triethanolamine until more efficient amines and amine blends were developed [75,86]. After obtaining the value for Q_{max}, the CO_2 loading for a known aqueous TEA concentration can be calculated for the given pressure and temperature. Therefore, the DIC can be calculated according to Eq. 9.

$$DIC = Q \cdot c_{TEA} \qquad \text{Eq. 9}$$

In Figure 12 A and Figure 12 B, the CO_2 loading and DIC in dependence of the TEA concentration is shown after application of the Complex Model II, respectively. Overall, the conversion of CO_2 loading into DIC and *vice versa* is in good agreement with the applied data from multiple publications for the investigated temperature range [81,83,84].

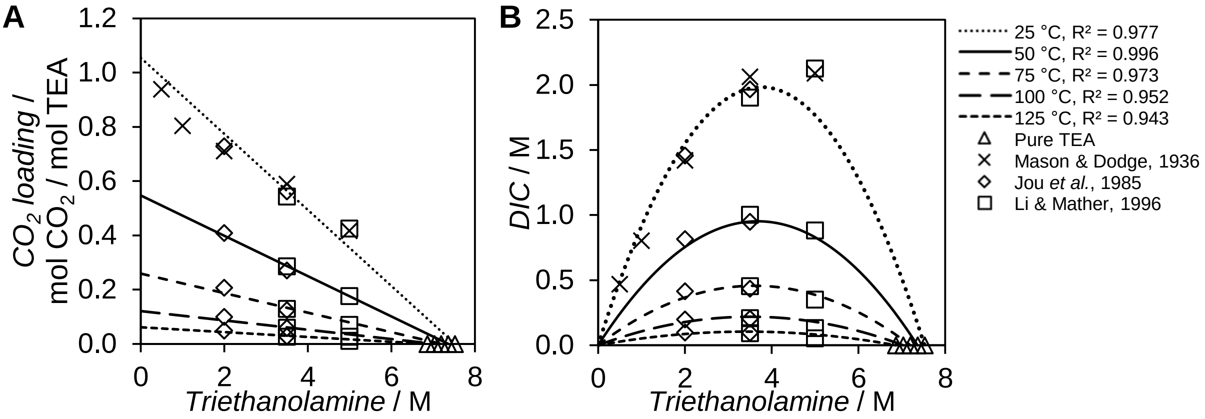

Figure 12: Solubility of CO_2 in aqueous triethanolamine solutions at 100 kPa CO_2 partial pressure shown as CO_2 loading (left) and dissolved inorganic carbon concentration (DIC) (right).

As the biocatalytic carboxylation of resorcinol is performed at 30 °C and 101.3 kPa (ambient pressure), a Q_{max} is derived from the data set. The temperature dependency of Q_{max} can be approximated with an exponential expression (Eq. 10) fitting the data in Figure 13 with a very high R^2 of 0.999. Thus, a Q_{max} of 0.914 mol CO_2 per mol TEA is calculated for 30 °C.

$$Q_{max} = 2.148\, e^{-0.028 \cdot T} \qquad \text{Eq. 10}$$

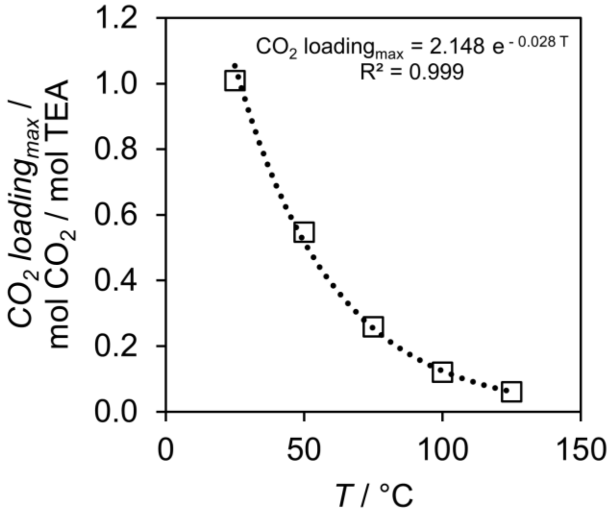

Figure 13: Achievable maximum CO_2 loading of triethanolamine at 101.3 kPa CO_2 partial pressure. Data derived from Figure 12.

Subsequently, both Complex Model I and Complex Model II are applied to the equilibrium yields obtained in the enzymatic carboxylation of resorcinol (see Figure 14). In both cases, an additional dilution factor had to be applied as the reaction mixtures were pre-aerated with CO_2, without substrate and enzyme being present. Addition of substrate and enzyme for start of the reaction therefore diluted the DIC concentration. No additional CO_2 gassing was being performed after substrate and enzyme addition, respectively. Therefore, the effects of the substrate and enzyme solution on the CO_2 solubility due to changing the Henry constant for the new mixture can be neglected. The regression of the experimental equilibrium data with both Complex Models resulted in calculated equilibrium constants of $5.66\cdot10^{-4} \pm 0.10\cdot10^{-4}$ mM^{-1} for the Complex Model I and $6.15\cdot10^{-4} \pm 0.11\cdot10^{-4}$ mM^{-1} for the Complex Model II (Figure 14). In both cases, the second substrate was set to be HCO_3^- as only this DIC species fits the experimental data. By measuring the pH after substrate and enzyme addition, the mole fractions of the dissolved inorganic carbon species in Complex Model II are calculated based on the correlation of Andersen (2002) [87]. Especially, the addition of enzyme solution shifted the pH as the purified enyzme is dissolved in 50 mM potassium phosphate buffer pH 7. Alternatively, the equilibrium yield data could also be fitted to the DIC concentration as the experiments were performed in the pH range, where bicarbonate is the most prominent inorganic carbon species. Therefore, the highest theoretical DIC and consequently a HCO_3^- of 1.85 M can be achieved at 50% (v/v) TEA and 3.75 M TEA at 30 °C based on Complex Model I, respectively. This enables reaching a maximum yield of 50.6% at 80 mM initial resorcinol concentration. In comparison, both Complex Model I and II give similar results for the equilibrium yield. However, it is expected that Complex Model II performs better at high TEA concentrations due to the limited concentration region, which the empirical approach covers.

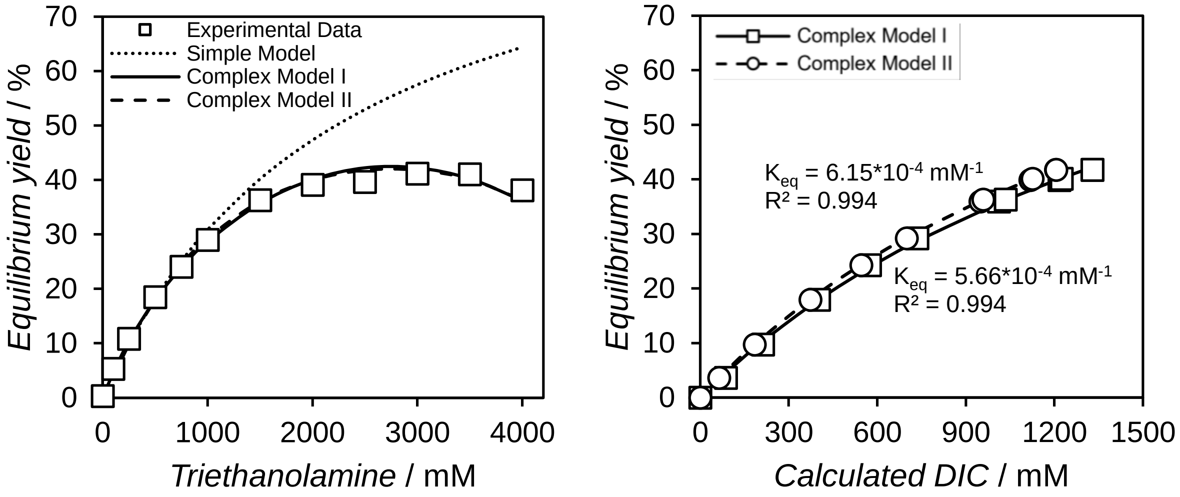

Figure 14: Comparison between experimental and calculated equilibrium yields for aqueous TEA and DIC dependencies. The aqueous TEA solutions were saturated with CO_2 before addition of resorcinol and 2,6-DHBD (16.4 U/mg) to final concentrations of 80 mM and 0.38 mg/ml, respectively. The reaction medium was incubated at 30°C for 24 h and 48 h in a closed vessel with no difference between both time intervals.

Solutions of more efficient amines and amine blends can be utilized to achieve even higher DIC and HCO_3^- concentrations in subsequent works to further improve the maximum reaction yield. Already, propylamine and diethylamine, among other primary and secondary amines, were demonstrated to improve the yield in the enzymatic carboxylation of catechol [45]. In comparison to tertiary amines, which produce carbonates directly without carbamate formation, primary and secondary amines form carbamates first, which produce subsequently bicarbonates in water [47,48]. However, biocatalyst deactivation at higher amine concentration needs to be considered as the deactivation of 2,3-DHBD whole cells in aqueous triethylamine is already reported [88].

2.2. Enzyme Kinetics in Aqueous Triethanolamine

The equilibrium yield experiments for the carboxylation of resorcinol in aqueous TEA indicate that bicarbonate fulfills the requirement to be the active C1 substrate. However, the equilibrium between HCO_3^- and CO_2 is rapidly reached in the reaction mixtures neutral pH region [89]. Therefore, determination of the reacting species, whether it is CO_2 or HCO_3^-, is not unequivocally possible. Nevertheless, in order to gain deeper insights of how the enzyme works in the triethanolamine-mediated reaction system, a kinetic investigation is conducted.

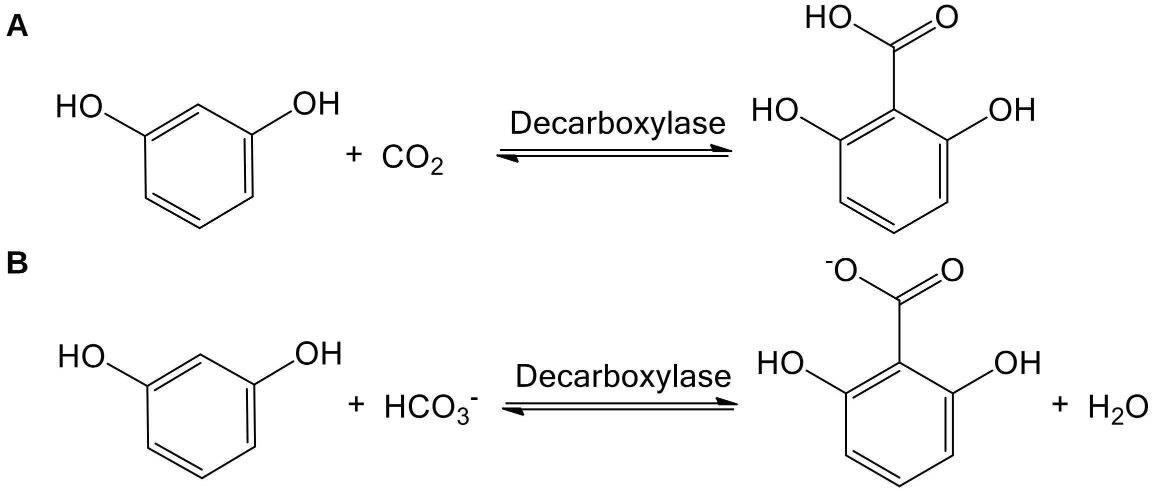

Figure 15: Enzymatic carboxylation of resorcinol utilizing CO_2 (A) or HCO_3^- (B) as C1 substrate.

The enzymatic carboxylation by 2,6-DHBD is a condensation reaction of two substrates (Figure 15), the phenolic and the C1 substrate [36]. In the case of bicarbonate, the condensation is followed by the elimination of water (Figure 15 B). For kinetic determination of the carboxylation, the concentrations of resorcinol and TEA are varied (Figure 19). In the next step, the correct kinetic model needs to be chosen for data analysis. Generally, enzymatic two substrate reactions can proceeds through a Sequential and Ping-Pong mechanism. The Sequential mechanism can be divided into two types, Ordered and Random. The mechanisms are illustrated in Figure 16 to Figure 18, where the substrates are denoted as A and B, whereas the products are denoted as P and Q. These mechanisms model the different possible enzyme reactions, where the order of binding ensures catalytic activity. For example, transaminase catalyzed reaction work in a Ping-Pong mechanism, while 2,6-DHBD is reported to work in a sequential mode [35].

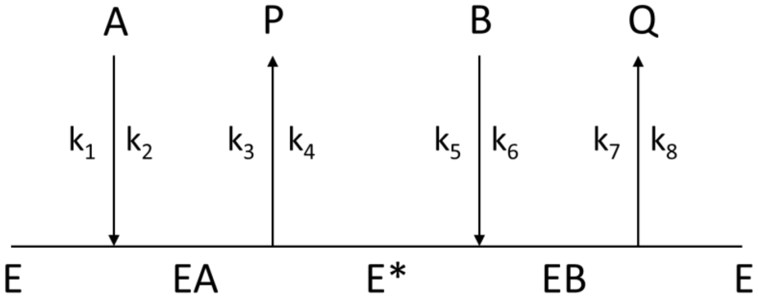

Figure 16: Example of a bi-bi Ping-Pong mechanism.

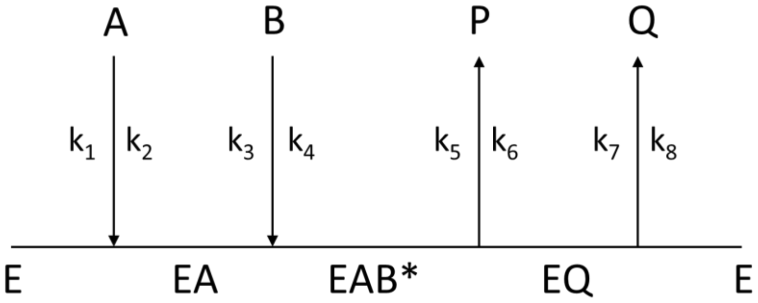

Figure 17: Example of an ordered bi-bi sequential mechanism.

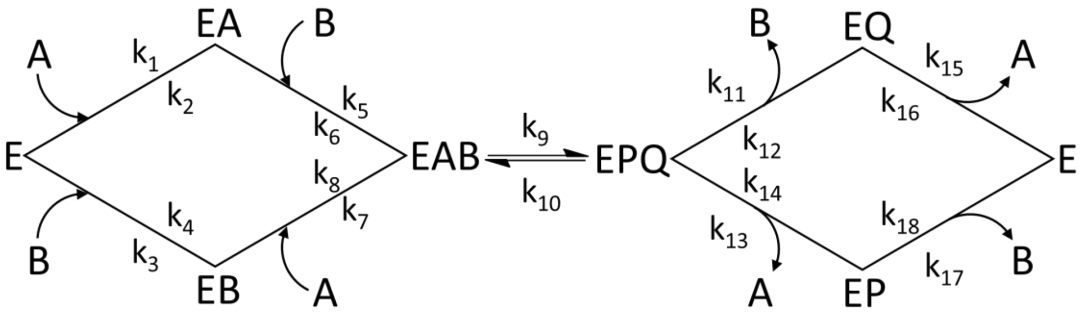

Figure 18: Example of a random bi-bi sequential mechanism.

Based on the mechanism, Michaelis-Menten kinetic equations can be obtained. For the sequential mechanism, the different two-substrate Michaelis-Menten kinetic equations (Eq. 11 - Eq. 13), which differ in the sequence of substrate binding, are listed. In the random sequential model (Eq. 11), it does not matter which substrate binds first. However, for the ordered bi-uni sequential kinetic model, either resorcinol binds first to the enzyme (Eq. 12) or the C1 substrate binds first (Eq. 13). These equations are applied to the experimental data for fitting and calculation of the kinetic parameters as well as testing for the reaction mechanism.

$$v = v_{max}\,\frac{c_{\mathrm{A}} \cdot c_B}{c_A \cdot c_B + K_{M,A} \cdot K_{M,B} + K_{M,A} \cdot\, c_B + K_{M,B} \cdot\, c_A} = v_{max}\,\frac{c_{\mathrm{A}} \cdot c_B}{\left(K_{M,A} + c_A\right) \cdot \left(K_{M,B} + c_B\right)} \qquad \text{Eq. 11}$$

$$v = v_{max}\,\frac{c_{\mathrm{A}} \cdot c_B}{c_A \cdot c_B + K_{M,A} \cdot K_{M,B} + K_{M,B} \cdot\, c_A} \qquad \text{Eq. 12}$$

$$v = v_{max}\,\frac{c_{\mathrm{A}} \cdot c_B}{c_A \cdot c_B + K_{M,A} \cdot K_{M,B} + K_{M,A} \cdot\, c_B} \qquad \text{Eq. 13}$$

The measured initial enzyme activity v is expressed in these equations as a function of the initial substrate concentrations c_A and c_B of both substrates as well as the kinetic parameters. The kinetic parameters include the maximum reaction velocity v_{max} as well as the Michaelis-Menten constants $K_{M,A}$ and $K_{M,B}$ for both substrates, respectively.

These equations are applied to the experimental data for fitting and calculation of the kinetic parameters as well as testing for the reaction mechanism. Successful application of the kinetic models to the experimental data is only possible, if dissolved aqueous CO_2 is selected as C1 substrate, which will be discussed later. In the case of the ordered sequential models, the error in the K_M values is much higher compared to the random sequential model. Additionally, in the ordered sequential fitting with the assumption of CO_2 binding first to the enzyme, an interdependency of both K_M values is occurring. This means that the data can be theoretically be fitted, but every adjustment of one of the K_M values influences the other K_M value without having significant influence on the v_{max} and the quality of the fitting after several fitting iterations. Overall, the random sequential model fits best, which is in agreement to the postulated reaction mechanism of the reversible decarboxylation and successful application of the same kinetic model in the carboxylation of catechol by 2,6-DHBD. [35] The results of the regressions are summarized in Table 2.

Table 2: Kinetic parameters determined for the enzymatic carboxylation of resorcinol by 2,6-DHBD *Rhizobium sp.* in aqueous TEA with application of different two-substrate Michaelis-Menten kinetic models.

	v_{max} (U/mg)	$K_{M,Res}$ (mM)	$K_{M,CO2}$ (mM)	R^2
Random sequential	16.43 ± 3.61	65.7 ± 19.7	109.9 ± 23.8	0.970
Ordered sequential (Resorcinol binds first)	7.77 ± 1.61	531 ± 566	10.28 ± 12.03	0.968
Ordered sequential (CO_2 binds first)	6.67 ± 0.91	f($K_{M,CO2}$)*	f($K_{M,Res}$)*	0.967

*Both K_M values are dependent on each other in the fitting, preventing the calculation of conclusive values. After 400 fitting iterations, the value of $K_{M,'CO2'}$ is >>1000 mM and $K_{M,Res}$ is smaller than 1 mM.

For the variation of TEA, it is essential to calculate the resulting DIC content and distribution of the inorganic carbon species to obtain the correct initial concentrations for application of the kinetic models. Therefore, the TEA dependent changes in the CO_2 loading and the resulting pH of the reaction mixture have to be taken into account. The same approach as in the equilibrium yield experiments is used to calculate the DIC. After CO_2 gassing of the reaction mixture excluding enzyme, the pH was measured. After enzyme addition, the pH changed slightly to values closer to pH 7, which is the pH of the buffer, in which the enzyme was dissolved after purification. The shift in the pH due the buffer prevents the utilization of the previously employed correlation of Jou *et al. (1985)*. Therefore, the measured pH of the reaction mixture is directly used to calculate the distribution of the dissolved inorganic carbon species according to Andersen [87]. This approach cannot differentiate between aqueous CO_2 and H_2CO_3. Therefore, both species are combined and referred to as 'CO_2'. In Figure 19, the initial enzyme activity is shown as function of resorcinol and 'CO_2', which includes the successfully applied random sequential bi-uni kinetic model.

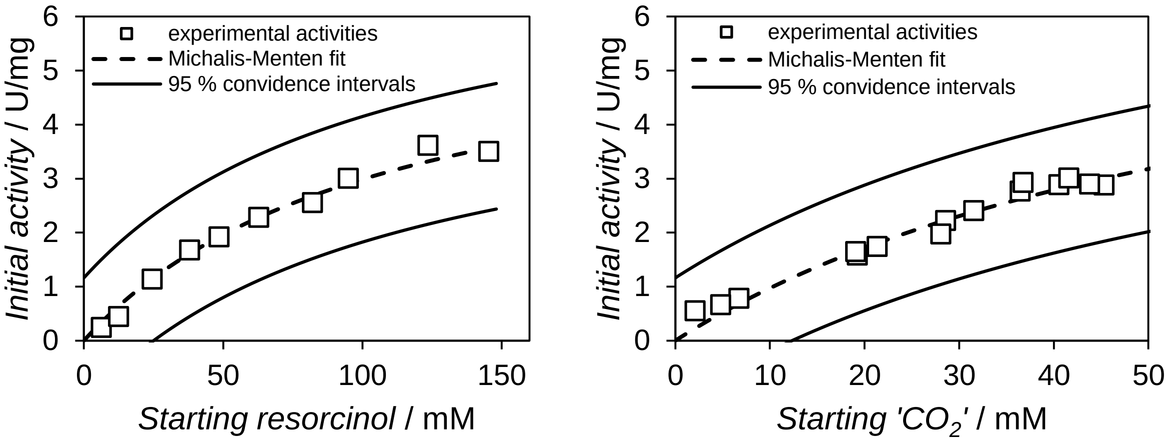

Figure 19: Initial rate measurements for resorcinol in triethanolamine (TEA) at 30 °C. On the left, up to 150 mM resorcinol is used in 1 M aqueous TEA with 92.8 µg/ml 2,6-DHBD. On the right, 90 mM resorcinol is used in 0.1 – 6.3 M aqueous TEA with 92.8 µg/ml 2,6-DHBD. Michaelis-Menten nonlinear regression was performed with the software Origin 2021.

For the determination of the carboxylation kinetics of the phenolic substrate, the resorcinol concentration in 1 M aqueous TEA was varied. At 1 M aqueous TEA, one of the highest 'CO_2' concentrations with up to 43.8 mM was achieved at the given reaction conditions. Lower TEA concentrations resulted in a lower pH, which increased the 'CO_2' ratio of the CO_2 species, but lowered the overall DIC significantly. Higher TEA concentrations enabled higher DIC concentrations, but due to the increase in pH, the ratio of 'CO_2' in the reaction mixture decreased. For the kinetics of the C1 substrate, the concentration of resorcinol was fixed to 90 mM. This prevented excessive enzyme deactivation occurring at higher resorcinol concentrations, which is reported in literature for comparable kinetic studies of similar enzymes in aqueous $KHCO_3$ systems [35,90].

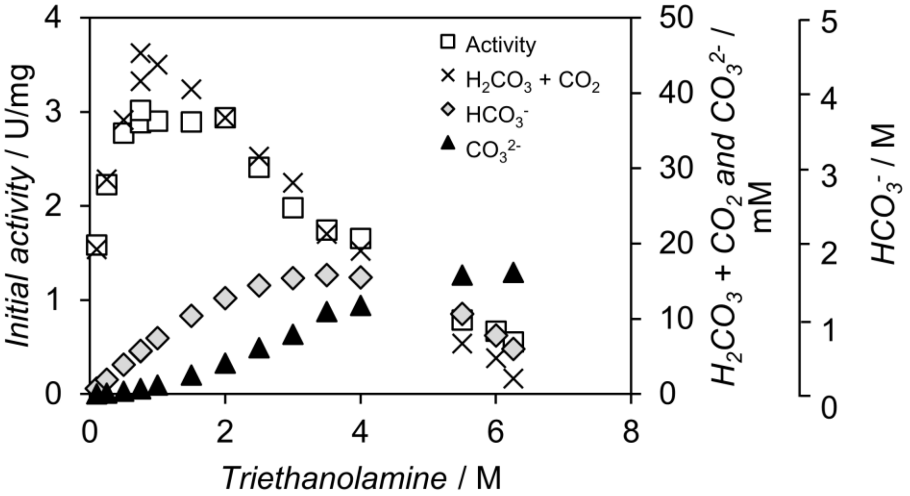

Figure 20: Comparison of measured initial activities and calculated carbon species concentrations for the carboxylation of 90 mM resorcinol in CO_2-saturated TEA at 30 °C by 92.8 µg/ml 2,6-DHBD.

As shown in Figure 20, the ‘CO_2’ concentration is limited in aqueous TEA to values below 50 mM at 30 °C and ambient pressure. The major fraction of DIC is present as bicarbonate in the investigated TEA concentration range. Yet, only the ‘CO_2’ concentration runs in parallel to the initial activity, which is not the case for bicarbonate and carbonate as illustrated in Figure 20. The parabolic shape of the TEA dependent bicarbonate concentration results in a circular activity plot due to the existence of identical bicarbonate concentrations with different initial activities. Similarly, it was not possible to fit the activity data to the CO_3^{2-} concentration. Consequently, application of the two-substrate kinetic model identified CO_2 and alternatively H_2CO_3 as second substrate for 2,6-DHBD catalyzed carboxylation. There are no known inhibitions by DIC species for reversible decarboxylases, which would justify modification of the kinetic model with inhibition terms. Therefore, the results of the kinetic and thermodynamic investigation seem to contradict each other as each model only worked with different C1 substrates, ‘CO_2’ and HCO_3^-, respectively. However, it is worth mentioning that the DIC species were only calculated based on models and not measured directly. In the case of the resorcinol variation for the evaluation of the carboxylation kinetics of the phenolic substrate, small deviations in the pH occurred. These relatively small deviation resulted in pH values of 7.53 to 7.60 after the presaturation of 1 M aqueous TEA. This in turn is influencing the calculated ‘CO_2’ concentrations, which deviated between 37.6 mM and 43.8 mM. Consequently, it can be seen that the slight pH deviation of up to 0.07 units between the measurements already results in major differences of up to 14 % in calculated ‘CO_2’ concentrations. This makes the determination of the kinetic parameters highly error prone. It is possible that these deviations occur due to reaching incomplete CO_2 saturation during presaturation. Additionally, only the concentration of the DIC species is calculated for the bulk reaction medium. This neglects the influence of the enzyme’s microenvironment, which can significantly shift the pH profile for enzymes that consume acids or bases due to diffusion. [91] Therefore, the calculated concentrations of the hydrated CO_2 species need to be treated with caution. The assumption that CO_2 or H_2CO_3 being the indicated second substrate can be supported by CO_2 pressure experiments up to 80 bar from literature [35]. In these experiments, the 2,6-DHBD from *Rhizobium sp.* was utilized reaching up to 7% catechol conversion [35]. Under these conditions, a bicarbonate concentration of only 4 mM is reported. However, at the same time approximately 0.5 M $KHCO_3$ is demonstrated to be necessary to reach such a conversion at ambient pressure. This considerable difference in corresponding bicarbonate concentration supports the finding that a different hydrated CO_2 species must be the C1 substrate. In these cases, the difference is that $KHCO_3$ at ambient pressure and CO_2 at 80 bar were used. Therefore, the resulting pH of the reaction mixture varies leading to different distributions of dissolved inorganic carbon species. Consequently, the concentration of bicarbonate can vary. At the same time, the concentration of CO_2 or alternatively H_2CO_3 can theoretically be comparable, which can explain the particularities in the achieved conversion. To an extent, utilization of molar concentration of $KHCO_3$ results in higher pH and DIC compared to CO_2 pressurized buffers. In aqueous $KHCO_3$ at ambient pressure, the overall DIC content is lower, but the 'CO_2' ratio higher due to the lowered pH. Taken into account the importance of the pH on the distribution of DIC species, it has to be closely monitored. Bicarbonate is the most predominant species in the pH range of 7-10, where 2,6-DHBD shows the highest stability [74]. However, even at pH 5, the enzyme still retained around 80 % of its activity [42]. In this acidic condition, approximately 85 % of the different CO_2 species exist as CO_2 and H_2CO_3. This supports the theory that 2,6-DHBD can utilize 'CO_2' as C1 substrate for the carboxylation.

In summary, the results of the enzyme kinetic investigation underlines that 'CO_2' is acting as the C1 substrate. In contrast, the results from the equilibrium yield investigation (Section 2.1: Triethanolamine-Mediated Carboxylation) revealed bicarbonate to be the C1 substrate. Both results are not necessarily contradicting. For the phenolic acid decarboxylase from *Bacillus subtilis*, density functional theory calculations of the active site revealed a mechanism, in which the CO_2 and indirectly HCO_3^- act as C1 substrate [92]. In this study, the obtained energy profile for the carboxylation reaction suggests that the source of the carboxylate group is CO_2. However, this CO_2 is formed by decomposition of H_2CO_3, which is generated by protonation of bicarbonate by a glutamic acid residue found in the active site [92]. Therefore, the enzyme additionally functions similar to a carbonic anhydrase utilizing CO_2 and HCO_3^- in conjunction. A similar mechanism could be possible for *Rhizobium sp.* 2,6-DHBD based on the amino acid residue structure of the catalytic center [93], even though both enzymes have a low sequence identity [94]. The most likely candidate would be Asp287 (PDB: 2DVU) being in close proximity to the C1 atom of the carboxylate as shown in Figure 21. Already, this residue is proposed to protonate the C1 atom of the carboxylate in the decarboxylation direction [95]. Following the transition state of the protonation, the C-C bond between the carboxylate group and the C1 atom breaks to form the phenol and CO_2 [95]. Although this study focused on the decarboxylation direction, it is fair to assume that this is also true for the reverse direction, since the reaction proceeds *via* the same transition states. For a 5-carboxyvanillate decarboxylase, which is mechanistically closely related to 2,6-

DHBD [96], it was even proven that the decarboxylation proceeds to generate CO_2 rather than bicarbonate as initial product [97].

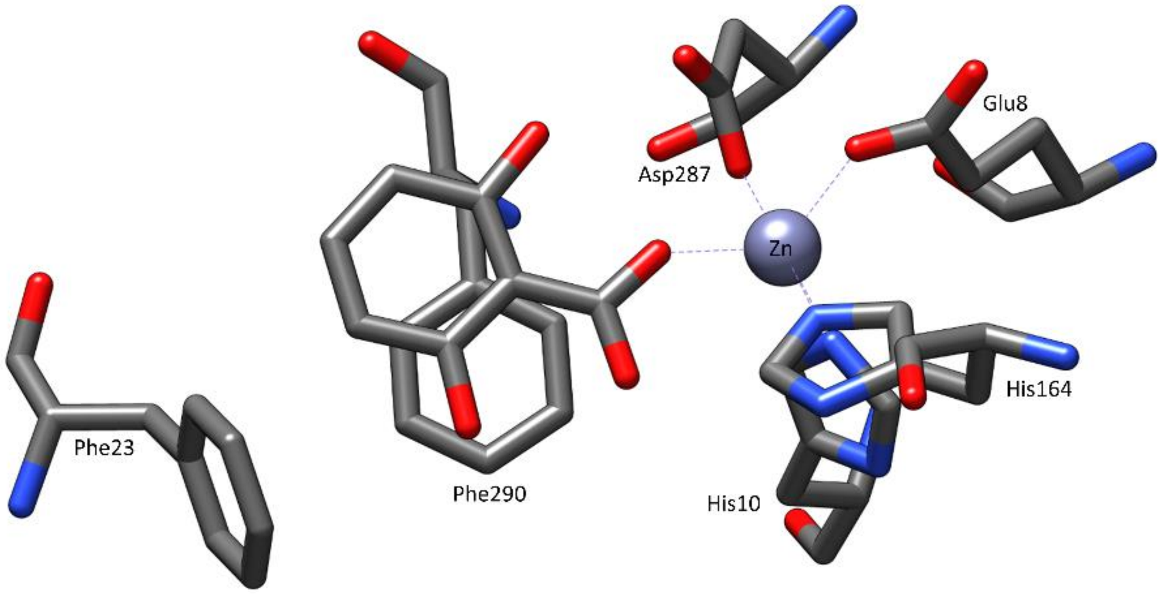

Figure 21: Crystal structure of the catalytic center of *Rhizobium* sp. 2,6-dihydroxybenzoic acid decarboxylase (PDB: 2DVU).

The likely protonation of bicarbonate by Asp287 would enable the pre-equilibrium of CO_2 prior to the carboxylation step with the reversible decarboxylase additionally functioning similar to a carbonic anhydrase. In conjunction with the non-enzymatic equilibrium between bicarbonate and carbonic acid, the feasibility to perform carboxylation reactions using bicarbonate salts as source of the C1 substrate was demonstrated in several studies [33,44,88]. Nevertheless, dealing with excess bicarbonate after the reaction and overall low conversions remain major challenges in these systems. Consequently, research also focusses on product recovery without elimination of excess bicarbonate [98,99] and the development of strategies to improve the overall conversion [45].

2.3. Pressure-Enhanced Carboxylation

Strategies to increase the product yield in the thermodynamic limited carboxylation of phenols are essential to make this system commercially viable. One strategy to enhance the product yield is the addition of an excess of the C1 substrate. In the conventional approach, the C1 substrate is supplied by addition of bicarbonate salts, which is limited by the solubility of the particular salt. In contrast, the amine-mediated system utilizes gaseous CO_2 to provide the C1 substrate. This enables the application of CO_2 pressure to increase the dissolved inorganic carbon and by this, the C1 substrate. For calculation of the CO_2 solubility in aqueous TEA, the correlation of Jou *et al.* (1985) is once more utilized. Additionally, the pH of the reaction solution can be calculated as this correlation incorporates the method of Kent and Eisenberg (1976) to use equilibrium constants to correlate solubility data. This approach is used to calculate theoretical concentrations of CO_2/H_2CO_3, HCO_3^- and CO_3^{2-} in aqueous TEA up to 1200 kPa. In combination with the previously obtained equilibrium constant from the Complex Model I, theoretical equilibrium yields and experimental reaction yields are compared in Figure 22.

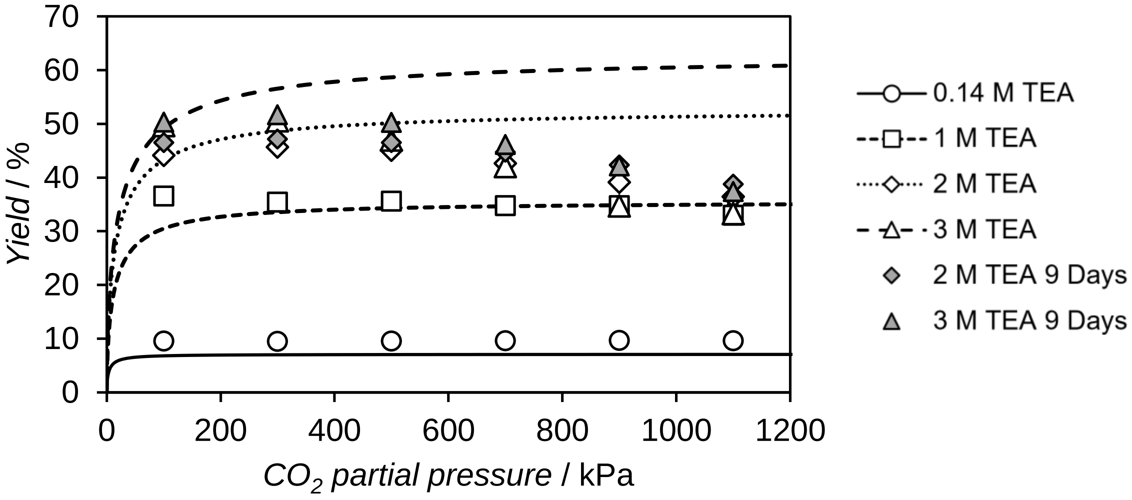

Figure 22: Theoretical equilibrium yield (lines) and experimentally determined reaction yield (symbols) up to 1200 kPa CO_2 in 0.14 M to 3 M aqueous triethanolamine. Samples were incubated for 2 days and 9 days. Only the 9 day samples of 2 and 3 M aqueous TEA are shown as the yield still increases.

It can be seen that the yield prediction fits to the experimental data for up to 1 M aqueous TEA. At high TEA concentration, the experimentally obtained yields are below the predicted equilibrium yield with the deviation increasing at higher applied CO_2 partial pressures. Additional tests confirm that the equilibrium was not yet reached for these data points as an extension of the reaction time led to a further increase in reaction yield. Furthermore, a control experiment, where the decarboxylation of 80 mM 2,6-DHBA was tested up to 1200 kPa was performed. There, the same effect of not reaching the equilibrium after 10 days of incubation is observed. This excludes resorcinol dependent deactivation of the enzyme. Moreover, a pH dependent enzyme deactivation is unlikely as the slightly alkaline pH lowers at higher CO_2 partial pressures. Therefore, the pH region is reached where the enzyme is reported to be most active [74]. The calculated pH profile can be seen in Figure 23 for the investigated TEA concentrations up to 1200 kPa. Initially, the pH of CO_2 loaded aqueous TEA solutions decreases rapidly until being buffered by the TEA and the bicarbonate equilibrium.

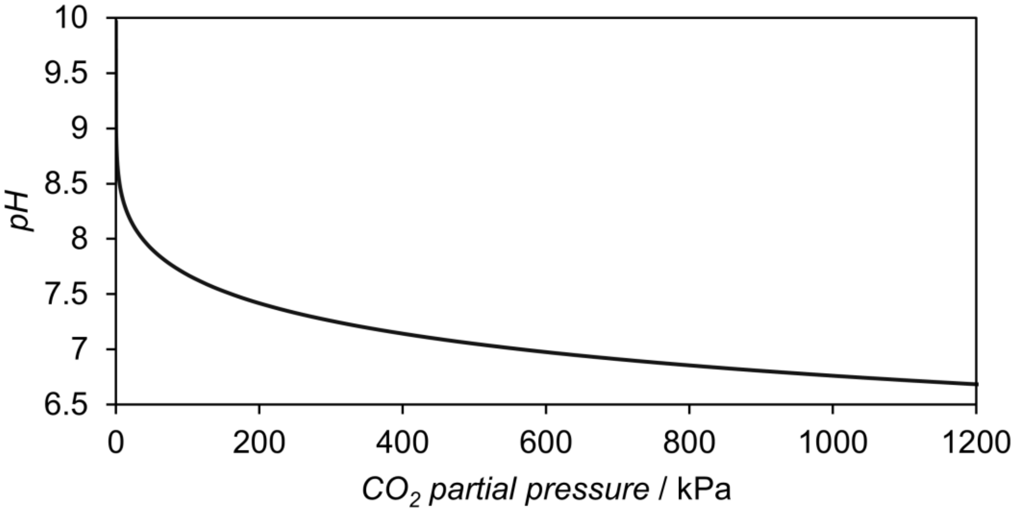

Figure 23: Profile of pH at CO_2 partial pressures up to 1200 kPa at 25 °C in aqueous triethanolamine calculated according to Jou *et al.* (1985).

In consequence of the lowered pH, the mole fraction and concentration of 'CO_2' increases, which is expected to increase the enzyme activity as well, based on the results from the previous kinetic investigation. An exemplary concentration profile of the different DIC species is shown in Figure 24 for 1 M aqueous TEA demonstrating that both CO_2 and HCO_3^- concentration increase. Therefore, the increase in C1 substrate concentration, whether CO_2 or HCO_3^-, cannot readily explain the reduced enzyme activity without an existing and overlooked inhibition. Regarding possible inhibitions, Ribulose-1,5-bisphosphate carboxylase/oxygenase and haemoglobin are prominent examples, which are CO_2 regulated. In haemoglobin, the carbamate formation on the N-terminal valine [100,101] modulates the affinity for oxygen binding at physiological conditions [102]. In the case of Ribulose-1,5-bisphosphate carboxylase/oxygenase, which fixes atmospheric CO_2 in plants, Mg^{2+} and inorganic carbon act as cofactors [103]. For enzyme activation, carbamylation occurs due to binding of CO_2 as cofactor to an alternative site on the enzyme as demonstrated in several studies [104–106]. In general, carbamate formation is reversible, when occurring between CO_2 and neutral amines. Nevertheless, a recent study on CO_2 mediated posttranslational modification of proteins gives insights that carbamylation of proteins is relevant at physiological conditions and impacts protein biochemistry [107]. According to these new findings, it is likely to that carbamylation causes the observed discrepancy between experimental and theoretical yields by reducing the 2,6-DHBD activity. In particular, the discrepancy is only observed when high DIC concentrations are applied by increasing aqueous TEA concentrations and CO_2 partial pressures as shown in

Figure 22. In future works, this hypothesis can be further investigated by application of carbamate-trapping methods and subsequent analysis of the derivatized enzyme. Such methods include ethylation of carbamates by application of triethyloxonium and investigation of derivatives with NMR spectroscopy and LC-MS methods [107].

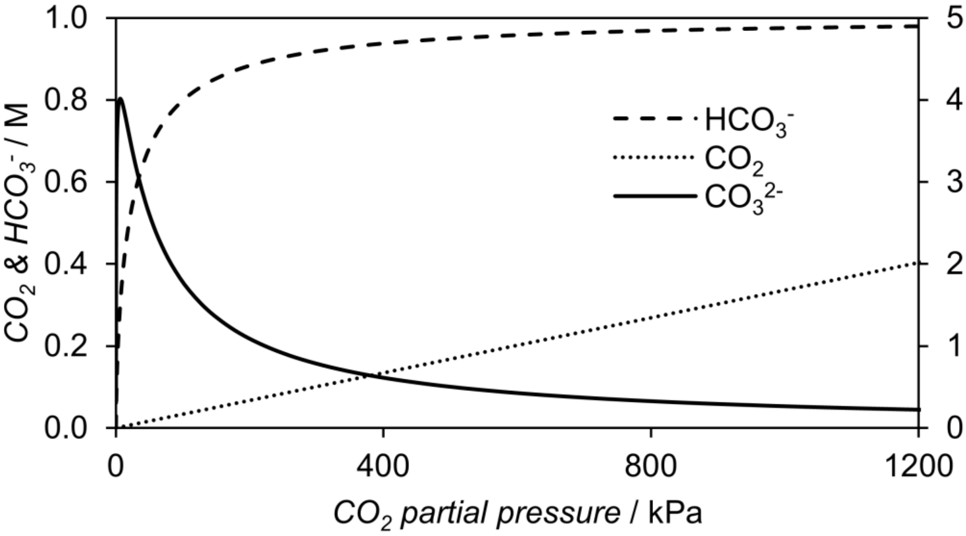

Figure 24: Dissolved concentration of CO_2/H_2CO_3, HCO_3^- and CO_3^{2-} in 1 M aqueous triethanolamine up to 1200 kPa at 25 °C.

In summary, it is shown that experimental yields obtained for the carboxylation of resorcinol at elevated pressure match the theoretical yields calculated on basis of the previously obtained equilibrium constant and the CO_2 solubility correlation established by Jou and colleagues. For the investigated reaction system, increasing the CO_2 partial pressure above 100 kPa only leads to limited yield improvements. Furthermore, a reduction in enzyme activity is observed at high DIC concentrations, which makes the application of CO_2 pressure above 100 kPa counterproductive. It is proposed that carbamylation of neutral amines in the 2,6-DHBD protein structure inhibits the enzyme activity.

2.4. Shifting the Equilibrium Yield with *in situ* Product Crystallization

In general, biocatalytic reactions are enhanced by application of *in situ* product removal (ISPR) techniques. This enables the reduction of occurring product inhibitions due to reducing contact between biocatalyst and product. Additionally, this improves the overall reaction speed as the availability of the product for the reverse reaction is minimized. As a consequence, reaction yields are enhanced, which otherwise would be limited through unfavorable thermodynamic equilibria. In the case of the biocatalytic carboxylation of resorcinol, achieving higher reaction yields is crucial for competing against the established chemical process, the Kolbe-Schmitt reaction. For the biocatalytic carboxylation of resorcinol and catechol, an ISPR method was first described by Ren *et al.*, who used quaternary ammonium compounds to selectively crystallize the carboxylic acid products *in situ* [77]. They demonstrated that the application of the appropriate quaternary ammonium compound enabled reaching conversions up to 99 %, when using aqueous $KHCO_3$ as C1 substrate donor. Based on these results, tetrabutylammonium bromide (TBA-Br) is applied for investigation of *in situ* crystallization of 2,6-DHBA produced in the aqueous TEA system as illustrated in Figure 25. In this combinational approach, aqueous TEA provides the C1 substrate for the biotransformation by CO_2 mediation and TBA-Br acts potentially as product precipitant.

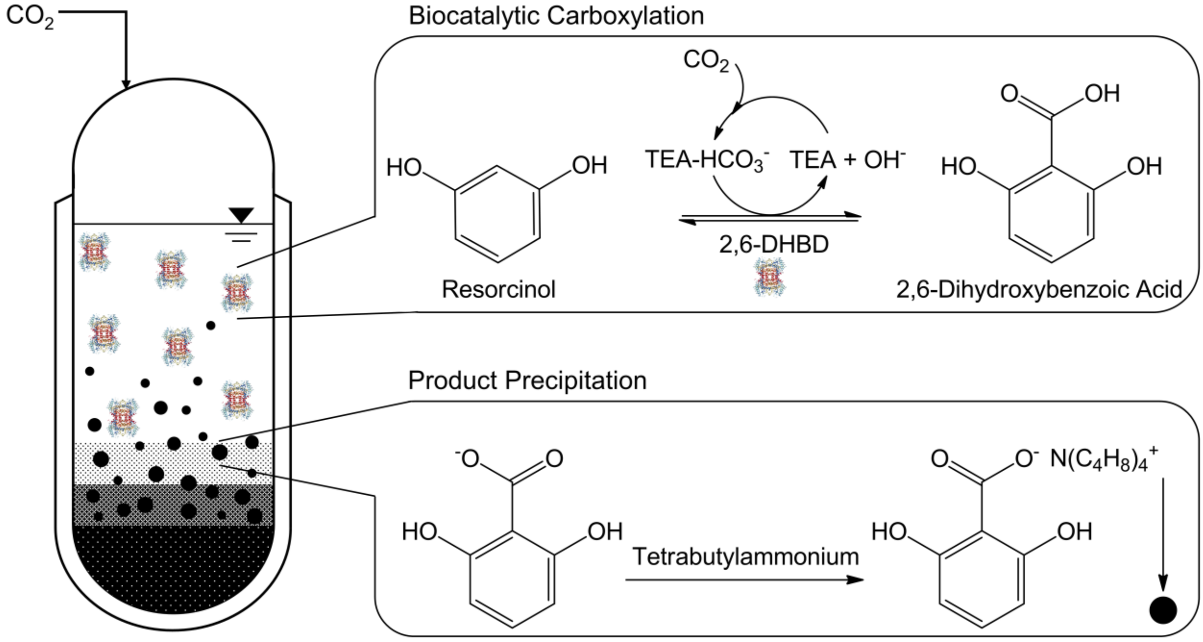

Figure 25: Overview of the proposed effect of tetrabutylammonium bromide to precipitate 2,6-dihydroxybenzoic acid produced by carboxylation of resorcinol by 2,6-DHBD in the aqueous triethanolamine reaction system.

Similar to using TBA-Br in the aqueous $KHCO_3$ system, the application of TBA-Br is enhancing the yields significantly compared to just using aqueous TEA without quaternary ammonium compound as shown in Figure 26. The theoretical equilibrium yield without TBA-Br is based on the previously determined K_{eq} of $5.66 \cdot 10^{-4}$ mM^{-1} (Complex Model I), which enables calculation of TEA dependent equilibrium yields. For the lowest investigated TEA concentration of 0.14 M, the highest enhancement is achieved in the carboxylation of 80 mM resorcinol. Here, the yield increases by a factor (Enhancement) of 6.7 from 6.5 % to 43.3 % with addition of 350 mM TBA-Br. Increasing the TEA concentration, even higher reaction yields are achieved. However, the equilibrium yield decreases after increasing the TEA concentration above a critical concentration. This is consistent with a reduction in the factor of enhancement from 6.7 at 0.14 M TEA to 1.0 at 3.75 M TEA (Figure 26 B). Therefore, the reaction yield is independent of TBA-Br addition reaching 3.75 M TEA, which also matches with the observation that no precipitate formation occurred.

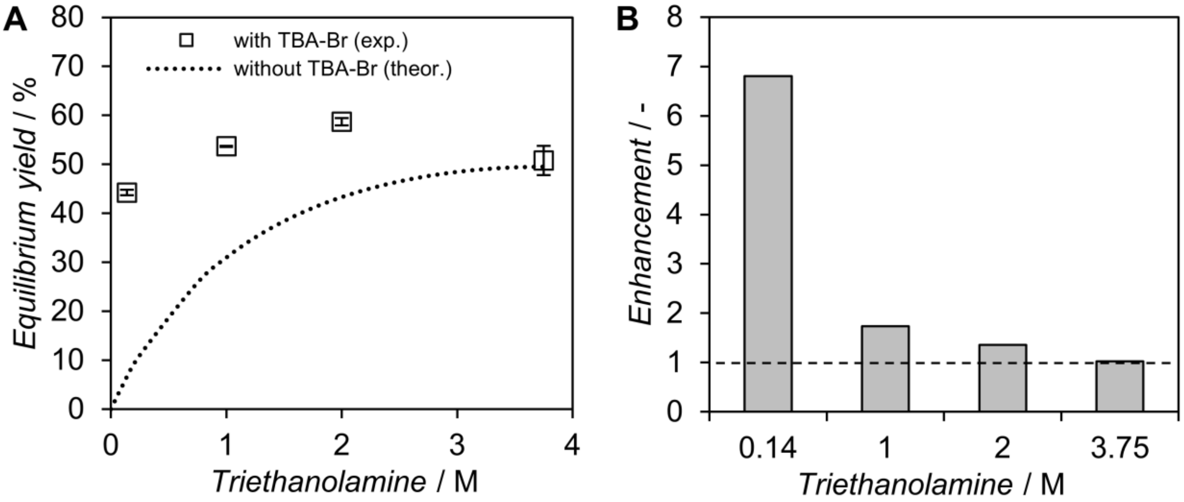

Figure 26: Equilibrium yield for the carboxylation of 80 mM resorcinol in CO_2-saturated aqueous triethanolamine by 0.38 mg/ml 2,6-DHBD (16.4 U/mg) at 30 °C after 24 h with and without 350 mM tetrabutylammonium bromide. Experiments were performed as duplicates.

Even though the product crystallization is not as prominent as in the aqueous $KHCO_3$ system, optimization of concentration and molar ratios between TEA, resorcinol and TBA-Br could improve the reaction yield further. Additionally, utilization of different amines [45] and amine blends [46] for CO_2 mediation can be investigated with the potential to overcome the observed limitation on quaternary ammonium dependent crystallization. At the same time, the application of more efficient amines and amine blends in respect to CO_2 loading capacity is beneficial to reach higher DIC concentrations. However, potential carbamylation-dependent enzyme deactivation has to be considered.

Already, the TEA-mediated system has the major advantage of being reusable with CO_2 compared to the $KHCO_3$ system. In combination with the *in situ* precipitation, a first and easy downstream processing is conceptualized (Figure 27). Here, the biotransformation occurs as shown in Figure 25. Additionally, the solid phase, which consists of the precipitate, is separated from the liquid phase, the reaction medium, by centrifugation. Alternatively, a filtration process would be possible, too. The subsequent addition of HCl dissolves leftover substrate and ammonium compounds. Through a second solid-liquid separation, pure product powder is obtained, which needs additional drying. In this process, the liquid side stream from the separation process can be recycled. Aqueous TEA from the first separation can directly be recycled and once more loaded with CO_2. A method to recover the quaternary ammonium compound was previously described by Ren *et al.*, who used a chloroform extraction procedure in the aqueous $KHCO_3$ system [77]. Overall, improvement of the *in situ* precipitation to reach full conversion would enable a much easier downstream processing with less handling of unreacted substrate.

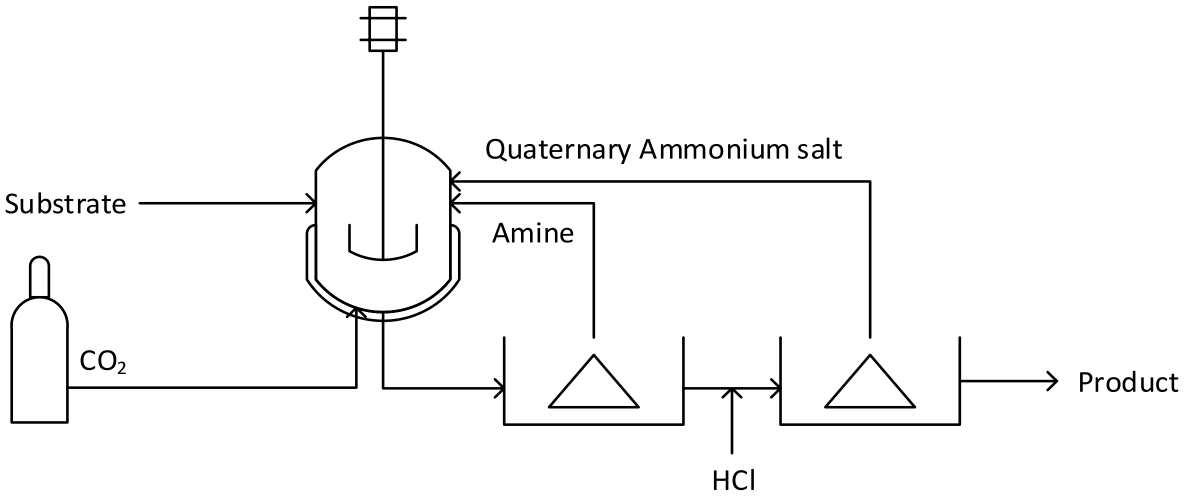

Figure 27: First concept of a simplified process for the biocatalytic carboxylation of resorcinol in aqueous triethanolamine, which includes an integrated downstream process based on the in situ product crystallization of 2,6-dihydroxybenzoic acid when using a quaternary ammonium salt like tetrabutylammonium bromide.

In conclusion, development of an ISPR process based on using dissolved quaternary ammonium salts is possible. Nevertheless, several challenges remain and need to be addressed to create an economically viable bioprocess. These challenges include among other that (1) the reaction yield is still limited, when using TBA-Br in the aqueous TEA system and (2) that the two-phase product precipitate cannot be pumped conveniently and has to be transported by alternative systems. Here, solid particles with quaternary ammonium functionalized groups can provide a favorable substitution. This gives the opportunity to create a liquid exclusive chromatography-based ISPR process. The approach to substitute dissolved quaternary ammonium salts with anion exchange resins containing quaternary ammonium functionalized groups in the aqueous TEA system is investigated in the next section (2.5).

2.5. Application of an Anion Exchange Resin for *in situ* Product Removal

ISPR approaches for carboxylic acids utilize processes such as liquid-liquid extraction [108] and chromatography-based [109] methods. For the biocatalytic carboxylation of catechol and resorcinol, liquid-liquid extraction could not yet be successfully implemented, because of the similarity of substrate and product and therefore a lack of selectivity [88]. In regard to chromatography-based separation approaches, anion exchanger are already reported to remove efficiently the product of the biocatalytic carboxylation of orcinol in a $KHCO_3$ system [98]. Separation of catechol and 2,3-DHBA was already studied with several different anion exchanger, which all showed competitive adsorption of catechol [88]. This included the weak anion exchanger Amberlite IRA67® and Dianion WA30® as well as strong anion exchanger Amberlite A26® and Amberlite IRA958® [88]. Both weak anion exchanger have tertiary amines as functional groups, but different backbone matrices. Amberlite IRA67® has a hydrophilic acrylic structure, whereas Dianion WA30® consists of a styrene-divinylbenzene backbone. In contrast to these resins, both strong anion exchanger have functional groups of quaternary ammonium. Similarly, the Amberlite IRA958® has an acrylic structure and the Amberlite A26® has a styrene-divinylbenzene backbone. Finding an appropriate adsorber, product selective resins can provide a favorable substitution to the previously investigated ISPR of utilizing dissolved quaternary ammonium salts.

The range of investigated anion exchanger for resorcinol and 2,6-DHBA separation is expanded with the strong anion exchanger Dowex® 1X8-50, which has trimethyl ammonium functionalized groups on 50 µm sized carriers. This carrier is similar to Amberlite A26®, but has slightly different properties, such as a smaller particle size and different cross-linking percentage. Already, Dowex® resins were investigated for the downstream process of 2,6-dihydroxy-4-methylbenzoic acid with a good selectivity [110]. Therefore, this resin is chosen for tests in the investigated aqueous TEA system. Respective results confirm that Dowex® also has a higher affinity to the product 2,6-DHBA compared to the phenolic substrate resorcinol. In an 80 mM equimolar mixture of resorcinol and 2,6-DHBA in 1 M aqueous TEA saturated with CO_2, 38.1 mM (95 %) product and 23.9 mM (60 %) substrate is measured to bind on 50 mg/ml Dowex®. Consequently, this can be regarded as a milestone as it is now the first reported adsorber that has a higher selectivity towards 2,6-DHBA compared to resorcinol to the best of our knowledge. This makes it possible to shift the reaction equilibrium by applying Dowex®. A comparative investigation of the binding capacity and selectivity is performed to assess the feasibility of an adsorption-based ISPR. The binding capacity and selectivity are investigated by the variation of the mole fraction of 2,6-DHBA and resorcinol as well as the variation of the adsorbent concentration (Figure 28). Different competitive isotherms for binary mixtures and the single solute Langmuir isotherm are applied. The extended Fritz and Schlünder isotherm is the most flexible of the tested isotherms due to the high number of fitting parameters. Therefore, the experimental data in Figure 28 is fitted accurately with a very high R^2 of 0.989. A summary of the fitting parameters of the different isotherms are listed in Table 3. In general, all tested isotherms have high R^2 and are suitable to predict the distribution of resorcinol and 2,6-DHBA.

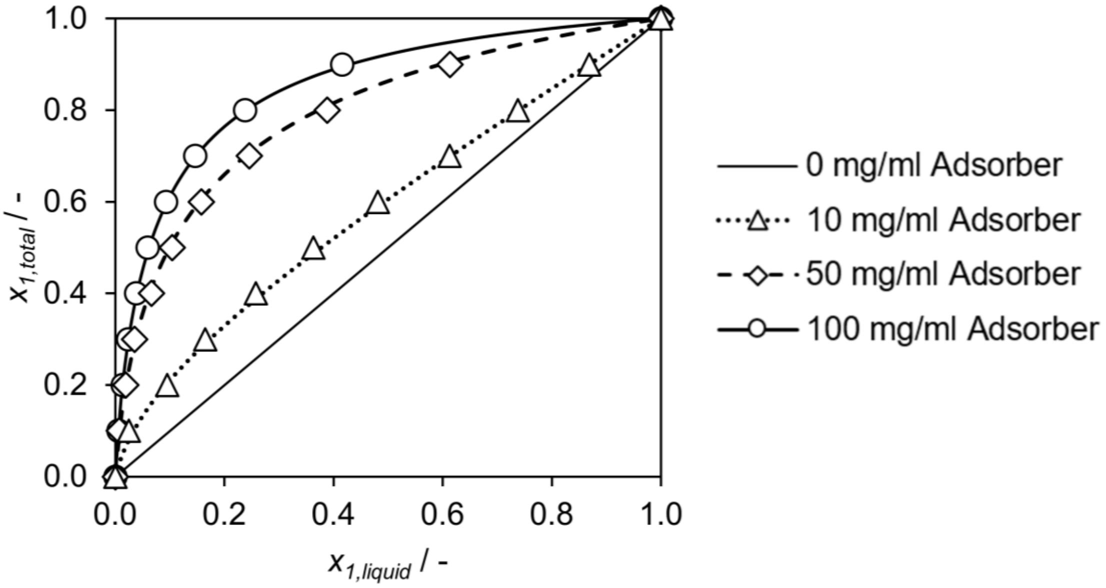

Figure 28: Adsorption isotherm of an 80 mM mixture of 2,6-DHBA and resorcinol on the adsorber, Dowex® 1x8-50 at different concentrations in 1 M aqueous TEA saturated with CO_2 at 30 °C.

From Figure 28, it can be seen that for a fixed mole fraction in the liquid phase $x_{1,liquid}$, the mole fraction of 2,6-DHBA in the multiphase system $x_{1,total}$ increases when more adsorber is added to the suspension. This effect enables the enhancement of the overall reaction yield when combining the adsorption process in a batch mode with the enzymatic carboxylation. In this process, the reaction product 2,6-DHBA adsorbs more selectively to the solid phase and is no longer available for the enzymatic carboxylation, which only occurs in the liquid phase. Therefore, the liquid mole fraction $x_{1,liquid}$ equals the reaction yield in the biotransformation in the case of no adsorber addition. Accordingly, $x_{1,total}$ equals the improved reaction yield when adding adsorber to the biotransformation.

Table 3: Isotherm parameters of 2,6-DHBA (1) and resorcinol (2) adsorbed on Dowex® 1x8-50 at 100 kPa and 30 °C.

			Extended Langmuir isotherms					
Jain and Snoeyink (1973)			Butler and Ockrent (1930)			Single Solute		
$q_{m,1}$	mol g^{-1}	1.857	$q_{m,1}$	mol g^{-1}	1.838	$q_{m,1}$	mol g^{-1}	1.807
$q_{m,2}$	mol g^{-1}	1.806	$q_{m,2}$	mol g^{-1}	2.028	$q_{m,2}$	mol g^{-1}	1.946
b_1	mM^{-1}	0.597	b_1	mM^{-1}	0.589	b_1	mM^{-1}	0.560
b_2	mM^{-1}	0.038	b_2	mM^{-1}	0.032	b_2	mM^{-1}	0.026
R^2		0.989	R^2		0.989	R^2		0.959
			Extended Freundlich isotherms					
Sheindorf *et al.* (1981)			DiGiano *et al.* (1978)			Fritz and Schlünder (1974)		
K_1		0.709	K_1		0.742	$b_{1,1}$		1.633
K_2		0.139	K_2		0.280	$b_{1,2}$		0.257
n_1		0.332	n^{-1}		2.959	$b_{2,1}$		1.180
n_2		0.577	R^2		0.978	$b_{2,2}$		0.214
$K_{1,2}$		0.044				$b_{2,2,1}$		1.880
R^2		0.988				$b_{2,1,2}$		0.037
						n_1		0.911
Extended Tóth isotherm						n_2		0.996
Jaroniec and Tóth (1976)						m_1		0.771
q_m	mol g^{-1}	1.910				m_2		0.872
b_1	mM^{-1}	1.685				$m_{1,2}$		0.991
b_2	mM^{-1}	27.02				$m_{2,1}$		0.728
n		0.985				d_1		1.217
$b_{1,2}$		0.062				d_2		3.518
$b_{2,1}$		16.03				R^2		0.989
R^2		0.989						

Application of the isotherms, such as the extended Fritz and Schlünder isotherm, enables the prediction of the reaction yield in relation to the addition of Dowex® into the system (Figure 29). Increasing the Dowex® concentration results in the shifting of the reaction yield nearly linearly for Dowex® concentrations up to 30 mg/ml. However, the reaction yield enhancement is only minimal at high Dowex® concentrations. Additionally, utilization of high Dowex® concentrations becomes unfeasible in context of reaction kinetics due to resorcinol binding and impairing of the mixing of the suspension. In general, viscosity increases with particle volume fraction, and it gets susceptible to shear stress as shown for aqueous dispersions of 250 nm poly(styrene-ethylacrylate) particles [111]. In conjunction, the dispersed particles disturb the mixing, leading to extra energy dissipation [112]. Additionally, the high frequency of contact at high particle volume fraction can damage the particles causing a decrease in particle size distribution during mixing.

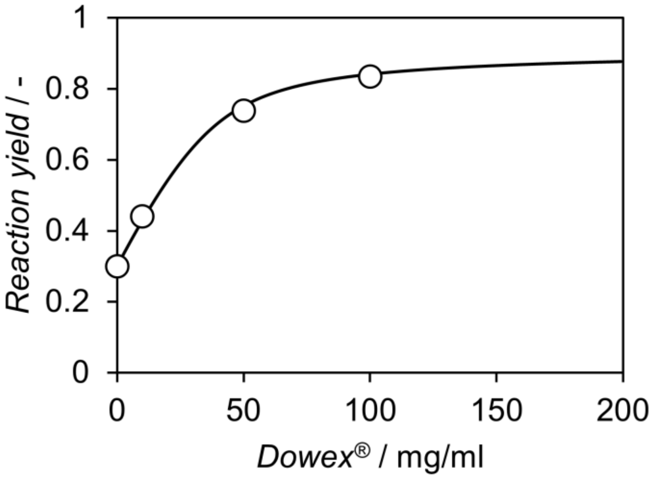

Figure 29: Enhancement of the reaction yield by utilization of Dowex® 1x8-50 in 1 M aqueous TEA saturated with CO_2 at 30 °C. The determined isotherm (extended Fritz and Schlünder isotherm) is used for calculation of the theoretical reaction yield and added as line in the figure, showing that reaction yield cannot be effectively enhanced above 100 mg/ml.

Furthermore, the additional adsorption of resorcinol will incrementally reduce the overall reaction speed at higher Dowex® concentrations. For illustration, the reaction yield in the liquid phase is measured for 5 days for various Dowex® concentrations up to 200 mg/ml (Figure 30). As a result, the liquid mole fraction can be reached earlier when less Dowex® is used in the reaction solution. Above 100 mg/ml Dowex®, the equilibrium liquid mole fraction is not yet reached after 5 days, demonstrating the slowing of the enzymatic reaction.

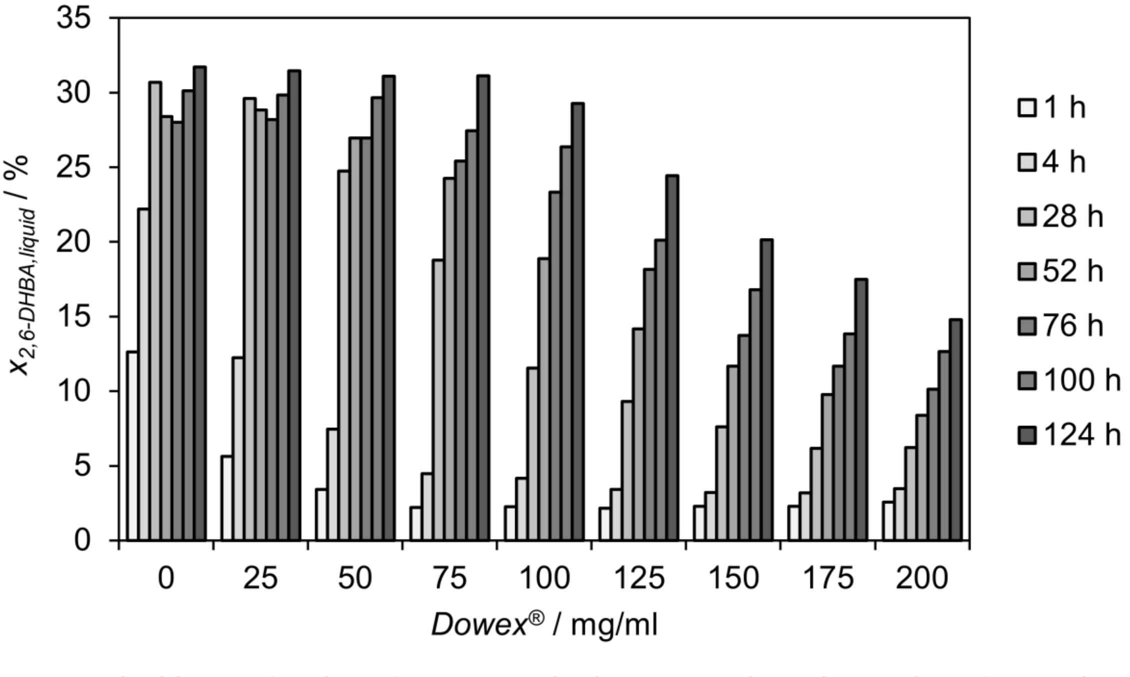

Figure 30: Liquid mole fraction of 2,6-DHBA in the enzymatic carboxylation of resorcinol by 0.139 mg/ml 2,6-DHBD (16.4 U/mg) in aqueous TEA saturated with CO_2 combined with Dowex® 1x8-50 at 30 °C.

Comparing the reaction yield (Figure 31) instead of the liquid mole fraction (Figure 30) of the same experiment, a time-dependent maximum around 50 mg/mL Dowex® can be observed. Even small amounts of adsorber are beneficial for the productivity, which is not visable from the liquid mole fraction data. In contrast, the amount of product bound on the solid phase is required to calculate the reaction yield, which is not directly measurable. Therefore, it is necessarry to find a suitable correlation. Successful application of the extented Fritz and Schlünder isotherm enables calculation of the amount of product adsorbed on the solid phase. Consequently, the reaction yield can be obtained. From the data, it is obvious that an improvement of the productivity can be realized by stepwise addition of Dowex®. In this way, a high reaction rate can be maintained by minimizing the amount of adsorbed phenolic substrate. Simultanously, high reaction yields of above 80 % are possible with Dowex®, improving the biotransformation significantly compared to to reaction system without adsorber.

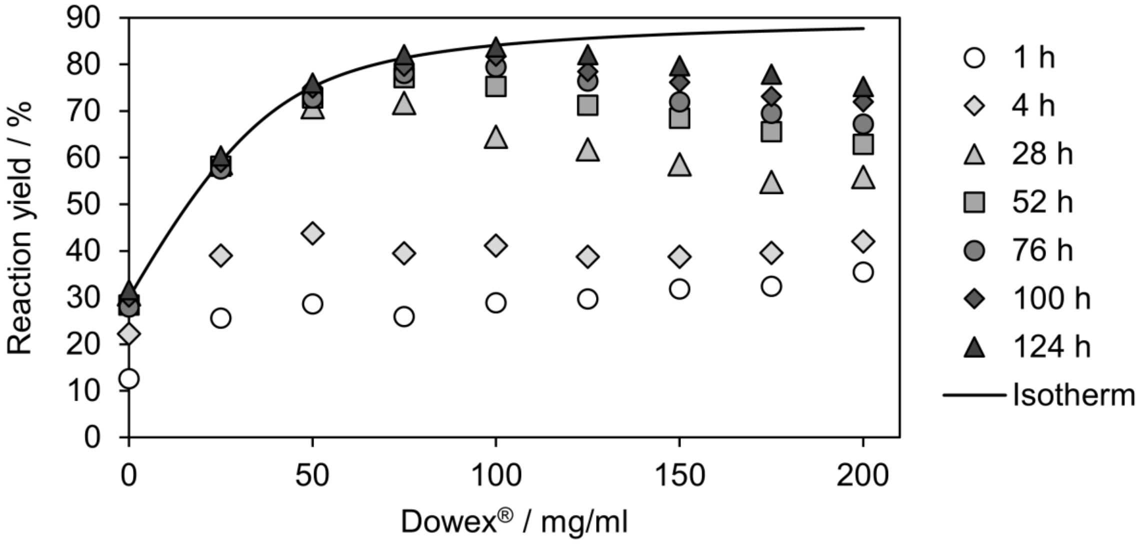

Figure 31: Enhancement of the enzymatic carboxylation of resorcinol in 1 M aqueous TEA saturated with CO_2 by improving the biotransformation with utilization of Dowex® 1x8-50 at 30 °C. The enzymatic carboxylation of resorcinol was performed with 0.139 mg/ml 2,6-DHBD (16.4 U/mg) in aqueous TEA saturated with CO_2 at 30 °C, supplemented with Dowex® 1x8-50. The previously determined isotherm (extended Fritz and Schlünder isotherm) is added, showing that the reactions at high adsorber concentration have not reached their reaction equilibrium after 124 h.

Still, the main challenge of having a competitive adsorption of the phenolic substrate when using Dowex® as adsorber in this biotransformation remains. This effect on the productivity can also be seen in Figure 31, where the reactions at high adsorber concentration have not reached their reaction equilibrium after 124 h, which is indicated by the previously determined isotherm. Furthermore, the reaction yields at higher adsorber concentrations get even lower, when compared at the same reaction time. This demonstrates that optimally, a more selective adsorber needs to be found.

In particular, the styrene-divinylbenzene-based backbone structure of Dowex® is known to adsorb organic species, such as phenols due to hydrophobic bonding [113]. Silica-based anion exchanger can be an alternative with their polar backbone. Already, it was shown that SiliabondTMA® has a higher affinity to 4-methoxybenzoic acid compared to *meta*-methoxyphenol, which, however, only worked efficiently in organic solvent [88]. In aqueous amine solutions, this silica-based anion exchanger may therefore perform more efficiently due to the organic nature of amines. However, an additional limiting parameter is the aqueous bicarbonate concentration, when using strong anion exchanger as bicarbonate is known to adsorb, reducing the capacity for product binding [88]. Nevertheless, strong anion exchanger with different backbone matrices can be tested. The SiliabondTMA® and SiliabondTBA® are expected to perform with a high selectivity. In particular, SiliabondTBA® is promising as it has butylammonium functional groups identical to TBA-Br, which was successfully used for *in situ* product crystallization in Section 2.4. In the same manner, styrene-divinylbenzene-based resins with butylammonium functional groups may perform with a higher selectivity compared to Dowex® 1x8 with its methylammonium functional groups.

2.6. Product Elution and Purification in a Dowex®-Based Downstream Process

After the successful adsorption of 2,6-DHBA on Dowex®, the product needs to be efficiently eluted for further product isolation. In a series of elution experiments, the mixture of an organic solvent supplemented with 1 M HCl elutes resorcinol and 2,6-DHBA with sufficient efficiency from the adsorber. In this process, HCl provides chloride ions to compete with the bound 2,6-DHBA, which are negatively charged, too. However, 2,6-DHBA has a low solubility in aqueous HCl solutions. Therefore, an organic solvent is used to ensure a high solubility of resorcinol and 2,6-DHBA. As a suitable, but not yet optimized eluent, 1 M HCl in methanol is used for further product isolation. After elution, vacuum distillation is used to remove and recycle the organic solvent, which results in precipitation of 2,6-DHBA due to low solubility in aqueous HCl. Additional washing steps with 1 M HCl are performed to remove resorcinol and other side products. By this, pure 2,6-DHBA is obtained. Side products usually form by oxidation reactions, which can be minimized by oxygen removal [35].

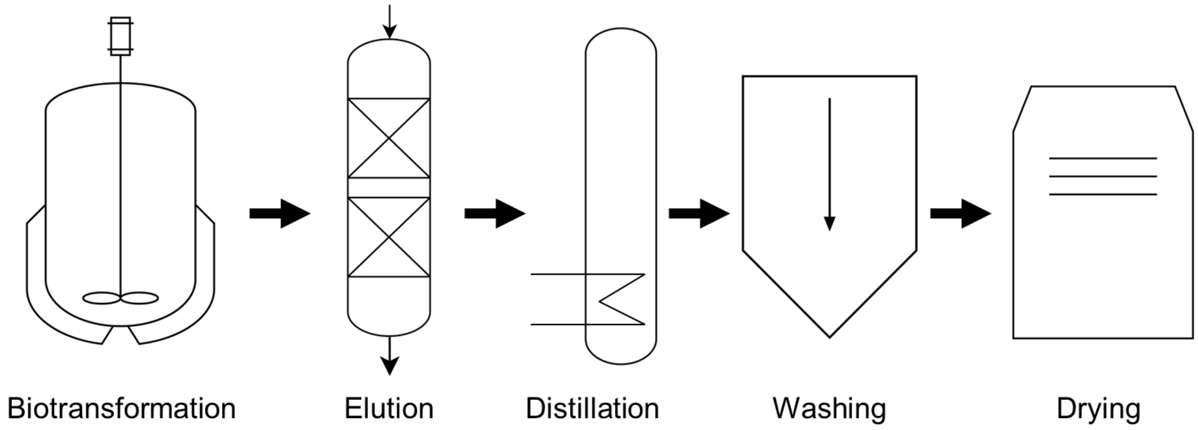

Figure 32: First concept for a Dowex®-based ISPR with subsequent downstream processing to obtain 2,6-dihydroxybenzoic acid.

In a 30 ml biotransformation of 80 mM resorcinol in 1 M aqueous TEA presaturated with CO_2, the applicability of this method is further investigated. After reaching a product yield of 20.4 % without continuous CO_2 gassing, the medium is taken and added to 0.5 g Dowex® 1x8-50 in a chromatography column for product adsorption. Afterwards, product isolation was performed as previously described. The mass balance analysis of this preliminary downstream processing shows that from the initial 75.5 mg 2,6-DHBA in the medium, 32.8 mg (43.4%) product crystals were obtained. HPLC analysis of the liquid solutions shows that the rest of the product remains with 36.9% in the reaction medium and 8.3% in the washing fraction of 1 M HCl. Consequently, 11.4% product was not dissolved in the liquid phases, which means that the remaining product is still bound on Dowex® or is lost due to side-product formation. The purity of the product was determined based on HPLC analysis and showed a 98.9% 2,6-DHBA purity with only 1.1% residual resorcinol. The high amount of unbound 2,6-DHBA can be reduced by further addition of adsorber. The elution with 1 M HCl in methanol proves to be already very efficient as 91.7% of resorcinol and 2,6-DHBA is recovered from the adsorber. Optimization of the elution, especially in regards to the total applied elution volume and flow rate is expected to reduce the remaining fraction of bound product. In this small-scale experiment, gravity column chromatography was utilized, preventing adjustment of the flow rate.

2.7. Lab-Scale Biotransformation of Resorcinol

The previously gained knowledge and improvements for the enzymatic carboxylation of resorcinol in aqueous TEA are used to investigate the reaction system in a lab-scale biotransformation. For this, the reaction is performed in a 3 l double jacket glass reactor fitted with three baffles and a single propeller stirrer for improved mixing. The complete experimental set-up is shown in Figure 33. For a higher productivity, the adsorber is added stepwise to maintain the liquid mole fraction of 2,6-DHBA below 10% in order to achieve first order kinetics. Alternatively, the process can be performed in a differential reactor set-up, where the reaction medium is continuously pumped through a packed-bed of adsorber. However, the competitive adsorption of resorcinol on Dowex® reduces the enzyme activity to the full extent, similar to having 100 mg/ml adsorber in the biotransformation. Additionally, pumping of the medium, which includes the enzyme, is known to deactivate enzymes in pumps that introduce high shear stress, such as piston pumps [114]. Contact with the pump can be prevented by utilization of an ultrafiltration membrane to immobilize the enzyme in the stirred tank reactor. An even further improvement can be achieved with immobilized enzyme on suspended carriers. For the separation of carriers instead of dissolved proteins, membranes with bigger pores can be used, decreasing the required energy for pumping as the pressure drop is reduced. However, required enzyme immobilization needs first to be establishment with sufficient efficiency and stability. Therefore, the easiest approach to perform the lab-scale biotransformation is done with the direct stepwise addition of adsorber.

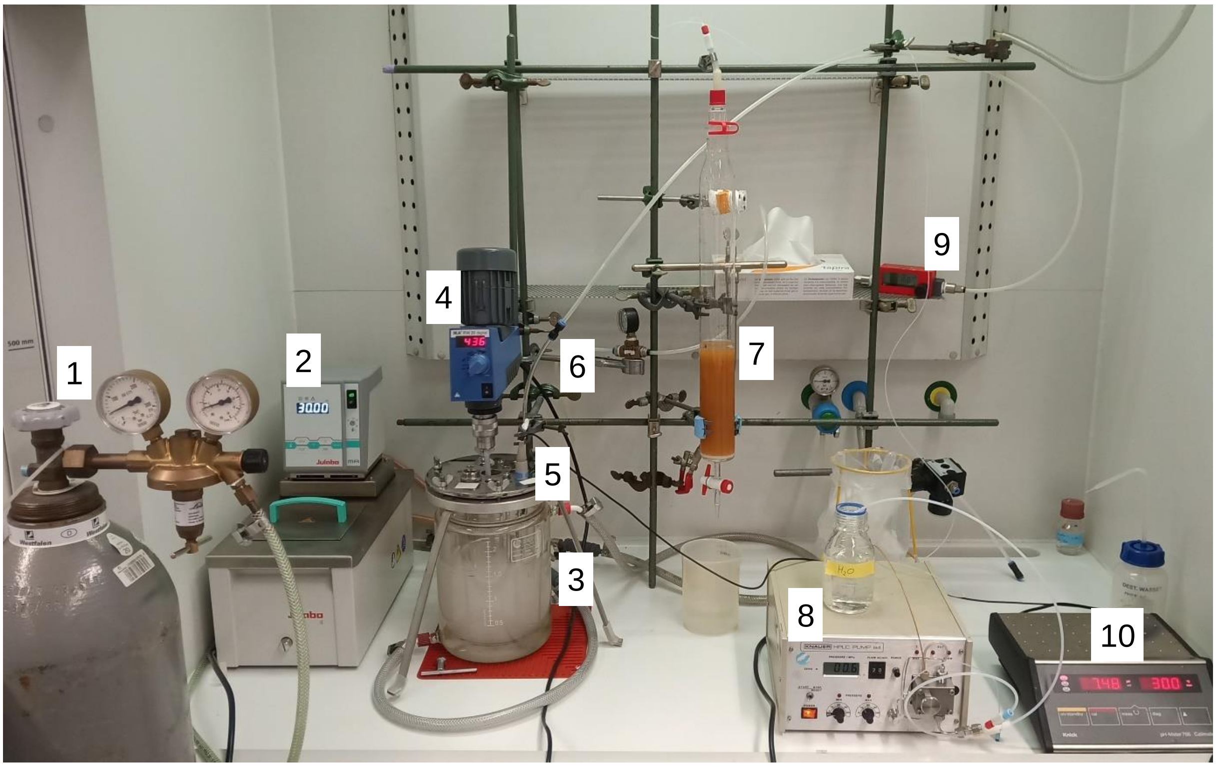

Figure 33: Set-up for the enzymatic carboxylation of resorcinol with subsequent chromatographic product isolation. 1) CO_2 supply; 2) Thermostate; 3) 3 L stirred tank reactor with baffles; 4) Overhead stirrer performing at 436 rpm; 5) pH probe connected to 10), pH meter; 6) Adapter connected to a 0.5 µm porous CO_2 sparger; 7) Chromatography glass column containing the Dowex® 1x8-50 in the process of washing; 8) Piston pump connected to 7), the chromatography column; 9) Mass flow meter.

During the reaction, the liquid concentration of resorcinol and 2,6-DHBA is measured, which is used to calculate the liquid mole fraction of 2,6-DHBA (Figure 34) and the reaction yield (Figure 35). Again, the reaction yield is calculated with the extended Fritz and Schlünder isotherm correlation, obtained in Section 2.5. Based on these results, the initial enzyme activity is calculated to be 18.4 U/mg. The high enzyme activity is successfully maintained for an extended period of time by the stepwise addition of Dowex®. However, after reaching a reaction yield of approximately 40% after 4 days, addition of adsorber did not improve the productivity to a huge extent anymore. This is primarily caused by the competitive binding of resorcinol, reducing the substrate concentration and thereby lowering the activity based on kinetics. Furthermore, deactivation of the biocatalyst occurred, which reduced the overall enzyme activity. This is confirmed by performing a repetitive batch (Figure 37), where the medium is reused after separation of the adsorber. In this biotransformation, deactivation can occur, among other effects, by stirrer-introduced shear forces, interaction of the enzyme with the bubble interface [115], temperature [74] and contact with resorcinol [35]. Furthermore, it is possible that proteases contributed to the decrease in activity. Cell-free extract was utilized, which can have proteases present in contrast to preparations of purified enzyme. Regarding temperature, 2,6-DHBD is known to be relatively stable to temperature with only minimal deactivation occurring above 60 °C when incubated for 30 min [74]. In contrast to enzyme deactivation, reversible binding of the enzyme to the adsorber can occur. Anion exchanger are known to bind proteins, which is generally influenced by the isoelectric point of the proteins [116]. The adsorption on the material can reduce the enzyme activity, but can also retain activity. The occurrence of enzyme adsorption is supported by the appearance of floating protein precipitate on top of the chromatography column after product elution with 1 M HCl in methanol. It is expected that during the product elution, the acidic and organic conditions lead to the denaturation of present enzyme.

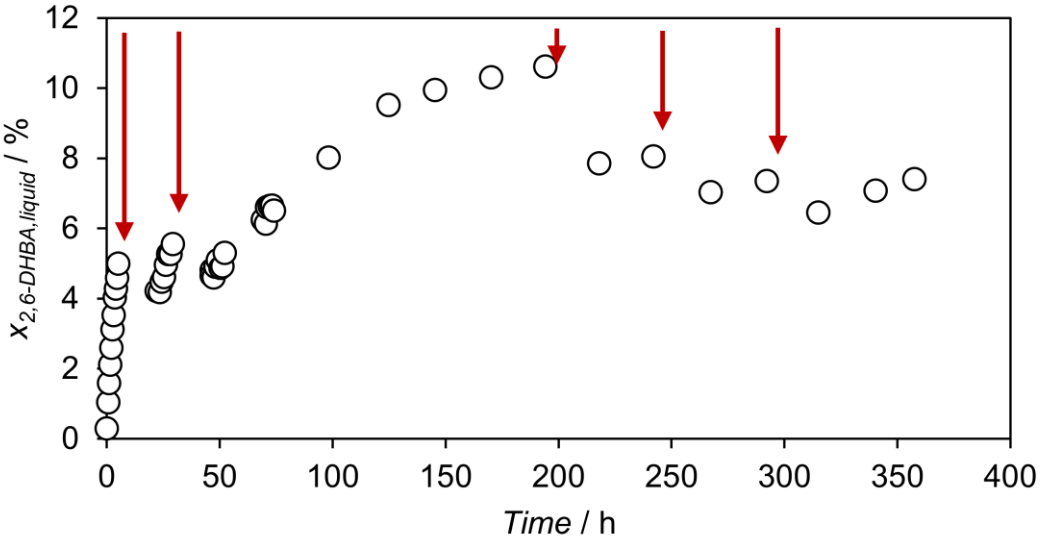

Figure 34: Liquid mole fraction of 2,6-DHBA for the enzymatic carboxylation of 80 mM resorcinol in 1 M aqueous TEA saturated with CO_2 with stepwise addition of Dowex® 1x8-50 in a 3 L stirred tank reactor with baffles. In each step (indicated by red arrows), 30 g Dowex® are added to the 1.5 L reaction medium containing 64.2 mg/l 2,6-DHBD cell free extract. The medium was stirred at 436 rpm, heated to 30 °C and continuously aerated with 20 ml/min CO_2 through a 0.5 µm porous sparger.

After addition of Dowex® to a final concentration of 100 mg/ml, the reaction was incubated additional two hours for final product adsorption. The adsorber was then harvested and transferred into a glass column for product elution according to the establish protocol in Section 2.6. During the addition of eluent, bound bicarbonate formed gaseous CO_2 due to the acidic condition. This complicates the elution at lab-scale as the packed bed gets continuously disturbed until the CO_2 degassing is completed. It is expected that pumping of the eluent from bottom to top performs better as undesired channeling due to gas pocket formation can be minimized. For future work, the possible build-up of pressure in the chromatography column needs to be considered to prevent equipment failure. The utilized open chromatography column, ensured gas leakage and prevented build-up of pressure inside the glass column. Furthermore, the desorbed CO_2 can be recycled in an optimized process. Thereby, it can be used for gassing of the reaction medium.

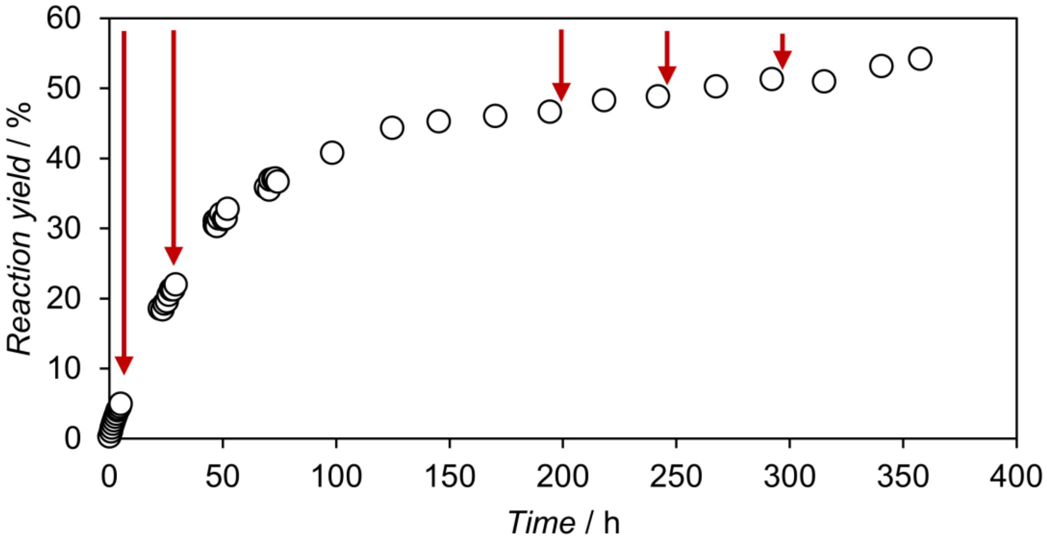

Figure 35: 2,6-DHBA reaction yield for the enzymatic carboxylation of 80 mM resorcinol in 1 M aqueous TEA saturated with CO_2 with stepwise addition of Dowex® 1x8-50 in a 3 L stirred tank reactor with baffles. In each step (indicated by red arrows), 30 g Dowex® are added to the 1.5 L reaction medium containing 64.2 mg/l 2,6-DHBD cell free extract. The medium was stirred at 436 rpm, heated to 30 °C and continuously aerated with 20 ml/min CO_2 through a 0.5 µm porous sparger.

The eluted product mixture was concentrated by vacuum distillation in a glass flask. In this process, the separated solvent was recycled for further product elution minimizing the required eluent volume and waste. In total, 1 L of 1 M HCl in methanol was necessary for product elution. Figure 36 A shows the precipitate before the first washing step with 1 M HCl. It is assumed that the dark color is caused by side-products, which are mainly known to occur due to the oxidation of phenols [35]. These side-products are visible in the HPLC chromatograms as additional peaks with variable retention times above 9 min. Due to the higher retention time, analysis of the resorcinol peak at 7.1 min and 2,6-DHBA peak 8.4 min are not impaired. Repeated washing with 1 M HCl removed leftover resorcinol and side-product, bleaching the residual 2,6-DHBA precipitate as shown in Figure 36 B. After sufficient washing and subsequent drying at 40 °C, 2,6-DHBA powder is obtained with a purity above 99.8%. Before drying, the wet 2,6-DHBA has a slightly pinkish color, which turns in the final product to a slightly greyish color as shown in Figure 36 C. In total, 6.71 g 2,6-DHBA was obtained from the biotransformation. The ratio of isolated product from the reaction medium is significantly improved as shown in the following.

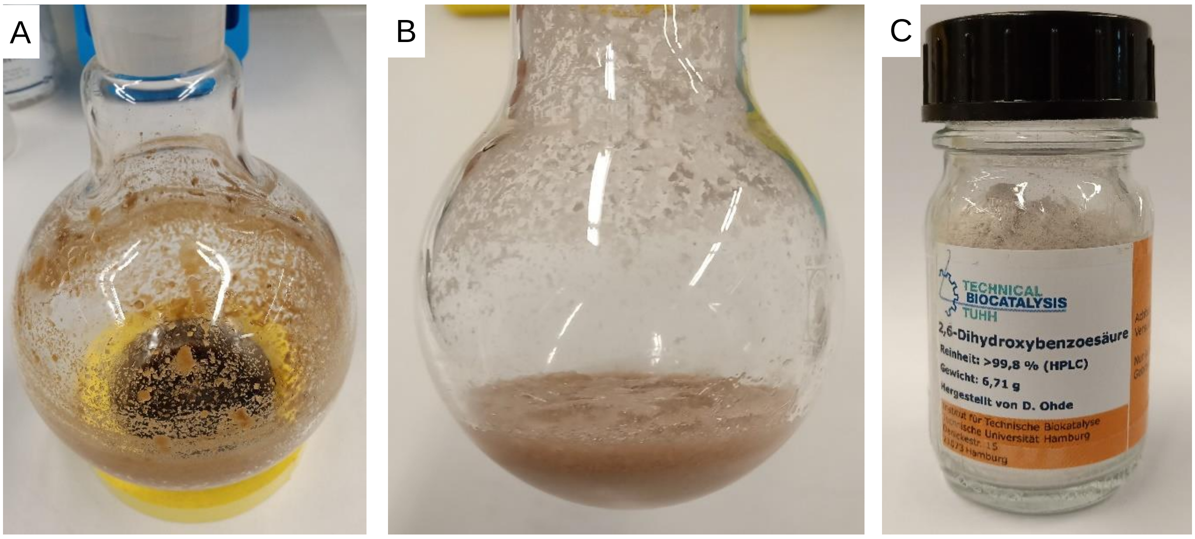

Figure 36: Purification status of 2,6-DHBA eluted from Dowex® 1x8-50. Following the downstream processing, 1) shows the precipitate from the elution fraction, 2) shows the 2,6-DHBA precipitate after washing with 1 M HCl and 3) shows the isolated and dried product in a glass bottle.

In the biotransformation of 30 ml scale, presented in Section 2.6, 43.4% of the product were isolated. In comparison, 66.9% was isolated in the 1.5 L biotransformation, which means that 6.71 g 2,6-DHBA powder is obtained from 10.03 g dissolved and adsorbed product in the reaction medium. This percentage is primarily improved due to the use of 100 mg/ml instead of 16.7 mg/ml Dowex®. Further improvements can be easily implemented by performing a second chromatographic run by adsorption of the leftover product in the reaction medium as well as improvement of the washing steps. Moreover, for enhancement of the reaction yield, a higher total enzyme activity can be applied. In theory, addition of 100 mg/ml Dowex® enables a reaction yield of 84%. However, only a total enzyme activity of 1772 U is employed in the 1.5 L biotransformation, which is expected to be the main reason of not reaching the expected yield in a timely manner. In turn, application of a low amount of enzyme resulted in a high biocatalyst yield of 69.7 $g_{product}$ / $g_{catalyst}$. The biocatalyst yield gives a measure about the mass of product produced per mass of enzyme preparation used over its lifetime. Biocatalyst yield is synonymous to the term ‘productivity number’, which Bommarius uses [117]. In contrast, John Woodley is using the term biocatalyst yield increasingly in his recent publications [118]. In principle, the biocatalyst yield is the total turnover number redefined on a mass basis, which makes it more practical when dealing with impure enzyme preparations. Since a crude enzyme extract is used for the lab-scale biotransformation, this parameter is calculated. An achieved biocatalyst yield of 69.7 g/g places the process in the fine chemical sector as provided by Woodley’s earlier publication on the cost analysis for catalyst production in biocatalytic processes[119]. In this fine chemical sector, a free enzyme preparation usually costs between 1000-2500 €/kg enzyme. Using this range, the cost of the biocatalyst would be in the range of 14.35 to 35.87 € to produce one kilogram of 2,6-DHBA. This is promising, when taking the price difference of resorcinol (Table 4) and 2,6-DHBA (Table 5) into account.

Table 4: Selection of commercially available resorcinol. Prices are given either as DDP (Delivered Duty Paid) or FOB (Free On Board) as defined in the Incoterms by the International Chamber of Commerce.

Seller	*Unit / kg*	*Unit Price*	*Price per kg*	*Quality*	*Average Price per kg*
Tokyo Chemical Industry Co Ltd, Japan	0.5	66.00 €	132 €/kg	99%	152.00 €
Sigma-Aldrich / Merck KGaA, Germany	0.5	86.00 €	172 €/kg	99%	(DDP)
Cemo Technology Develop Co Ltd, China	1	15.00 $	15 $/kg	99%	
Cemo Technology Develop Co Ltd, China	1	20.00 $	20 $/kg	99%	20.00 $
Sinoright International Trade Co Ltd, China	1	15.00 $	15 $/kg	99%	(FOB)
Jiangsu Ambition New Materials Co Ltd, China	1	30.00 $	30 $/kg	99%	

Table 5: Selection of commercially available 2,6-dihydroxybenzoic acid. Prices are given either as DDP (Delivered Duty Paid) or FOB (Free On Board) as defined in the Incoterms by the International Chamber of Commerce.

Seller	*Unit / kg*	*Unit Price*	*Price per kg*	*Quality*	*Average Price per kg*
Thermo Fisher Scientific Inc, USA	0.5	437.00 €	874 €/kg	98%	743.00 €
Santa Cruz Biotechnology Inc, USA	0.5	306.00 €	612 €/kg	n/a	(DDP)
Henan Kingway Chemicals Co Ltd, China	1	100.00 $	100 $/kg	98%	125.00 $
Hebei Mojin Biotechnology Co, Ltd, China	1	150.00 $	150 $/kg	99%	(FOB)

Based on these prices, 2,6-DHBA is 4.9 times (DDP prices) or 6.3 times (FOB prices) as valuable as resorcinol, leaving room for process costs. For the following calculations, only the FOB prices are considered as these are closer to the expected bulk prices of the chemicals and give a more conservative cost estimation. For 1 kg of 2,6-DHBA, around 1.1 kg resorcinol are required based on the lab-scale biotransformation as the isolated yield is still limited at 66.9%. Adding the resulting resorcinol costs of 22 $/kg to the biocatalyst cost of 35.87 €/kg (~42.40 $/kg), both components contribute around 64.40 $ to the costs. It is expected that this leaves sufficient room to cover all remaining costs as these are the major cost contributors. Additional costs, such as costs for the personal, remaining material and electricity are not yet specified. However, due to the downstream process being simple and solvents, such as TEA and methanol being mostly reusable as demonstrated, the costs are estimated to be low. Therefore, it seems reasonable that the reaction can be profitable.

In this cost estimation, the calculations heavily rely on the biocatalyst yield, which should be confirmed in additional experiments. This value should also be used with caution as it is only achieved when the reaction is run for a long time (>14 days), which is not practical for industrial applications. A much higher enzyme loading would be necessary to increase the productivity. However, this decreases the biocatalyst yield and makes the process not practical from a different perspective. Therefore, further optimization needs to be performed.

One of the major advantages performing the enzymatic carboxylation in aqueous amine solution is that the reaction medium including the enzyme can be reused. This is proven by utilization of the reaction medium of the first batch in a second batch without addition of fresh enzyme. In the second batch, which is shown in Figure 37, only 0.60 U/mg initial activity remained. This corresponds to a 96.8% decrease in initial activity. Due to leftover substrate and product in the reaction medium, the liquid mole fraction starts at 0.8. Remarkable is that the addition of Dowex® after 24 h doubled the remaining activity to 1.21 U/mg, demonstrating the benefit of using an ISPR, even if it is still imperfect.

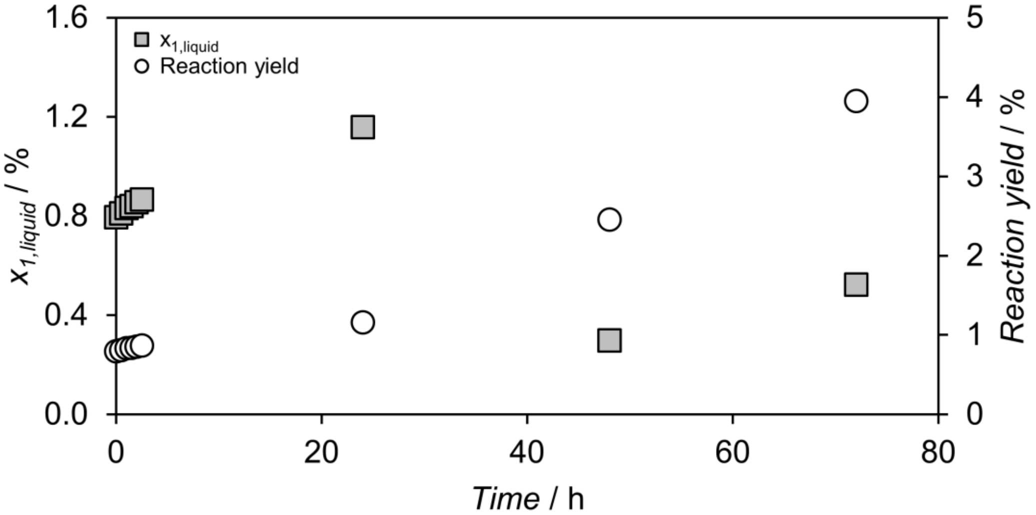

Figure 37: Second batch of the enzymatic carboxylation of 80 mM resorcinol in 1 M aqueous TEA saturated with CO_2 in a 3 L stirred tank reactor with baffles. After 24 h, 30 g (20 g/l) Dowex® 1x8-50 is added to the 1.5 L reaction medium containing 64.2 mg/l 2,6-DHBD cell free extract. The medium was stirred at 436 rpm, heated to 30 °C and continuously aerated with 20 ml/min CO_2 through a 0.5 µm porous sparger.

In summary, it is demonstrated that the enzymatic carboxylation of resorcinol is enhanced in aqueous TEA and is further improved by the application of a Dowex®-based ISPR approach. The reusability of the reaction medium including the dissolved amine is shown, which is essential for adsorption of gaseous CO_2, thereby providing the C1 substrate for the biotransformation. For obtaining pure 2,6-DHBA powder, a simple downstream processing is established, where the recycling of the adsorber and solvent for product elution is shown. Overall, no special equipment, e.g. for pressurization is required as the reaction is best performed at ambient CO_2 conditions. At elevated CO_2 pressure, the enzyme activity is negatively affected, presumably due to carbamylation occurring on the enzyme structure. As consequence of not requiring a pressure reactor, an efficient gassing technique is only required for optimal mass transfer of the gaseous CO_2 into the liquid reaction medium. CO_2 gassing of aqueous TEA and its different effects, which impact not only the gassing efficiency, but also the biotransformation itself, are investigated and presented in Chapter 3.

3. CO_2 Microbubble Gassing of Aqueous Triethanolamine

3.1. Effects of the CO_2 Saturation Level on the Gassing

The biocatalytic carboxylation of phenols by reversible decarboxylases in aqueous amine solutions has the major advantage to utilize gaseous CO_2 as substrate. However, the gaseous CO_2 is not directly used as it first has to be dissolved in the liquid medium to be accessible for the biocatalyst. Therefore, CO_2 gassing and subsequent saturation plays a major role in the aqueous amine system. More specifically, the CO_2 gassing needs to be efficient to reduce the waste of unreacted CO_2 and its involved emission. Furthermore, the saturation process can be shortened by designing an efficient gassing, which enables reaching the optimal pH and CO_2 loadings to start the process. In general, amine solutions are alkaline in nature, and need to be neutralized by CO_2 saturation to prevent biocatalyst deactivation. For example, the pH shifts from an initial value of 10.8 to 7.5 during CO_2 saturation of an aqueous 1 M TEA solution without biocatalyst at 30 °C. Already during this process a peculiarity is observed regarding the foaming behavior. Approaching CO_2 saturation of a 1 M aqueous TEA solution, increased foaming occurs, whereas sparse or no foaming occurs in the initial period of CO_2 gassing. For investigation of this observed effect as well as quantification of the CO_2 mass transfer in the two-phase system, a bubble column equipped with a device to measure bubble size distributions is set up. The concept of the two-phase system investigation is illustrated in Figure 38.

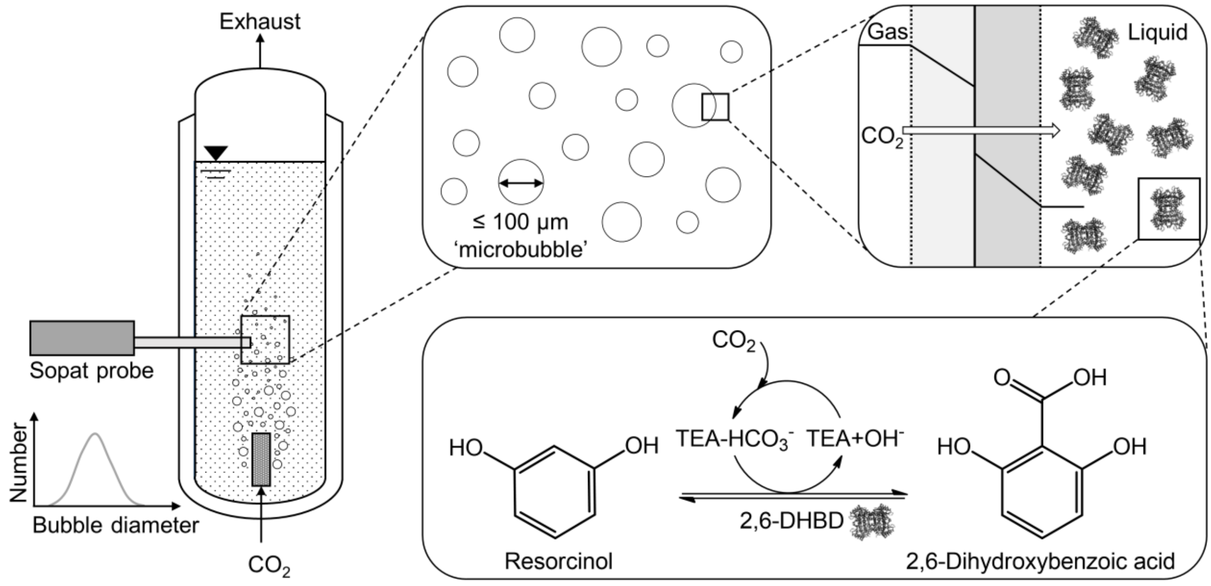

Figure 38: Two-phase biotransformation of resorcinol by 2,6-dihydroxybenzoic acid decarboxylase (2,6-DHBD) in a bubble column with active CO_2 gassing of aqueous triethanolamine (TEA).

For the bubble size distribution measurements, a probe-based microscope by SOPAT GmbH, Germany, is used, which can optically measure bubble sizes in the range from 9-1200 µm. Therefore, this device is suitable to measure even bubbles in the micrometer region. The bubble size distribution (BSD) is determined for different CO_2 saturation conditions to better assess the reason for the changed foaming behavior. For this investigation, the BSD is determined during the initial loading of unsaturated aqueous TEA and compared to the BSD present after reaching the maximum CO_2 saturation, which is indicated by attaining a stable pH. Furthermore, three spargers with mean pore diameters of 0.5, 2 and 10 µm are utilized for the CO_2 gassing to assess the impact on the resulting bubble diameter. Otherwise, the spargers have identical geometric dimensions and are mounted in a 250 ml bubble column. The determined BSD are shown in Figure 39.

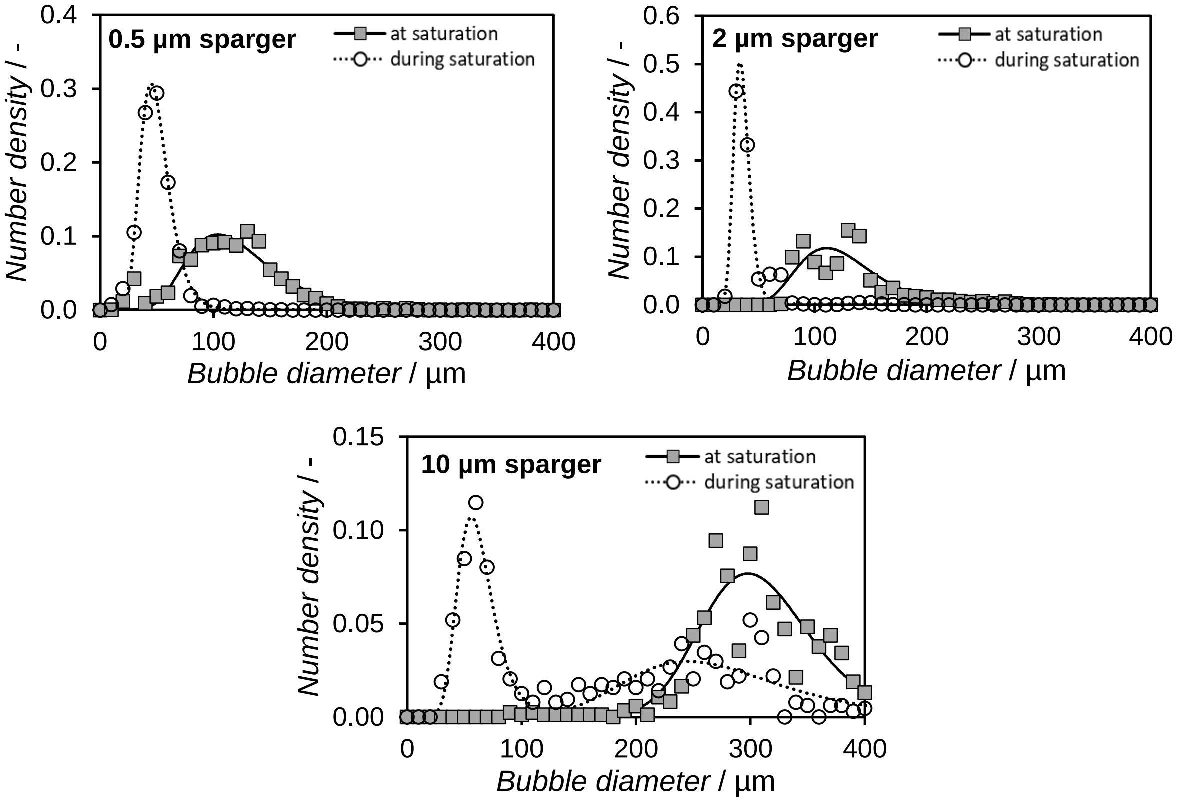

Figure 39: CO_2 bubble size distribution during initial saturation ($S_{CO_2} = 0$) and at saturation ($S_{CO_2} = 1$) of 150 ml 1 M aqueous triethanolamine with 100 ml/min CO_2 using different spargers in a bubble column with an inner diameter of 31.9 mm under ambient conditions. The bubbles were detected with a Sopat-VI Sc probe-based microscope and analyzed by the integrated image analysis software. Log-normal regressions with the following R^2 for CO_2 saturated and CO_2 depleted conditions were calculated, respectively: 0.5 µm sparger: 0.92 and 0.99; 2 µm sparger: 0.81 and 0.98; 10 µm sparger: 0.84 and 0.70 (bimodal).

In the cases of using the three different porous spargers, the BSD in respect to bubble diameter does change with applied sparger pore diameter. The mean Sauter diameter (d_{32}), defined in Eq. 14, is a typical representation of the mean bubble size.

$$d_{32} = \frac{\sum_{i=1}^{N} d_i^3}{\sum_{i=1}^{N} d_i^2} \qquad \text{Eq. 14}$$

The calculated d_{32} of the experimental data is summarized in Table 6. It can be seen that the bubble diameter increases concurrently with the pore diameter for both CO_2 saturation scenarios. This is in agreement with BSD measurements in non-coalescing systems, whereas bubble sizes in coalescing systems are largely independent of the sparger pores due to coalescence on the spargers surface [120]. Overall, the 0.5 µm and 2 µm sparger produce similar BSDs. However, the 10 µm sparger produces much larger bubbles and also shows initially a bimodal distribution, which changes to a unimodal distribution at CO_2 saturation. Both submillibubble peaks of the 10 µm sparger are in the same 300 µm size range, whereas the initial peak bellow 100 µm resembles the peaks in the BSD of the 0.5 µm and 2 µm sparger. Usually, bimodal distributions can be attributed to coalescence phenomena occurring on the sparger's surface [121]. However, all three sparger consist of the same material. Additionally, the bimodal distribution disappears, when mass transfer reaches the equilibrium due to CO_2 saturation. Instead of a coalescence effect on the spargers surface, this could indicate that the initially produced submillibubbles shrink to microbubbles as a result of the mass transport during saturation. Consequently, the submillibubble peak of the 10 µm sparger also decreases from 300 µm to almost 240 µm.

Table 6: Mean Sauter diameter d_{32} for different porous sparger in 1 M aqueous triethanolamine at 100 ml/min CO_2 and 30 °C.

Sparger pore size	CO_2 saturation (S_{CO2})	d_{32} (µm)
0.5 µm	$S_{CO_2} = 1$	144.7
	$S_{CO_2} \approx 0$*	61.3
2 µm	$S_{CO_2} = 1$	157.3
	$S_{CO_2} \approx 0$*	71.1
10 µm	$S_{CO_2} = 1$	277.0
	$S_{CO_2} \approx 0$*	184.3

*The initialization and measuring time prevents practical measurement of the bubble size at $S_{CO_2} = 0$.

Microbubbles show the characteristic to decrease in size during residence as the inner bubble pressure increases, which in turn enhances the mass transfer [122]. The pressure difference between the inside and outside of a gas bubble in a liquid medium can be determined by the Young-Laplace equation (Eq. 15). Here, the pressure difference *Δp*, also called Laplace pressure, is caused by the surface tension *σ* of the interface between gas and liquid. For a bubble with a decreasing radius *r*, the curvature of the boundary layer gets bigger, which increases the inner bubble pressure [122]. In turn, this increases the concentration gradient and mass transfer [122] as the pressure is linked to Henry's law [123]. According to Henry's law, the partial pressure difference is the driving force for the mass transfer, which is expected to be the fundamental reason for the shrinking and quick dissolution of microbubbles [122,124]. Additionally, an increase of the mass transfer coefficient k_L is expected to occur for microbubbles, which is in agreement with the Ranz and Marshall's correlation in a recent study. [125] In this study of Tanaka *et al*. (2020), the shrinking of single freely rising bubbles in the micrometer range at different air saturation levels was investigated. In consequence of this accelerated shrinking of bubbles in the micrometer range, it is possible that the measured microbubble peak for the 10 µm sparger generated in the same manner during initial CO_2 gassing. In comparison to microbubbles, macrobubbles usually increase in size during their rising to the liquid surface, because of the decreasing hydrodynamic pressure. Consequently, the rapid shrinking of microbubbles can ensure that they will not reach the liquid surface to burst or generate foam due to complete dissolution. Therefore, the possibility for complete dissolution of microbubbles during their slow rise to the surface results in less foaming as less bubbles reach the surface. This explains the observation of a different foaming behavior, when gassing 1 M aqueous TEA with CO_2 to reach CO_2 saturation.

$$\Delta p = \frac{2 \cdot \sigma}{r} \qquad \text{Eq. 15}$$

In contrast to experiments with single freely rising bubbles as performed by Tanaka *et al.* (2020), high bubble concentrations are achieved when using porous spargers which requires consideration of coalescence effects in bubbly flows. The decreasing bubble diameter in the BSDs of CO_2 unsaturated aqueous TEA solutions would emphasize that coalescence plays a minor role to increase the bubble size during initial CO_2 saturation. Instead, the accelerated dissolution assisted by the Laplace pressure may be dominant. Even though coalescence is reported to occur for air bubbles in water [126], the lower zeta potential of CO_2 bubbles compared to air bubbles [127] can suppress coalescence. In general, reducing the bubble size decreases the zeta potential [128]. This is expected to enhance the repulsion of the negatively charged bubble surfaces, which in turn diminishes coalescence of microbubbles [129]. At the same time, reduced coalescence stabilizes potential foam due to less bursting of bubbles [130]. However, this microbubble property can also lead to increased formation of stable foam, if the bubbles reach the liquid surface. In our recent study, we demonstrated that less foam formation is observed for microbubble aeration due to the more efficient mass transfer, which required lower gassing rates [131]. In the case of CO_2 gassing of aqueous TEA, the pH is lowered from highly alkaline condition to a more neutral value. As a result of the lowered pH, the zeta potential of microbubbles increases [128]. Furthermore, is was shown that the zeta potential of microbubbles is dependent on the pH with changes from -110 mV above pH 10 to positive values below pH 4.5 [128]. Therefore, the pH change from 10.8 to 7.5 for the CO_2 gassing of 1 M aqueous TEA enhances coalescence. This phenomenon is expected to contribute to the increasing bubble diameter in the measured BSD reaching CO_2 saturation (Figure 39). In addition, it supports the hypothesis that the microbubble peak for the 10 µm sparger forms as a result of having bubbles near the microbubble region shrinking. Further analysis of potential microbubble dissolution is investigated in the next section (Section 3.2) by simulating the mass transfer.

3.2. Simulating the Shrinking of Microbubbles

The shrinking of microbubbles is further investigated by simulating the mass transfer for different CO_2 saturation conditions of 1 M aqueous TEA. This can support the previous finding that in the CO_2 depleted TEA solution, mass transfer causes shrinking of microbubbles whereas coalescence is responsible for an increase in bubble diameter in CO_2 saturated TEA. For the simulation, different aspects of the mass transfer need to be considered. Regarding the theoretical rising velocity v of macrobubbles, the classical approach of using the Stokes law (Eq. 16) is usually applied [132]. This incorporates the bubble diameter (d_B), gravitational constant (g), densities of the gas (ρ_g) and liquid (ρ_l) as well as the dynamic viscosity (η).

$$v = \frac{{d_B}^2 \, g \, (\rho_g - \rho_l)}{18 \, \eta} \qquad \text{Eq. 16}$$

However, microbubbles cannot be treated as rigid particles even though they appear nearly spherical as it causes slight errors [133]. Furthermore, the influence of convection on mass transfer decreases in the microbubble region, making diffusion the dominating process. Overall, the diminished ability of the fluid surface to support tangential stress and the inner circulation within the bubble causes them to have slightly higher rising velocities compared to a solid particle described by Stokes law [132]. Therefore, the Hadamard-Rybcynski interpretation of Naiver-Stokes, which takes the boundary condition, the internal viscosity and the dispersive phase into account, was shown to match experimental results closer [132,134,135]. For the simulation of different initial saturation conditions of the 1 M aqueous TEA, the mass transfer simulation is performed according to Iwakiri *et al.* (2017) [122]. In respect to the saturation, aqueous TEA solutions are usually prepared involving vigorous mixing to homogeneously dissolve TEA in water. This causes the solution to be saturated with air oxygen and nitrogen. Afterwards, no further degassing is performed. Therefore, the assumption of having an air saturated aqueous TEA solution as starting condition is reasonable. For the simulation, the saturation S is defined as

$$S = \frac{c}{c^*}, \qquad \text{Eq. 17}$$

where c is the dissolved gas concentration and c^* is the maximum solubility of the gas. This way, air and CO_2 saturated solutions reach $S_{air} = 1$ and $S_{CO2} = 1$, respectively. In Table 7, the simulation parameter and physical properties are summarized.

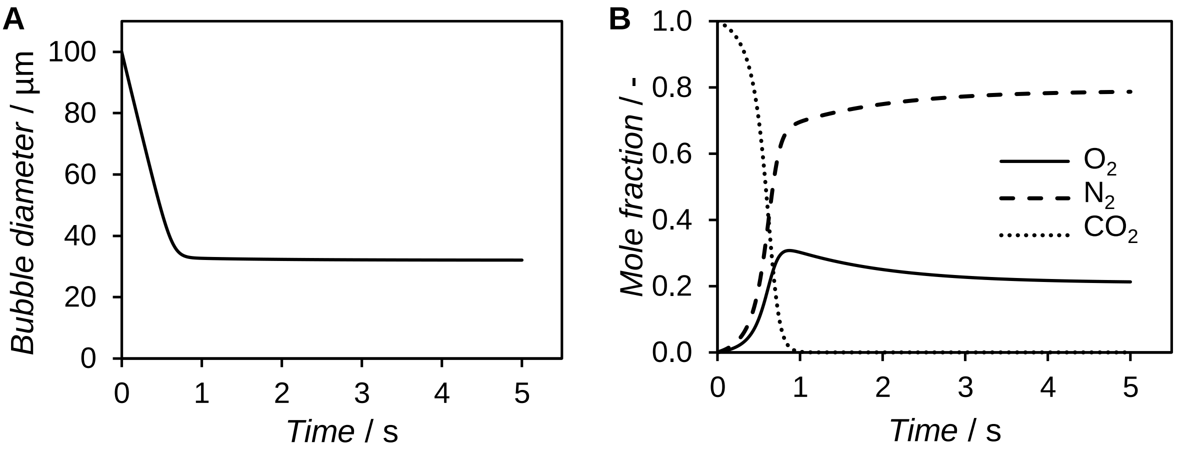

Figure 40: Simulated shrinking of a 100 µm CO_2 bubble with change of bubble diameter (A) and change in the inner bubble mole fraction (B) for CO_2 gassing in 1 M aqueous triethanolamine at 30 °C and 101.3 kPa. The simulation was performed with Matlab, where the initial saturation level of the solution was set to $S_{air} = 1$ and $S_{CO2} = 0$.

As shown in Figure 40, the diameter of a 100 µm CO_2 bubble decreases rapidly in the air saturated medium. From the simulation, it is clear that the bubbles gas volume is exchanged and equilibrated with air oxygen and nitrogen (Figure 40 B). This stabilizes the bubble size preventing further rapid shrinking. However, the bubble still shrinks, which causes it to completely dissolve after 29.1 s due to the increasing Laplace pressure. It is calculated that the bubble rises approximately 8.5 mm before complete dissolution is achieved. Therefore, it is not reaching the liquid surface, which would require rising 152 mm, before dissolution. When simulating the mass transfer for air saturated condition ($S_{air} = 1$), only CO_2 bubbles above 194 µm would reach the liquid surface. In contrast, CO_2 saturated ($S_{CO2} = 1$) 1 M aqueous TEA slows the mass transfer resulting in CO_2 bubbles above 140 µm reaching the liquid surface before dissolution. Here, the mass transfer is primarily occurring due to the increasing Laplace pressure. Taking the determined BSD (Figure 39) from the bubble column experiments into account, it is clear that only for CO_2 saturated conditions a significant amount of bubbles reaches the liquid surface. Therefore, these bubbles have the potential to produce foam. This drastic change in required bubble diameter to reach the liquid surface from 194 µm to 140 µm supports the observation of increased foaming when reaching CO_2 saturation in the bubble column experiments.

Table 7: Parameter and physical properties for the mass transfer simulations in 1 M aqueous triethanolamine.

Simulation parameter	Value	Literature[25-29]
Reactor height h [m]	0.152	
Atmospheric pressure p_{atm} [Pa]	$1.013 \cdot 10^5$	
Temperature T [K]	303.15	
Surface tension σ [N/m]	$62.8 \cdot 10^{-3}$	Vázquez *et al.*, 1996
Dynamic viscosity η[Pa s]	$1.2659 \cdot 10^{-3}$	Ko *et al.*, 2001
Liquid density ρ_l [kg/m^3]	1018.2	Ko *et al.*, 2001
Henry's constant $H(CO_2)$ [mol/m^3/Pa]	$3.46 \cdot 10^{-4}$	Danckwerts, 1966
Henry's constant $H(O_2)$ [mol/m^3/Pa]*	$1.2 \cdot 10^{-5}$	Sander, 2015
Henry's constant $H(N_2)$ [mol/m^3/Pa]*	$6.4 \cdot 10^{-6}$	Sander, 2015
Diffusion coefficient $D(CO_2)$ [m^2/s]	$1.14 \cdot 10^{-9}$	Ko *et al.*, 2001
Diffusion coefficient $D(O_2)$ [m^2/s]*	$2.2 \cdot 10^{-9}$	Himmelblau, 1964
Diffusion coefficient $D(N_2)$ [m^2/s]*	$2.0 \cdot 10^{-9}$	Himmelblau, 1964

*values for gas properties in pure water

Additionally, the mass transfer simulation is used to predict the theoretical BSD from the determined BSD at CO_2 saturation utilizing the 0.5 µm sparger. Here, the resulting BSD is time-dependent and it is shown that the main change in the BSD is happening in the first second as shown in Figure 41. For better comparison, the number densities are normalized by applying a multiplication factor, so that all bubble size distributions display the same peak height. During the first second of simulated mass transfer, the BSD shifts rapidly to smaller bubbles. In consequence, measuring of the initial BSD is demonstrated to be a major challenge. To emphasize this, it takes already 0.5 s to obtain 200 pictures for the Sopat measurement. In this short time frame, the BSD is expected to change significantly as shown in Figure 39. The time for measurement can be further reduced by limiting the amount of pictures. However, the initialization time of the measurement is actually the biggest obstacle as there is a time delay after the start of the CO_2 gassing to ensure the formation of a uniform multiphase flow.

Nevertheless, a simulated BSD between 0.5 s and 1s is in rough agreement with the experimental BSD. Especially, the narrowing of the BSD is replicated in the simulation and consistent with the experimentally obtained BSD for air and CO_2 saturated conditions. In the simulation, it is expected that the more narrow BSD is produced by the counter diffusion of air oxygen and nitrogen, shown in Figure 40 B, which stabilizes the bubble diameter for an extended time during their ascent to the liquid surface.

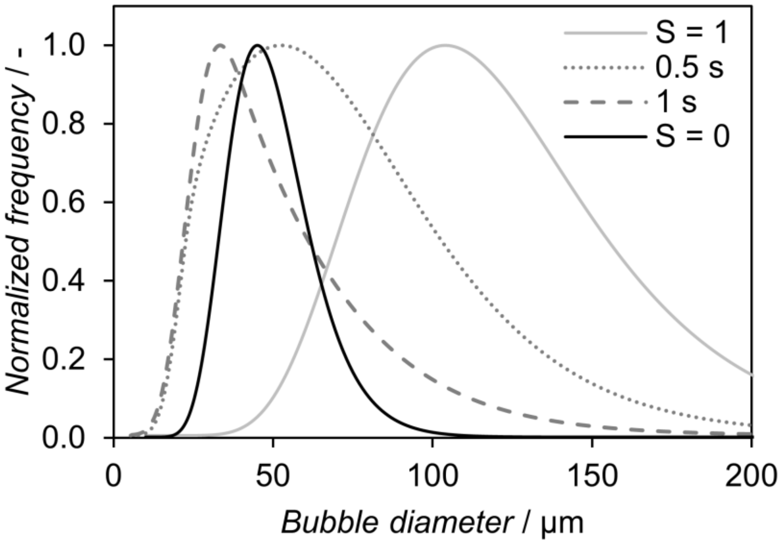

Figure 41: Comparison of experimentally determined and simulated lognormal CO_2 bubble size distribution for different CO_2 saturation levels S_{CO_2} in 1 M aqueous triethanolamine based on the experiments utilizing the 0.5 µm sparger from Figure 39. The simulated distribution changes according to the passed time after bubble formation, which is shown for 0.5 s and 1 s. The bubble number frequency is normalized by applying a multiplication factor, so that all bubble size distributions display the same peak height.

In regard to the BSD resulting from using the 10 µm sparger, the theoretical BSD in the first seconds of CO_2 gassing of CO_2 unsaturated aqueous TEA is simulated. The simulated BSD consists out of 9 BSDs, which are the BSDs simulated in 0.5 second intervals up to 4 seconds including the initial experimentally determined BSD. In this cumulative BSD, which is displayed in Figure 42, all bubbles are removed from the BSD that completely dissolve and reach the liquid surface during their residence time, respectively. In this way, the accumulation of microbubbles and the decrease in frequency of bubbles with larger diameter is attempted to be sufficiently modelled. After the initial shrinking of bubbles, which is primarily achieved during the first second, the size of the microbubbles stabilizes for an extended period as previously shown in Figure 40 for a 100 µm bubble, which only dissolved after 29.1 s. This leads to an accumulation of microbubbles in the bubble column illustrated by the arrow in the microbubble peak (Figure 42). At the same time, this causes the fraction of initially produced bubbles above 200 µm in diameter to decrease. In this way, extending of the simulation time enhances this trend, which is already predominant for every BSD addition up to reaching 4 seconds. It is expected that this trend continues until reaching an equilibrium between bubble formation and bubble disappearance, either due to dissolution or reaching the liquid surface. However, it is important to note that the changes in the CO_2 saturation level are neglected in this scenario, which is a reasonable assumption for the simulation up to 4 seconds. However, saturation level need to be considered for extended simulations.

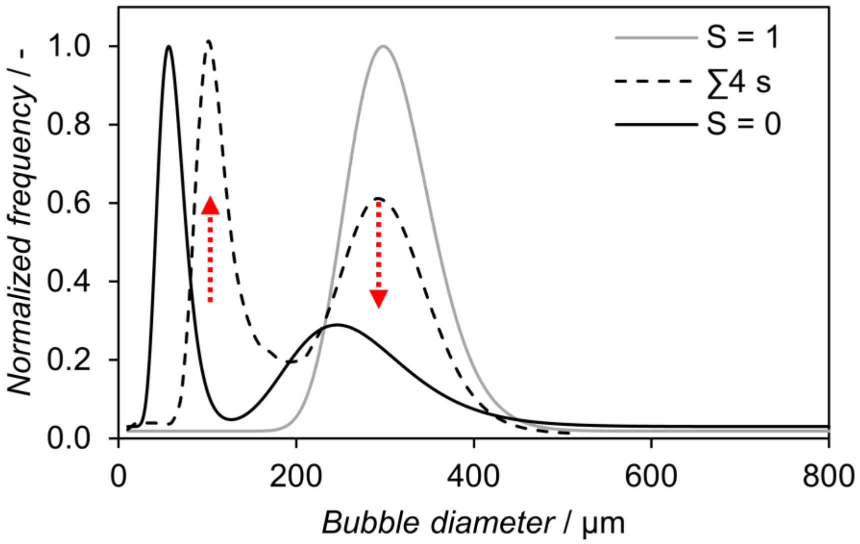

Figure 42: Simulated lognormal CO_2 bubble size distribution (BSD) in comparison to experimentally determined BSD for different CO_2 saturation levels S_{CO_2} in 1 M aqueous triethanolamine based on the experiments utilizing the 10 µm sparger from Figure 39. The simulated BSD represents the sum of the BSD obtained in the first 4 seconds in 0.5 second intervals. The frequency is normalized to the same peak height of the other distributions.

Overall, the previously proposed idea that the mass transfer being responsible for the shift in the BSD to smaller bubbles instead of bubble coalescence and the occurrence of a bimodal BSD are consistent with the Matlab simulations. Still, there are residual differences between the experimental and simulated BSDs. Two major factors contribute to these differences. Firstly, errors in the experimental BSD propagate to the simulation. Secondly, the performed simulations are simplified and neglect additional factors, which affect the mass transfer. In regard to the first mentioned error source, it is assumed that the experimentally obtained BSD are representative for the investigated conditions. The fact that only small differences in the lognormal distributions can be observed in Figure 39 between experimental and fitted data, generally supports this assumption. Still, these errors propagate into the simulation affecting the final simulation by resulting in a difference between experiment and simulation. Furthermore, the exact acquisition of the BSDs in initial CO_2 depleted aqueous TEA is a challenge that needs to be considered in future experiments. As previously discussed, the time delay between start of CO_2 gassing and acquisition of a sufficient amount of pictures for BSD determination is a significant concern for errors in the resulting BSD. Additionally, several effects are neglected in the BSD simulation. For once, the measurement position of the Sopat probe is situated 31.9 mm above the sparger. In this way, some mass transfer already occurs during the rise of bubbles to cover this distance. In contrast, the simulation shows the fate of all bubbles in the initial BSD. In this way, the simulation predicts changes in bubbles of identical lifetimes, whereas the Sopat probe photographs a mixture of bubbles of various lifetimes. Furthermore, the performed simulations neglect the liquid flow and the variation of residence time for each bubble diameter in the flow field. Additionally, coalescence effects generally need to be considered for the investigation of rising bubble swarms. In summary, all these differences between reality, measurement and simulation are points that lead to differences in the BSD.

3.3. Optimization of the CO_2 Gassing

The previously shown shrinking of microbubbles assisted by the Laplace pressure is enhancing the mass transfer. Microbubble gassing aims to utilize this highly efficient way to dissolve gas in liquid, which means that the majority of the produced bubbles and their diameter is aimed to be below 100 µm. For CO_2 gassing of aqueous TEA solutions, several factors can improve the gassing. Already, the application of porous spargers with pores below 10 µm is proven to produce bubbles with smaller diameters as demonstrated Section 3.1. However, reducing the pore diameter below 1 µm pore size is found to affect the resulting bubble diameter to a lesser extent. In the following step, the effect of gassing rate and TEA concentration variation is investigated.

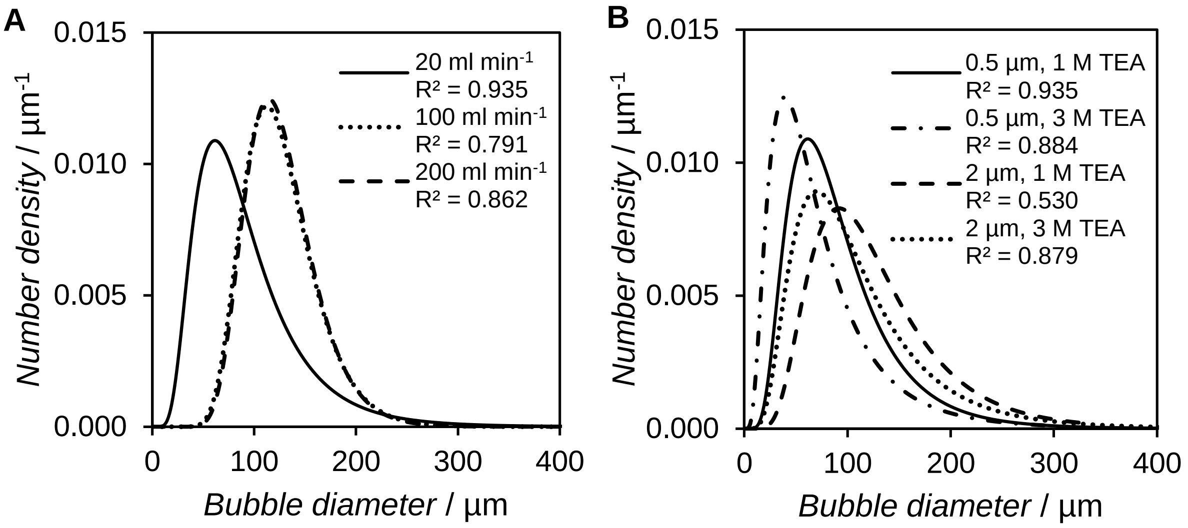

Figure 43: Bubble size distribution influenced by the variation of the CO_2 gassing rate (A) in 1 M aqueous triethanolamine (TEA), and the impact of different utilized porous spargers with mean pore sizes of 0.5 µm and 2 µm in aqueous TEA solution of different molarities at a CO_2 gassing rate of 20 ml/min (B).

The BSD for different CO_2 gassing rates in 1 M aqueous TEA are displayed in Figure 43 A. It can be seen that the BSD shifts to smaller sized bubbles when decreasing the gassing rate to 20 ml/min. In view of calculated d_{32}, the difference is only minor with values of 142, 146 and 146 µm for 20, 100 and 200 ml/min, respectively. However, the direct comparison of the measured BSD by the mean diameter d_{50} shows that a shift from 79 µm to 110 µm occurs for the $d_{50,\ 20\ ml/min}$ and $d_{50,\ 100\ ml/min}$, respectively. In contrast to that, increasing the gassing rate to 200 ml/min did not change the BSD. The effects are usually caused by using a porous sparger with an inhomogeneous pore size distribution. During the initial bubble formation, neighboring pores can cooperate through coalescence [64,136]. Lowering of the gassing rate reduces the coalescence on the sparger surface, whereas an increased gassing rate activates more pores enhancing joint bubble formation [64]. At the same time, activation of smaller pores can also lead to smaller bubbles forming [64]. However, these are only a small fractions in the BSD. Nevertheless, increasing the gassing rate usually broadens the BSD due to these effects. This includes that a gassing rate above a critical point leads to the effect that all pores are activated and a secondary bubble formation above the pores occurs [137]. Consequently, the bubble formation process gets independent of the gassing rate producing a constant BSD [137]. The occurrence of such a secondary bubble formation in the gassing of 1 M aqueous TEA with 200 ml/min is likely to happen, which explains the observed unchanging BSD at higher gassing rates.

The gassing rate of 20 ml/min was selected for further investigations, because the smallest bubbles are produced at this rate. As shown in Figure 43, increasing the TEA concentration led to smaller bubbles being formed. For the 0.5 µm sparger, the d_{50} of 79 µm decreased to 58 µm, while µm for the 2 µm sparger, the d_{50} shifted from 109 µm to 98 µm. Varying the TEA concentration, the physical properties of the medium are changing, and this is explaining the changing BSD. Overall, the bubble formation at a single hole and multiporous sparger are affected by surface tension and viscosity. In case of TEA, the surface tension and viscosity are the major properties, which are getting affected. Increasing the TEA concentration from 1 M to 3 M reduces the surface tension from 63.1 mN/m to 53.4 mN/m, respectively [138]. In turn, the decreased surface tension causes faster bubble detachment even at smaller bubble diameters [64]. This leads to smaller bubbles being formed, which simultaneously increases the bubble density. In regard to the dynamic viscosity, it essentially triples from 1.56 mPa*s at 1 M TEA to 4.47 mPa*s at 3 M TEA [138]. An increase in viscosity causes higher drag forces acting on the bubble formation, which slows the bubble growth [139]. Similar to increasing the gassing rate, smaller pores are activated due to the elevated pressure under the porous surface [64]. However, viscosity is also known to have the opposite effect on the bubble size. Higher viscosities can also cause an increase in bubble size due to coalescence enhancement [140]. In sum, the beneficial effects to produce smaller bubbles are dominating as seen from the smaller bubbles being generated in the experimental set-up. Further reduction of bubble size can be theoretically achieved by addition of additives, introduction of shear forces and other means. However, complications can occur in the downstream processing when using additives, often making it necessary to introduce further separation steps for additive removal, which is increasing the costs [141]. This is in general limiting the applicability of additives for these kind of processes. Regarding application of shear forces, it was shown in stirred tank reactors that the introduction of shear forces has minor to no influence on bubble size reduction [131]. In these studies, it was found that microbubbles are smaller than the eddies produced by stirring, preventing further size reduction [131].

In short summary, microbubbles can easily be produced in aqueous TEA due its inherent fluid properties reducing the diameter of produced bubbles. In general, producing smaller bubbles is beneficial for achieving a higher interfacial surface area for mass transfer. At the same time, the buoyancy force for these microbubbles further decreases, which effectively increases the bubbles residence time in the liquid phase. The complete dissolution of CO_2 bubbles in aqueous TEA gives the opportunity to reduce the applied gas inlet stream as well as minimizing the CO_2 emission in the off-gas [125].

3.4. Mass Transfer Investigation

Microbubble gassing is already shown to be easily achieved in aqueous TEA with the majority of bubbles having diameters below 100 µm at various conditions. Besides the BSD, measuring the mass transfer is important to characterize efficient gassing in multiphase reactors. In this way, mass transfer limitation can be assessed and prevented by choosing appropriate reaction parameters. This prevents kinetic limitations, which would otherwise occur in the case of an insufficient supply of dissolved gaseous reactants. Apart from that, minimizing the amount of unreacted gaseous reactants is of high interest. Therefore, the mass transfer is investigated in the aqueous TEA system. For this study, different gassing rates are applied through the previously tested 0.5 µm, 2 µm and 10 µm sparger. In general, the mass transfer rate $\dot{N}$ can be calculated by Eq. 18 for gaseous species like CO_2 and O_2, which are transferred from the bubble into the liquid. The mass transfer rate is directly proportional to the mass transfer coefficient k_L, the specific interfacial area a and the concentration gradient. The concentration gradient depends on the saturation concentration c^* and the bulk concentration c of the gaseous component in the liquid medium. Similarly, k_L depends on different parameter and is considered a function of the fluid properties and operation conditions. Generally, it is difficult to determine the k_L and a individually due to being dependent on several parameter. Therefore, the volumetric mass transfer coefficient k_La is usually determined, which gives a measure for the efficiency of the mass transfer. Overall, this equation is valid for two-phase systems without any reaction present that consumes gaseous components.

$$\dot{N} = k_L \cdot a \, (c^* - c) \qquad \text{Eq. 18}$$

For the measurement of CO_2 in aqueous TEA, a CO_2 sensor spot from PreSens (Regensburg, Germany) was utilized. However, no measurable CO_2 signal was detected with this sensor, whereas measurements of CO_2 in pure water are possible. These sensors are validated to work in the range of 10 to 250 hPa p_{CO_2}. The positive control in water indicates that the adsorption and hydration of CO_2 mediated by TEA, prevents its detection. It is likely that the high affinity of aqueous TEA solutions to CO_2 is preventing the quantitative diffusion through the sensor membrane to interact with a luminescence dye. In turn, this likely causes low CO_2 signals, which are below detection limit. In general, CO_2 measurements in aqueous amine solutions are more complex as in addition to the hydrated CO_2 equilibria [87], the CO_2 equilibrium with the amine [48] needs to be considered. This complexity is circumvented by utilization of a different established approach [142], which uses air oxygen k_La and comparison of the diffusion constants (D_L) for the estimation of the CO_2 k_La according to Eq. 19.

$$(k_L)_{CO_2} = (k_L)_{O_2} \cdot \left[\frac{(D_L)_{CO_2}}{(D_L)_{O_2}}\right]^{0.5} \qquad \text{Eq. 19}$$

In Eq. 19, the diffusion constants provide a correction factor to estimate the CO_2 k_La provided that the specific surface area between the air and CO_2 gassing is comparable [142,143]. The measured air oxygen k_La are shown in Figure 44.

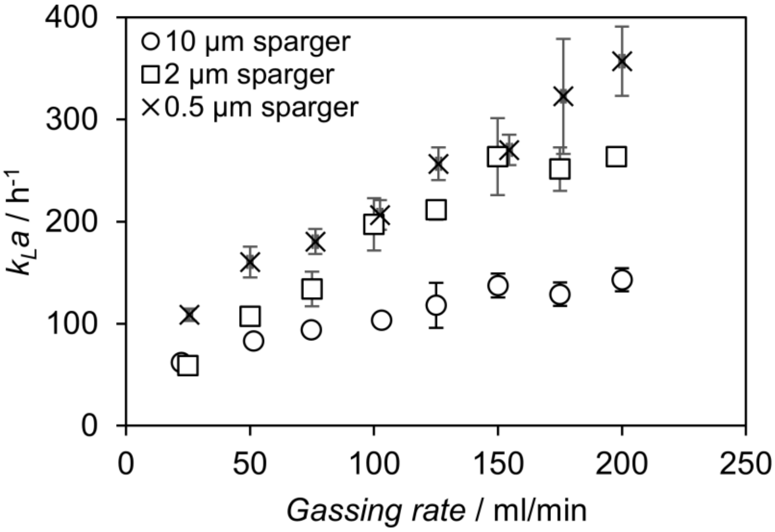

Figure 44: Experimentally determined dynamic air oxygen k_La using different porous sparger for the aeration of 150 ml 1 M aqueous triethanolamine at 30 °C in a bubble column with an inner diameter of 27.0 mm.

Application of higher gassing rates leads to increasing air oxygen k_La for all tested spargers. Both, the 0.5 µm and 2 µm sparger perform similarly, with the 0.5 µm sparger achieving overall slightly higher k_La values. These results are in agreement with the previously determined BSD in Figure 39. In the BSD, the 0.5 µm and 2 µm sparger produced similar mean Sauter diameter of 61.3 µm and 71.1 µm, respectively. In general, the BSD and the resulting d_{32} correlate to the specific surface area with smaller bubbles achieving higher values for a. The lower k_La values for the 10 µm sparger can be explained by formation of roughly three times bigger bubbles (d_{32} = 184.3 µm) due to the larger sparger pore diameter [64], which lowers the part of the specific surface area that is part of the k_La. Reaching microbubbles smaller than 40 µm, even the mass transfer coefficient k_L increases as indicated by results from a recent study [125]. These results again emphasize the importance of microbubble gassing.

In the next step, the specific surface area needs to be assumed or proven to be comparable between air and CO_2 gassing to use the established correlation (Eq. 19) to estimate the CO_2 k_La based on the air oxygen k_La [142,144]. Often, it is assumed that the specific surface area is comparable for macrobubble gassing of air and CO_2. [142,143] However, microbubble formation is achieved in the gassing of aqueous TEA, where the accelerated dissolution assisted by the Laplace pressure occurs. Therefore, the comparability of air and CO_2 microbubble gassing is examined in more detail by means of the resulting BSD at saturation. This minimizes the mass transfer being affected by the gas composition, which generally influences the interfacial tension in the system [145]. Furthermore, determining the BSD at saturation, mass transfer effects can be largely prevented, which would otherwise occur due to the different solubility concentrations of both gases. However, the only mass transfer is expected to occur due to the increased Laplace pressure.

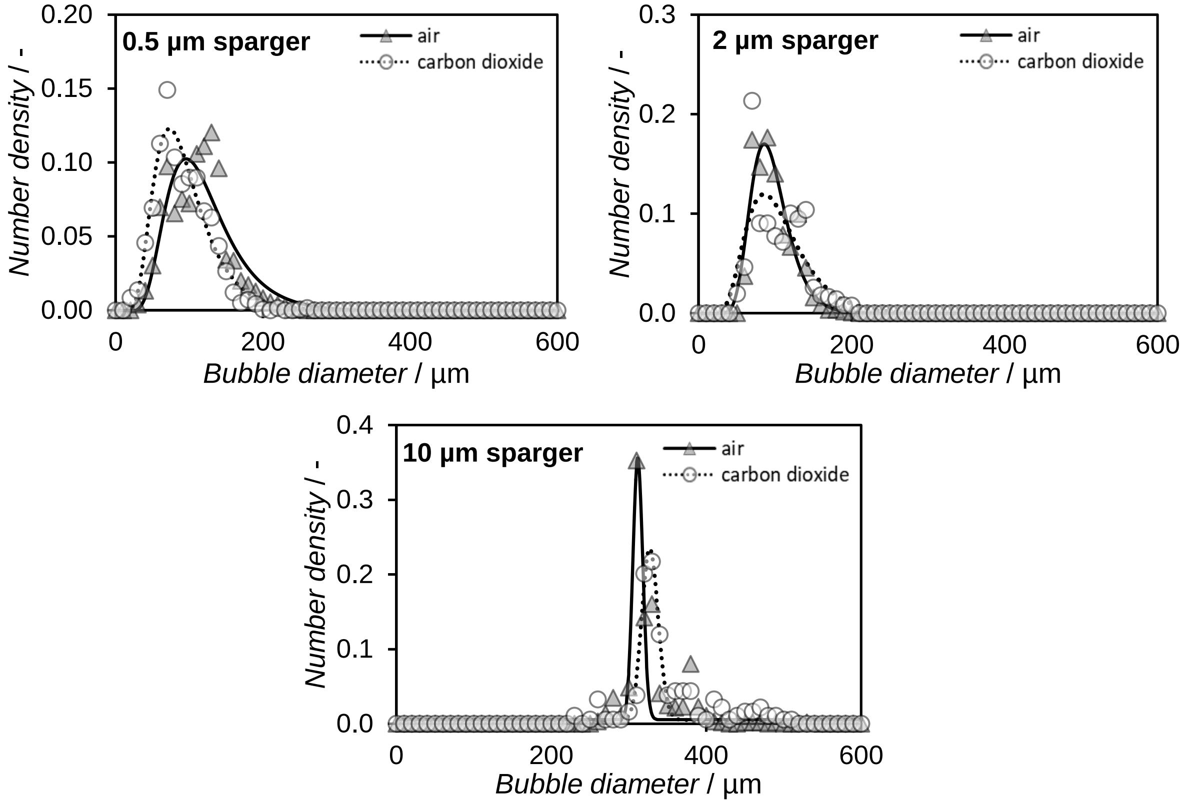

Figure 45: Determined bubble size distributions for the gassing of 150 ml of 1 M triethanolamine with 20 ml/min air and CO_2 with different spargers in a bubble column with an inner diameter of 31.9 mm at saturation under ambient conditions. The bubbles were detected with a Sopat-VI Sc probe-based microscope and analyzed by the integrated image analysis software. Log-normal regressions with the following R^2 for air and CO_2 were calculated, respectively: 0.5 µm sparger: 0.88 and 0.96; 2 µm sparger: 0.93 and 0.76; 10 µm sparger: 0.80 and 0.91.

The obtained BSD, shown in Figure 45, are once more in agreement with the dynamic determined k_La as only the 10 µm sparger produces much bigger bubbles compared to the other spargers. This reduces the specific surface area and therefore, results in low k_La values. Additionally, the application of the 0.5 µm and 2 µm sparger produces similar BSD, being consistent with the trend in $k_L a$ values (Figure 44) and the BSD at saturation with a higher gassing rate of 100 ml/min (Figure 45) compared to 20 ml/min (Figure 39).

Furthermore, the BSD for air and CO_2 look similar as can be seen in Figure 45. This similarity is confirmed by performing a double sided t-test. In the t-test, the measured cumulative distributions of air and CO_2 utilizing the three different spargers are merged at a resolution of 10 µm, respectively. Covering the bubble diameter range of 10-800 µm, where all bubbles are detected, creates a data set of 80 points for each air and CO_2 gassing. For this comparison, a highly significant p-value of 0.964 is calculated for the null hypothesis, which assumes no difference in the BSD between both gases. Due to the specific surface area being reflected by the BSD, it can be safely confirmed that air and CO_2 gassing at saturation is similar. Therefore, the estimation of the CO_2 $k_L a$ based on the air $k_L a$ can be performed. For this, the diffusion constants of air oxygen and CO_2 are necessary, which are $2.10 \cdot 10^{-5}$ cm²/s and $1.92 \cdot 10^{-5}$ cm²/s at 25 °C in water, respectively [146]. Based on these comparable diffusion constants, the calculated $(k_L)_{CO_2}$ is only 4.4% smaller than the $(k_L)_{O_2}$. This means that the main difference between both mass transfers are a result of the different solubilities, which directly affects the concentration gradient. To emphasize, air oxygen has a much lower solubility with a Henry constant of 1.3 M/atm, whereas CO_2 has a Henry constant of 34 M/atm in water at 25 °C [147]. In aqueous TEA solution, this difference is even bigger as CO_2 has a much higher solubility due to the adsorption resulting from the amine. Therefore, a several fold higher mass transfer rate is expected for CO_2.

In summary, the microbubble sparger (0.5 µm and 2 µm sparger) achieve much higher mass transfer rates, which is consistent with smaller bubble diameter being detected in the aqueous TEA solution. This increases the specific surface area as well as enhancing the mass transfer constant due to reaching microbubbles below 40 µm. As a result, higher $k_L a$ values are achieved. Furthermore, it is shown that the bubble diameter is affected by the saturation level of the liquid phase, which enhances the mass transfer rates in CO_2 depleted aqueous TEA. In consequence, the initial mass transfer efficiency is expected to be high, which in result decreases with the CO_2 saturation level.

3.5. Gassing Efficiency in Aqueous Triethanolamine

In an optimal process, the necessary CO_2 gassing rate to reach saturation in the aqueous amine solution should be fast and highly efficient. Further enhancement of the mass transfer rate by applying a flow above 200 ml/min is not feasible in the bubble column set-up as excessive foaming occurs. In addition, the fraction of CO_2 molecules transferring from the gas into the liquid phase in proportion to the amount remaining in the gas phase and eventually in the exhaust decreases. Therefore, the mass transfer efficiency is an important characteristic to evaluate the extent of wasted gas. For the determination of the standard gas transfer efficiency (*SGTE*), the supplied gassing rate of the gas component $\dot{w}_G$, such as oxygen or CO_2, and the standard gas transfer rate (SGTR) are required. The *SGTR* is calculated according to Eq. 20, which utilizes the determined $k_L a$, gas solubility c^* and liquid volume V_l for a given process condition. In the next step, the *SGTE* is calculated according to Eq. 21, which gives the percentage of applied gas molecules that dissolve in a given liquid volume.

$$SGTR = k_L a * c^* * V_l \qquad \text{Eq. 20}$$

$$SGTE = \frac{SGTR}{\dot{w}_G} * 100\% \qquad \text{Eq. 21}$$

Utilizing the determined air oxygen $k_L a$, the standard oxygen transfer efficiency (*SOTE*) is calculated for the 0.5 µm and 10 µm sparger. As seen in Figure 46, the highest *SOTE* is obtained at the lowest gassing rates for both spargers. The 0.5 µm sparger reaches the highest efficiency at the lowest investigated gassing rate of 25 ml/min, where around 20% of the injected oxygen dissolves in the medium. In comparison, the 10 µm sparger only reaches an efficiency of 13% and performs at approximately halve of the efficiency of the 0.5 µm sparger. In this experiment, the influence of the changing saturation level on the efficiency is taken into account due to the nature of the dynamic $k_L a$ measurements. At high gassing rates, the SOTE gets nearly independent as seen in Figure 46, which is expected to occur due to a secondary bubble formation above the pores as previously emphasized [137].

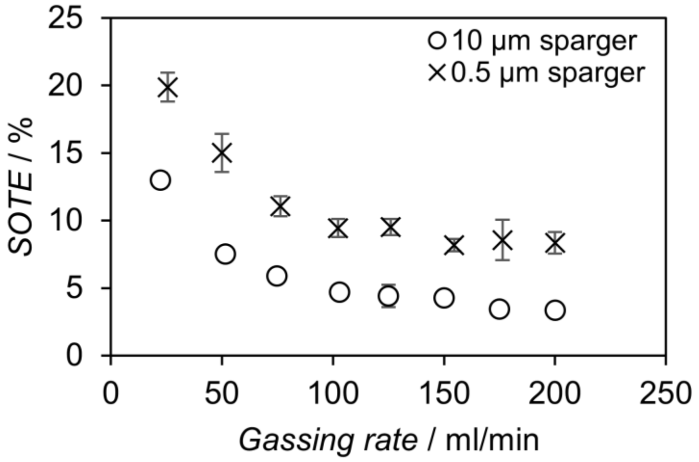

Figure 46: Comparison of standard oxygen transfer efficiencies (SOTE) for different gassing rates applied with porous spargers having a mean pore size of 0.5 µm and 10 µm, respectively. Values were calculated from the k_La measurements shown in Figure 44.

For an estimation of the standard CO_2 mass transfer efficiency (*SCTE*), the *SOTE* can be used in the same way utilizing the air oxygen k_La for assessment of the CO_2 k_La. Additionally, the higher CO_2 saturation concentration compared to air oxygen has to be accounted for. The use of amines for high CO_2 loadings further enhances the initial gassing. The calculated values of the *SCTE* reaches values above 100% due to the high CO_2 solubility, which emphasizes that CO_2 bubbles are predicted to completely dissolve during the initial gassing of CO_2 in aqueous TEA. Reaching higher CO_2 saturation levels, the mass transfer efficiency decreases due to the decreasing concentration gradient, increasing bubble diameter and decreasing k_La. Here, incorporation of the enzymatic carboxylation of resorcinol has the potential to increase the mass transfer due to the continuous consumption of dissolved CO_2. This maintains the concentration gradient reducing the otherwise occurring loss of efficiency. The mass transfer efficiency can be further improved by process optimization, which includes, among other things, increasing the bubble column height to utilize the higher hydrostatic pressure. This enhances the CO_2 saturation concentration resulting in a higher mass transfer gradient. Furthermore, this scale-up increases the residence time of bubbles.

Generally, increasing the residence time is beneficial for mass transfer processes as it prolongs the contact time between gas and liquid phase. However, excessively long residence times without sufficient bubble coalescence at the liquid surface causes accumulation of foam. In context of the CO_2 gassing to saturate the aqueous TEA, the amount of foam increases at higher gassing rates. In an optimal process, the CO_2 saturation of the aqueous amine solution should be fast and highly efficient. However, further enhancement of the mass transfer rate by applying a gassing rate above

200 ml/min is not feasible in the bubble column set-up due to severe foaming. The increased gassing rate causes higher gas hold-ups, which transition to foaming with the majority of gas bubbles being part of the foam and not residing in the actual liquid phase. For quantification of this effect, the fractional gas hold-up ε_G is calculated according to Eq. 22 [148] based on the liquid volume at rest V_L and the total volume V_{TOT} in the gas-liquid system. In Figure 47 A, the determined ε_G is shown for the different spargers of up to 200 ml/min. Furthermore, the foam hold-up ε_F is calculated (Eq. 23), which increases drastically at high gassing rates for the microbubble sparger as shown in Figure 47 B.

$$\varepsilon_G = \frac{V_{TOT} - V_L}{V_{TOT}} \qquad \text{Eq. 22}$$

$$\varepsilon_F = \frac{V_{Foam}}{V_{TOT}} \qquad \text{Eq. 23}$$

It is expected that these high gas hold-ups for microbubbles are reached due to their long residence time, which is caused by their slow rising velocity. Usually, a high gas hold-up is preferred in a multiphase reactor to ensure a high interfacial area for mass transfer. However, microbubbles are shown to produce the majority of the gas hold-up as stable foam at high gassing rates.

From characterization of the absorption-based post-combustion capture of CO_2, amine solutions are known to tend to produce foam, where the foaming tendency and foam stability is primarily affected by the liquid's viscosity, density and surface tension [149]. Furthermore, the foam formation and foam stability is influenced by several process parameter including the gassing rate, temperature, amine concentration and CO_2 loading [149,150]. In particular, increasing the gassing rate and CO_2 loading, when using aqueous monoethanolamine solutions, is generally reported to increase the foam volume [150]. Various amines beside monoethanolamine tend to foam similarly, whereas other amines, like diethanolamine are not foaming [149]. Furthermore, foam stability is known to be determined by bubble coalescence with larger bubbles tending to coalesce more, which reduces the foam stability [151]. This explains the higher foam volume when using the microbubble sparger in contrast to the 10 µm sparger. Generally, microbubbles are considered to have a lower coalescence tendency due to their charged surface [152,153], which consequently leads to the formation of highly stable foam [151,154].

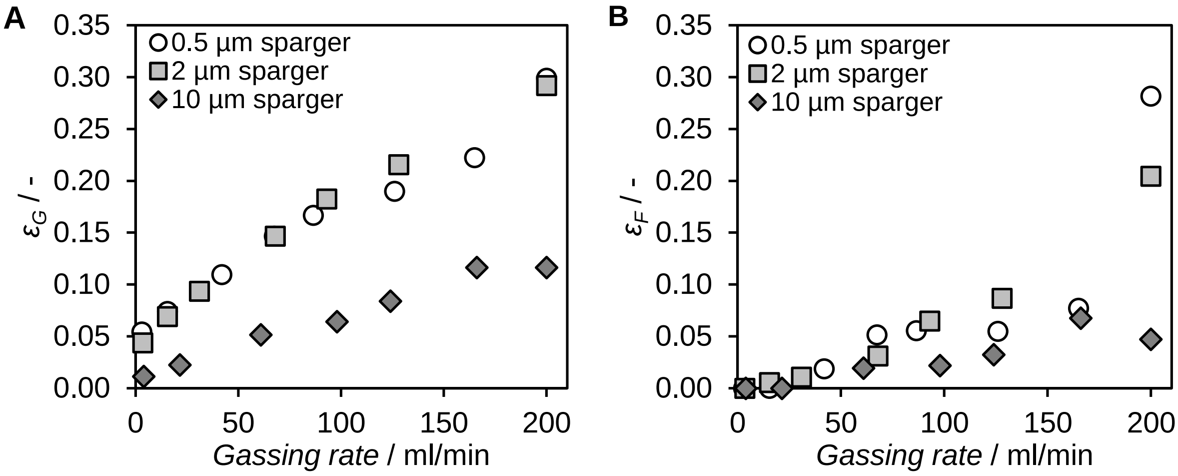

Figure 47: Gas hold-up ε_G (A) and foam hold-up ε_G (B) in 100 ml 1 M aqueous triethanolamine for up to 200 ml/min CO_2 gassing utilizing different sparger.

The tendency of microbubbles to produce stable foam needs to be considered for efficient microbubble gassing in a process. Otherwise, the advantage of using microbubbles to enhance the mass transfer is negated by the disadvantage of having to deal with excessive foaming. In the experiments, basically no foam is observed when applying a gassing rate below 50 ml/min CO_2, which equals a superficial gas velocity of 1.46 mm/s. In addition, higher mass transfer rates are always achieved with microbubble gassing in comparison to macrobubble gassing, which reduces the gassing rate to reach the same k_La. This is expected to compensate for the increased foaming tendency and foam stability.

3.6. Influence of an Active CO_2 Gassing on the Biotransformation

The initial CO_2 saturation of aqueous amines is critical to neutralize the alkaline pH, which prevents pH dependent enzyme deactivation as previously discussed. After the CO_2 loading and biocatalyst addition, dissolved CO_2 is consumed in the biotransformation. Here, a continuous CO_2 gassing is increasing the achievable yield and a higher reaction velocity by maintaining higher C1 substrate concentrations. However, the theoretical improvement is limited to the use of only low resorcinol concentrations to prevent enzyme deactivation as the enzyme shows a low tolerance to phenolic substrates [35]. Therefore, only concentrations of up to 100 mM are feasible at the moment. This limits reaction productivities severely according to the determined kinetic and thermodynamic parameter when using an active CO_2 gassing. Consequently, a highly efficient CO_2 gassing is mandatory.

Investigating the influence of the CO_2 gassing on the carboxylation of resorcinol in aqueous TEA, the 0.5 µm microbubble sparger and the 10 µm submillibubble sparger are compared. In a first comparison, both spargers are utilized at the identical CO_2 gassing rate of 100 ml/min showing identical initial productivities with minimal deviation between biological duplicates (Figure 48). However, application of the 10 µm sparger is shown to maintain a higher productivity after an extended reaction time as can be seen in Figure 48. It is expected that the different productivities during the course of the reaction are a result of enzyme deactivation. In general, enzymes are prone to deactivate at gas-liquid interfaces, which is demonstrated for different enzymes [155,156]. Previously, it was shown that the 0.5 µm sparger produces much smaller bubbles compared to the 10 µm sparger, which corresponds to a higher interfacial area. Therefore, the difference in the gas-liquid interfacial area is a result of the utilization of different spargers and is the most likely reason of enzyme deactivation. As consequence of the relatively low reaction rate in comparison to the mass transfer rate as well as the high CO2 solubility in aqueous TEA solutions, a possible mass transfer limitation is generally excluded. Furthermore, the pH measurement during the entire reaction confirms a constant C1 substrate concentration by maintaining a constant pH value. For the same reason of having a very slow reaction and constant pH, differences in the mixing behavior are expected to be neglectable. Already, the mixing is less efficient with bubbles in the micrometer range produced by utilization of both sparger as these bubbles have low terminal rising velocities and related impulse forces [132].

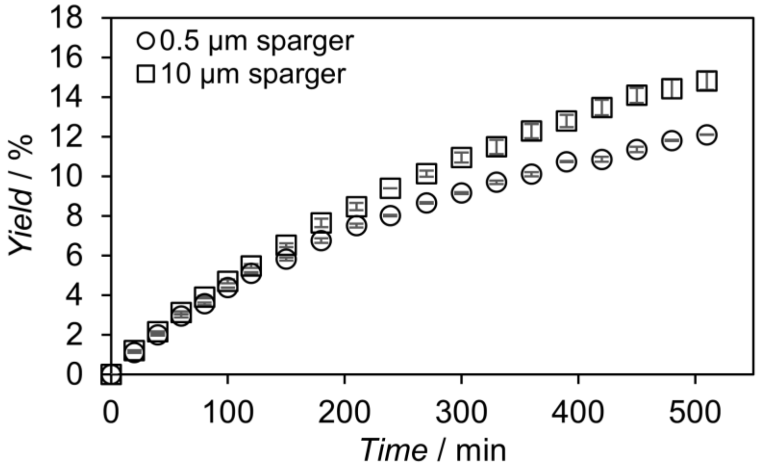

Figure 48: Carboxylation of 10 mM resorcinol by 12.5 µg/ml 2,6-DHBD (16.4 U/mg) at 30 °C in 1 M aqueous triethanolamine saturated with CO_2 prior to biocatalyst addition and continuous gassing with 100 ml/min CO_2 using different spargers.

Overall, the application of the 10 µm sparger results in over 20 % higher product yields after 5 hours. The difference is supposedly caused by microbubbles, which cause more stable foam to be produced due to their lower coalescence tendency. This effect leads to the accumulation of enzyme in the foam, known from processes that use foam for protein recovery [157]. Consequently, the flotation of enzymes causes a reduced activity in the liquid bulk phase. The yield difference ΔY between the 0.5 µm and 10 µm sparger is even more noticeable in the case of using a higher initial resorcinol concentration as shown in Figure 49. Application of higher substrate concentrations increases the reaction rate due to enzyme kinetics. Therefore, higher productivities are achieved overall. In turn, the improved turnover is likely to make the biocatalyst more sensitive to deactivating influences.

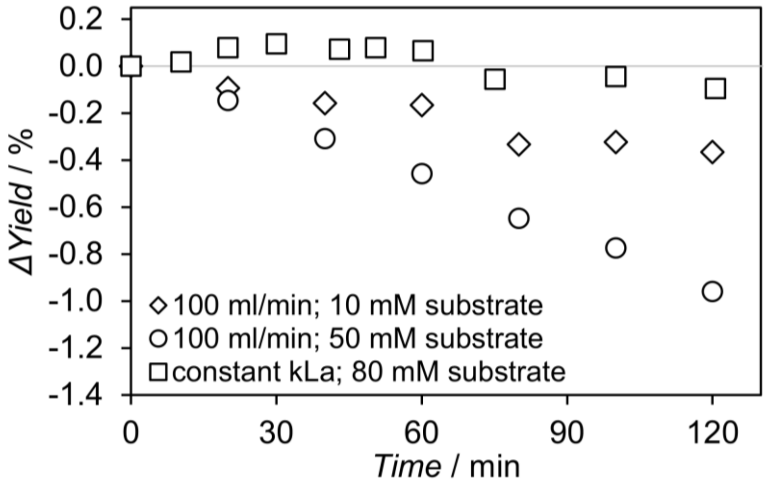

Figure 49: Yield comparison for the carboxylation of resorcinol by 12.5 µg/ml 2,6-DHBD (16.4 U/mg) in 1 M aqueous triethanolamine saturated with CO_2 prior to biocatalyst addition and continuously aerated with CO_2 using a microbubble (MB) and submillibubble (SB) sparger at 30 °C. ΔY is calculated by subtracting the achieved reaction yield for the MB gassing with the achieved yield, when using the SB sparger.

Performing the biotransformation at a comparable k_La of 140 1/h instead of using identical gassing rates, no yield difference is observed even at a higher substrate concentration of 80 mM. This highlights the enormous potential of microbubble gassing. The deviating productivities are likely caused by variation in the amount of gas-liquid interfacial area. Performing the carboxylation of resorcinol at identical k_La, the interfacial area is expected to be comparable. Assessing this theory, the Sauter mean diameter (d_{32}) determined from the measured BSD is used to calculate the rate of interfacial area generation ($\dot{a}$). First, the specific volume (SV) for spheres [158] is calculated according to Eq. 24. In the next step, $\dot{a}$ is determined using the specific volume and the gassing rate ($\dot{V}$) according to Eq. 25.

$$SV = \frac{6}{d_{32}} \qquad \text{Eq. 24}$$

$$\dot{a} = SV \cdot \dot{V} \qquad \text{Eq. 25}$$

In Table 8, the gassing parameter for the different conditions are summarized. At identical gassing rates, the microbubble sparger generates a 2.5 times higher interfacial area per minute compared to the 10 µm sparger. This is in agreement with the proposed enzyme deactivation by increased gas-liquid interfacial area leading to a reduced productivity. At comparable k_La, the generated interfacial area per minute varies by 30% and is therefore very similar between both spargers explaining the identical productivities. This difference is mainly artificially created due to approximating the d_{32} for the 50 ml/min gassing with the value obtained from the 20 ml/min gassing as no BSD was determined for the 50 ml/min CO_2 gassing. Furthermore, the lognormal distribution fittings of the BSD are used for the calculation of the d_{32}, which are in some cases not fitted perfectly with some R^2 values being below 0.8. Nevertheless, the calculated values are in good agreement with the experimental data from the biotransformation. The proposed deactivation caused by the interfacial area is under further investigation for verification. Additional factors and interdependencies, such as shear forces introduced by bubble bursting and coalescence, foam formation and processes at the interfacial area as well as the unique shrinking behavior of microbubbles [125] are expected to also affect enzyme deactivation.

Table 8: Comparison of the rate of the surface area generation $\dot{a}$ based on the measured Sauter mean diameter d_{32} in dependence to the applied gassing rate $\dot{V}$.

	Sparger	d_{32} (µm)	$\dot{V}$ (ml/min)	$\dot{a}$ (m^2/min)
Comparable gassing rate	0.5 µm	141	100	4.26
	10 µm	354	100	1.70
Comparable k_La	0.5 µm	112*	50	2.67
	10 µm	349	200	3.44

*Sauter mean diameter value is based on the measurement at 20 ml/min as the BSD was not measured at 50 ml/min

In contrast to the aqueous TEA system, where kinetic limitations due to insufficient mass transfer are hard to establish, microbubble aeration in other reaction systems demonstrates even more benefits in comparison to macrobubble aeration. For the enzymatic oxidation of glucose to gluconic acid by glucose oxidase, much higher productivities were achieved, when using microbubble spargers [131]. Furthermore, the higher mass transfer rates and efficiency achievable in the glucose oxidase system are consistent with the trends for the carboxylation of resorcinol in the aqueous TEA system.

4. Discussion and Outlook

Biotechnological processes increasingly replace chemical processes as biocatalysis utilizes several principles of green chemistry, which are beneficial to create more economic as well as environmental friendly processes. Especially, the possibility to perform complex reactions using enzymes with high regioselectivity is of major advantage. However, for implementation of a biocatalytic process step, knowledge of the catalytic system is necessary for designing reaction as well as enzyme engineering strategies. In this work, aspects of the reaction and process engineering are addressed giving insights into the TEA-mediated enzymatic carboxylation of resorcinol and promoting the applicability of this process for industry. However, two main challenges still remain to be solved to make this process economic and applicable for industry.

- Firstly, the enzyme has only a low tolerance for the phenolic substrate, which causes deactivation or denaturation. However, high substrate concentrations are preferred for reaching maximum reaction velocity according to the elucidated 2,6-DHBD kinetics. Furthermore, presence of high substrate concentration enables reaching a high product concentration, which is important to reduce manufacturing costs. Alternatively, fed-batch and continuous operation approaches can be utilized to minimize the present substrate concentration in a process, which reduces the expected substrate dependent denaturation. However, the maximum reaction velocity cannot be achieved at low substrate concentration. In contrast, protein engineering is a powerful tool to optimize enzymes making them better adapted to substrate and solvents [159]. This makes it possible to perform the reaction at high substrate concentrations and improve the productivity. In addition, activity, substrate specificity and stereoselectivity of enzymes can be modulated.
- Secondly, the major challenge of only reaching low product yields even at high C1 substrate concentration remains. Different *in situ* product product removal approaches are shown to significantly increase the reaction yield. The adsorption-based approach enables even yields above 80%. However, reaching yields above 80% still remains unfeasible due to competitive substrate adsorption on the adsorber. More efficient adsorption materials need to be found to improve the binding selectivity of product while reducing the competitive substrate adsorption at the same time. It is expected that the unspecific binding of the phenolic substrate can be reduced by replacing the styrene-divinylbenzene-based backbone structure of Dowex® with a more polar backbone like silica-based alternatives. Simulation of the interaction between

substrate, product and different adsorber materials by molecular modelling has the opportunity to provide new insights. At the same time, promising materials can be found, which can be subsequently confirmed for selective adsorbers in an experimental setup.

Nevertheless, performing enzymatic carboxylation in aqueous amine solutions is shown to enhance the biotransformation by providing high C1 substrate concentration. Furthermore, this reaction system utilizes gaseous CO_2 making it important for a green alternative to the Kolbe-Schmitt process. The absorption of CO_2 is shown to be easily achieved with porous spargers, which produce bubbles in the micrometer scale. These bubbles have a high surface to volume ratio. Therefore, they provide a high interfacial area between gas and liquid phase, which is enhancing the mass transfer. Reaching bubbles with diameters below 100 µm, the remarkably rapid bubble dissolution assisted by enhanced Laplace pressure is utilized, which is characteristic for microbubbles. This is shown to significantly improve the mass transfer rate as well as the gassing efficiency. Consequently, lower gassing rates can be applied saving energy costs and reducing the waste of unreacted CO_2 in the exhaust.

In principle, the enzymatic carboxylation can be implemented in post combustion CO_2 capture processes replacing the need for a stripper as illustrated in Figure 50. In the proposed set-up, the biocatalyst is immobilized on a carrier and performs the carboxylation in a packed-bed reactor. Application of immobilisates has the advantage that the biocatalyst can easily be retained in the reactor for enhanced biocatalyst utilization. Furthermore, the carrier structure and close proximity of enzymes creates a microenvironment, in which enzymes are potentially more stable. After the reaction, the product is removed from the aqueous amine solution by the adsorber present in a subsequent packed-bed. Here, several ISPR columns can be used in parallel to perform loading and elution of the product in intervals. This ensures a continuous process. During the carboxylation, the CO_2 loading of the aqueous amine solution decreases due to CO_2 consumption. Therefore, the lean aqueous amine solution can be pumped back into the CO_2 adsorber column. Depending on the extent of CO_2 depletion, an additional stripper may still be necessary.

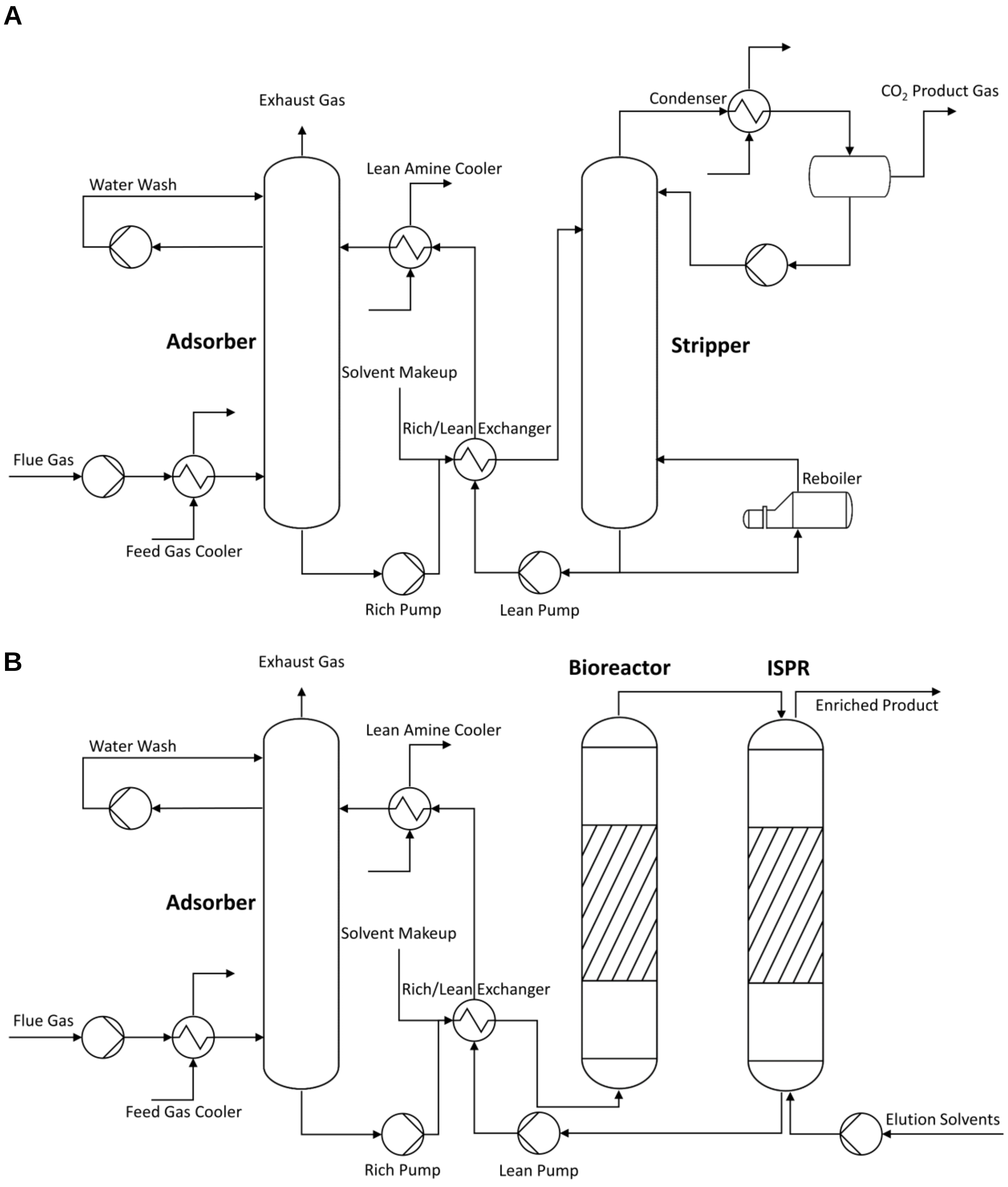

Figure 50: Conventional[69] (A) and modified (B) post-combustion CO_2 capture process for biocatalytic carboxylation.

Furthermore, the amine-mediated process can be expanded to perform a wide range of enzymatic carboxylation reactions. Various reversible decarboxylases were found and characterized in the last two decades extending the scope to produce valuable products utilizing CO_2. In Figure 51, a selection of known carboxylation reactions is presented. For one, phenolic acid decarboxylase (PAD) is known to regioselectively carboxylate *para*-hydroxystyrene derivates[94]. In this way, valuable products such as *para*-coumaric and ferulic acid can be produced with oxygen-stable enzymes and without need of cofactors.

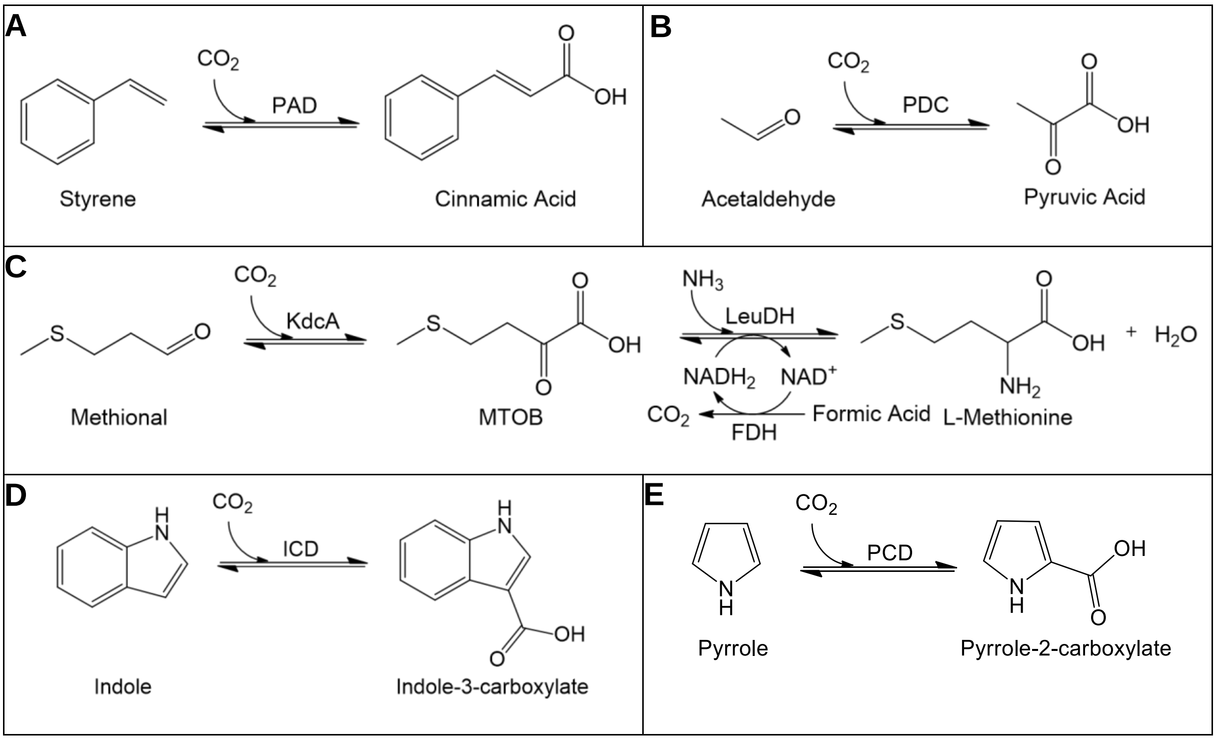

Figure 51: Biocatalytic Carboxylation reactions of A) phenolic acid decarboxylase (PAD), B) pyruvate decarboxylase (PDC), C) branched-chain alpha-keto acid decarboxylase (KdcA) combined with the reductive amination by leucine dehydrogenase (LeuDH) and a cofactor recycling using formate dehydrogenase (FDH), D) Indole-3-carboxylate decarboxylase (ICD) and E) Pyrrole-2-carboxylate decarboxylase (PCD).

In contrast, other decarboxylases require cofactors such as thiamine diphosphate like the pyruvate decarboxylases (PDC) and branched-chain alpha-keto acid decarboxylases (KdcA). Pyruvate decarboxylase can be used for the carboxylation of acetaldehyde using CO_2 to yield pyruvate [160]. This reaction can be even extended to include L-lactic dehydrogenase (LDH) in a one-pot reaction for the synthesis of L-lactic acid [161]. Even amino acids can be synthesized by utilizing decarboxylases like KdcA. This enzyme can fix CO_2 to produce 4-methylthio-2-oxobutanoate (MTOB) from methional, acting as intermediate for the reductive amination by leucine dehydrogenase (LeuDH) yielding the essential amino acid L-methionine [72]. Even indole and pyrrole derivates can be selectively carboxylated, which are employed in the synthesis of various pharmaceuticals and agrochemicals [162]. Pyrrole-2-carboxylate decarboxylase from *Bacillus megaterium* catalyzes the carboxylation of pyrrole in the presence of a carbon dioxide source, resulting in yields of up to 80% [163]. The carboxylation of indole derivates is reported to be efficient when utilizing indole-3-carboxylate decarboxylase from *Arthrobacter nicotianae* [164,165]. Often, these types of enzymes have a very narrow substrate scope, which makes it necessary to find more

CO_2 fixing enzymes with a wider substrate spectrum. Alternatively, protein engineering can be a powerful tool to tailor existing decarboxylases to accept additional substrates. Therefore, subsequent carbon capture and utilization biocatalysis research needs to further enhance reaction yields, optimize suitable biocatalysts and develop new as well as improve existing biocatalytic carboxylations.

5. Conclusion

In this detailed investigation, practical solutions are applied to overcome the strongly limited reaction yields in the enzymatic carboxylation of resorcinol by the 2,6-DHBA decarboxylase from *Rhizobium* sp.. As a result, a lab-scale production could be realized to obtain pure 2,6-DHBA (> 99.8%, HPLC).

- Correlation of the theoretical CO_2 loading enabled the determination of thermodynamic and kinetic parameters of the reaction. By this, the nature of the reaction mechanism utilized by the enzyme could be confirmed. It is revealed that the decarboxylase has a feature, close to a second activity, similar to a carbonic anhydrase. In the active center, bicarbonate gets protonated to H_2CO_3, which decomposes into water and CO_2. Aqueous CO_2 is subsequently consumed as the active C1 substrate. In this way, bicarbonate and aqueous CO_2 are utilized by the 2,6-DHBD for the carboxylation of resorcinol.
- Attempts to improve the thermodynamic equilibrium by application of TEA and high CO_2 pressure showed that the reaction yield can be improved at high pressure. However, the enhancement rapidly diminishes above 100 kPa CO_2 pressure due to a reduced effect on the C1 substrate concentration. Furthermore, an inhibiting effect is observed at higher pressure resulting from the high dissolved inorganic carbon concentration. It is expected that reversible carbamylation of the enzyme occurs, influencing the enzyme conformation, leading enzyme deactivation.
- Attempts to shift the thermodynamic equilibrium by *in situ* product removal were more successful, significantly improving the reaction yield. It was shown that the application of tetrabutylammonium bromide precipitates 2,6-DHBA. However, reaction yields could be improved only up to 60% at low TEA concentration, due to diminished precipitation at high TEA concentrations. In contrast, a more efficient anion exchanger, acting as adsorber, was found and characterized in detail. Utilization of this adsorber enabled reaction yields above 80%. Here, a competitive adsorption of the phenolic substrate was found, which is slowing the reaction and reducing the overall productivity.
- An easy downstream process to obtain 2,6-DHBA in a purity above 99.8% was established using the adsorber-based *in situ* product removal. In this process, solvents including TEA are recyclable for reuse. This was demonstrated in a first 3 l lab-scale process providing insights into the feasibly of the biocatalytic process to produce carboxylated phenols.

- The gassing of the reaction medium was investigated and optimized. Microbubble gassing reduced foaming, improved the mass transfer rate and efficiency of the absorption of CO_2 in the TEA-based reaction medium reducing the waste of unreacted CO_2 and related costs. The liquid properties of TEA enabled easy production of bubbles in the micrometer scale increasing the surface to volume ratio. An active CO_2 gassing during the biotransformation that causes a high rate of surface area generation was shown to negatively impact the productivity.
- Bubble size distribution measurements and mass transfer simulations confirm that CO_2 bubbles below 100 µm rapidly dissolve as the dissolution gets assisted by enhanced Laplace pressure. This process has three distinct phases. In the initial phase, CO_2 from the bubble dissolves into the liquid phase, while oxygen and nitrogen from the air saturated aqueous TEA solution diffuses into the bubble. After this initial, rapid mass transfer, microbubbles primarily contain air and remain more stable in aqueous TEA solutions. Next, these bubbles either reach the liquid surface or shrink further to reach diameters, where the enhanced dissolution assisted by the Laplace pressure gets more prominent and the bubbles get completely dissolved.

The successful and improved enzymatic synthesis as well as subsequent isolation of 2,6-DHBA with an efficient process that enables the recycling of the medium is demonstrated. The gained insights and improvements make the enzymatic carboxylation more competitive to the current state of the art chemical Kolbe-Schmitt process to produce carboxylated phenolic compounds.

6. Experimental Details

6.1. General

All chemicals were obtained with purities of ≥ 99 % from Sigma-Aldrich (Darmstadt, Germany), except triethanolamine, which was purchased from Carl Roth (Karlsruhe, Germany). Carbon dioxide 4.5 (≥ 99.995%) was obtained from Linde (Pullach, Germany). For the bubble column experiments, 1” long and ½” in diameter stainless steel filters with 2 µm and 10 µm pores were purchased from Techlab (Braunschweig, Germany). In addition, a 0.5 µm PerfectPeak® solvent inlet filter from Adaptas (Massachusetts, USA) was used as sparger. The pH measurements were performed with a Knick (Berlin, Germany) pH-Meter 766 Calimatic.

6.2. Overexpression of 2,6-Dihydroxybenzoic Acid Decarboxylase

E. coli BL21(DE3) cells containing the plasmid pET21a+ with the gene for 2,6-DHBD from *Rhizobium sp.* strain MTP-10005 were used for decarboxylase preparation. The cells were provided by Dr. Lorenzo Pesci (Hamburg University of Technology, Hamburg, Germany), who performed the transformation of the competent cells [35], while the original plasmid vector containing the decarboxylase gene was provided by Prof. Kurt Faber and Dr. Silvia Glueck (Graz University, Graz, Austria). For the pre-culture, cells from a single bead of a cryostock or a cell colony from Luria Bertani [166] agar plates supplemented with 100 µg/ml ampicillin were used. The cells were added to a 200 ml Erlenmeyer flask with baffles containing 50 ml Luria Bertani medium supplemented 100 µg/ml ampicillin. The pre-culture was incubated overnight at 37 °C and 120 rpm. The OD_{600} of the overnight culture was measured and used for the inoculation of 500 ml Luria Bertani medium supplemented 100 µg/ml ampicillin in 2 l Erlenmeyer flasks to a final OD_{600} of 0.1. The subsequent incubation was performed at 37 °C and 120 rpm. Reaching an OD_{600} between 0.6-0.8, the enzyme synthesis was induced by addition of 1 M IPTG to a final concentration of 1 mM. The overexpression was continued overnight at 20-25 °C and 120 rpm. The next day, the cells were harvested by centrifugation (8000 rpm (11325 rcf), 20 min and 4 °C) and washed with 50 mM KP_i pH 7.5. Wet cells were obtained after repetition of the centrifugation step and discard of the supernatant.

6.3. Preparation of Cell-Free Extract

For the preparation of cell-free extracts (CFE), wet cells suspended at 4 g/ml in 50 mM KP_i pH 7.0 were sonicated. The sonication was performed with a 3 mm tip at 70% power for three cycles using a BANDELIN Sonopuls from BANDELIN electronic (Berlin, Germany). Each cycle consisted of three minutes sonication and a subsequent incubation on ice to cool the sample down. After sonication, the sample was centrifuged at 20.000 rpm (48384 rcf) for 20 min at 4 °C. The supernatant was filtrated using a 0.45 µm filter. Afterwards, the CFE was stored at -20 °C or cooled at 4 °C for subsequent enzyme purification.

6.4. Enzyme Purification via Affinity Chromatography

Enzyme purification was performed by affinity chromatography in a packed bed column using 90 µm beads of Nickel Sepharose® 6 Fast Flow from Cytiva, USA. Different packed bed columns were used with varied column volumes (CV) depending on the amount of CFE to be purified. The smallest utilized CV was 3 ml. For equilibration, the column was washed with 5 CV of equilibration buffer having a pH of 7.4 and consisting of 20 mM Tris, 300 mM NaCl and 10 mM imidazole. Afterwards, the CFE was loaded on the column. Unbound protein was removed by application of 10 CV of washing buffer. The washing buffer had a pH of 7.4 and consisted of 20 mM Tris, 300 mM NaCl and 20 mM imidazole. Desired enzyme was eluted using 5 CV of elution buffer, which had a pH of 7.4 and consisted of 20 mM Tris, 300 mM NaCl and 250 mM imidazole. Buffer exchange to remove imidazole was performed by repeated centrifugation at 5000 rpm (3850 rcf) for 10 min at 4 °C using centrifuge tubes with an integrated 10 kDa cut-off membrane. For the buffer exchange, 50 mM KP_i pH 7.0 was used. Purified enzyme was aliquoted and stored at -20 °C.

6.5. Enzymatic Reactions

Reactions, if not otherwise stated, were carried out in closed 1.5 ml HPLC screw cap vials with purified 2,6-DHBD from one common batch at 30 °C and 500 rpm. Reaction mixtures without enzyme were presaturated with CO_2 by cannula acting as sparger until the pH was constant. The reactions were started by enzyme addition.

- For initial mass-specific enzyme activity measurements, samples were taken during the first four minutes when the yield was below 10% and zero order kinetics could be applied. Initial rates were fitted to the double substrate

Michalis-Menten model using Matlab R2018b from MathWorks (Natick, USA). In Matlab, the ODE45 solver was used to obtain mathematical solutions for the kinetic model including error estimations. Based on the random sequential model, a mass specific activity of 16.4 U/mg (v_{max}) was calculated for the purified 2,6-DHBD. This enzyme preparation was used for all experiments, if not otherwise stated.

- For determination of equilibrium yields, reaction yields were determined after 24 h and 48 h incubation with no change in analytical yield in between.
- For the *in situ* product precipitation experiments, 80 mM resorcinol and 350 mM tetrabutylammonium bromide were added after CO_2 saturation of aqueous TEA solutions.
- For experiments on the influence of an active CO_2 gassing on the productivity, reactions were carried out in a double jacket bubble column with an inner diameter of 27 mm and a working volume of 150 ml. The reactions were started by enzyme addition to the previously CO_2 saturated 1 M TEA solution containing the substrate resorcinol. Different porous sparger and gassing rates were applied.
- Pressure experiments were performed in open 1.5 ml HPLC screw cap vials that were placed in high-pressure reactors consisting of stainless steel cylinders capped with bronze lids [167]. These reactors have a volume of 160 ml and can be used at pressures up to 400 bar. For control experiments, aluminium reactors with identical volume were used. These were flushed with CO_2 prior to closing representing the condition for ~100 kPa CO_2 pressure.
- Carboxylation of resorcinol in medium containing Dowex® 1X8-50 were performed in closed 1.5 ml HPLC screw cap vials. For long-term experiments, the medium was flushed with CO_2 after each sampling to counteract CO_2 leakage.

6.6. Sampling Procedure and RP-HPLC Method

Reaction samples were diluted with equal volume of trifluoroacetic acid for samples containing TEA, while samples without TEA were diluted with a water/acetonitrile solution (20:80), supplemented with 3% (v/v) TFA. This was performed to stop the reaction and remove amine-bound CO_2. Samples were mixed and centrifuged for 5 min at 13.000 rpm (15700 rcf). Supernatant was injected in an Agilent (Waldbronn, Germany) LC-1100 HPLC system equipped with a diode array detector and a LichroCART 4 x 250 mm Lichrospher 100 RP column (5 µm). The separation was performed at 30 °C with the mobile phase consisting of eluent A, 0.1% (v/v) TFA in water, and eluent B, 0.1% (v/v) TFA in acetonitrile. The following gradient was applied at 0.8 ml/min: 0-1 min 10% B; 1-3 min 10-25% B; 3-10 min 25-60% B; 10-12 min 60-90% B; 12-16 min 90% B; 16-18 min 90-10% B; 18-20 min 10% B. Typical Retention times were 7.8 min for catechol, 8.7 min for 2,3-dihydroxybenzoic acid, 7.1 min for resorcinol and 8.4 min for 2,6-dihydroxybenzoic acid. The absorption was measured at 320 nm, 254 nm and 280 nm as shown in an example chromatogram (Figure 52) for a sample mixture of 1 mM resorcinol and 1 mM 2,6-DHBA. Depending on the compound concentration in the sample, a different detection wavelength was used for quantification. For example, resorcinol was quantified between 1-80 mM at 254 nm and below 1 mM at 280 mM due to a higher sensitivity. 2,6-DHBA was quantified between 1-80 mM at 280 nm, while either 320 nm or 254 nm was used for quantification below 1 mM. However, the best sensitivity and accuracy was at 320 nm for 2,6-DHBA.

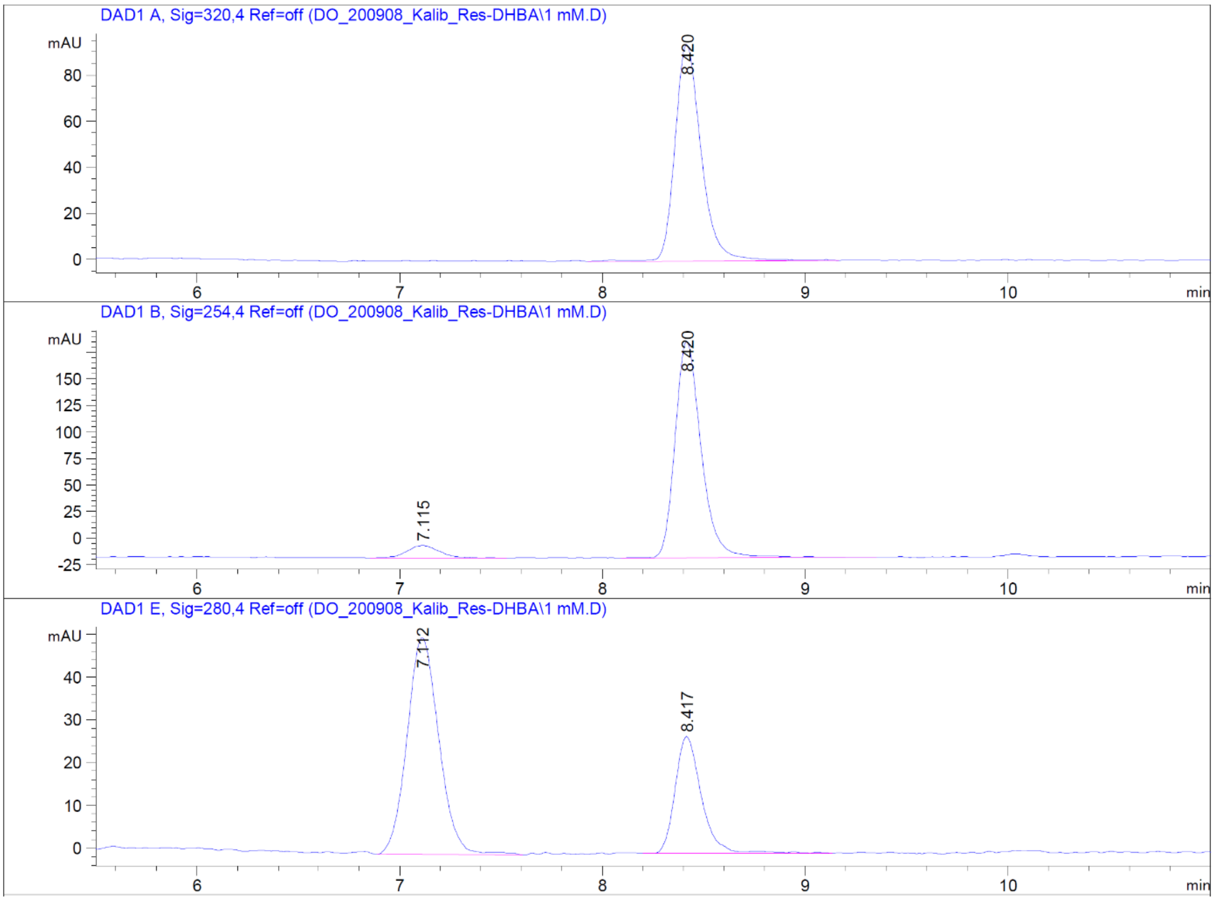

Figure 52: Example chromatogram of an aqueous mixture of 1 mM resorcinol and 1 mM 2,6-DHBA diluted with an equal volume of a water/acetonitrile solution (20:80), supplemented with 3% (v/v) TFA. The RP-HPLC method was utilized that is described in Section 6.6.

6.7. Dynamic $k_L a$ Measurements

Dynamic $k_L a$ measurements were performed in a double jacket bubble column with nitrogen and air gassing method [168]. The 360 mm long double jacket column had an inner diameter of 27 mm. For oxygen detection, PreSens (Regensburg, Germany) oxygen sensor SP-PSt3-NAU-D10-YOP was used. Measurements were performed in 150 ml 1 M TEA at 30 °C reaching a fill level of 225 mm. For the linearization of the data, Eq. 1 was used with the oxygen concentration at saturation c^* (mg/ml) and measured oxygen concentrations in the liquid c_l (mg/ml) at the different time points t (s).

$$k_L a = \frac{\ln\left(\frac{c^* - c_{l,2}}{c^* - c_{l,1}}\right)}{t_2 - t_1} \qquad \text{Eq. 26}$$

6.8. Bubble Size Distribution Determination

Inline measurements of bubble sizes were performed with a Sopat-VI Sc (Berlin, Germany) probe-based microscope and its integrated image analysis software (Sopat Software v2.1.17.1623) in a bubble column set-up. The column had an inner diameter of 31.9 mm and was used with a working volume of 150 ml. The probe was centered 36 mm above the sparger. The gap on top of the Sopat probe was adjusted to 2 mm for the 0.5 µm sparger and between 5-10 mm for the 2 µm and 10 µm sparger with smaller gaps at larger TEA concentrations. In the example Sopat image analysis, shown in Figure 53, the left side shows the raw image, while the detected bubbles are highlighted in the right image. Many bubbles are correctly detected, while other bubbles are not detected, which can have several reasons. Generally, bubbles are only detected if they are sufficiently in focus, don’t overlap with other bubbles and are not sticking to the surface of the Sopat probe. Comparing Figure 53 A and Figure 53 B, it can be seen that bubbles that remain stationary are not detected by the image analysis software. Through comparison of the field of view of the Sopat probe, the bubble diameter is calculated in the software. The field of view of the Sopat Sc is 2.7 mm and the measuring range is 9-1200 µm.

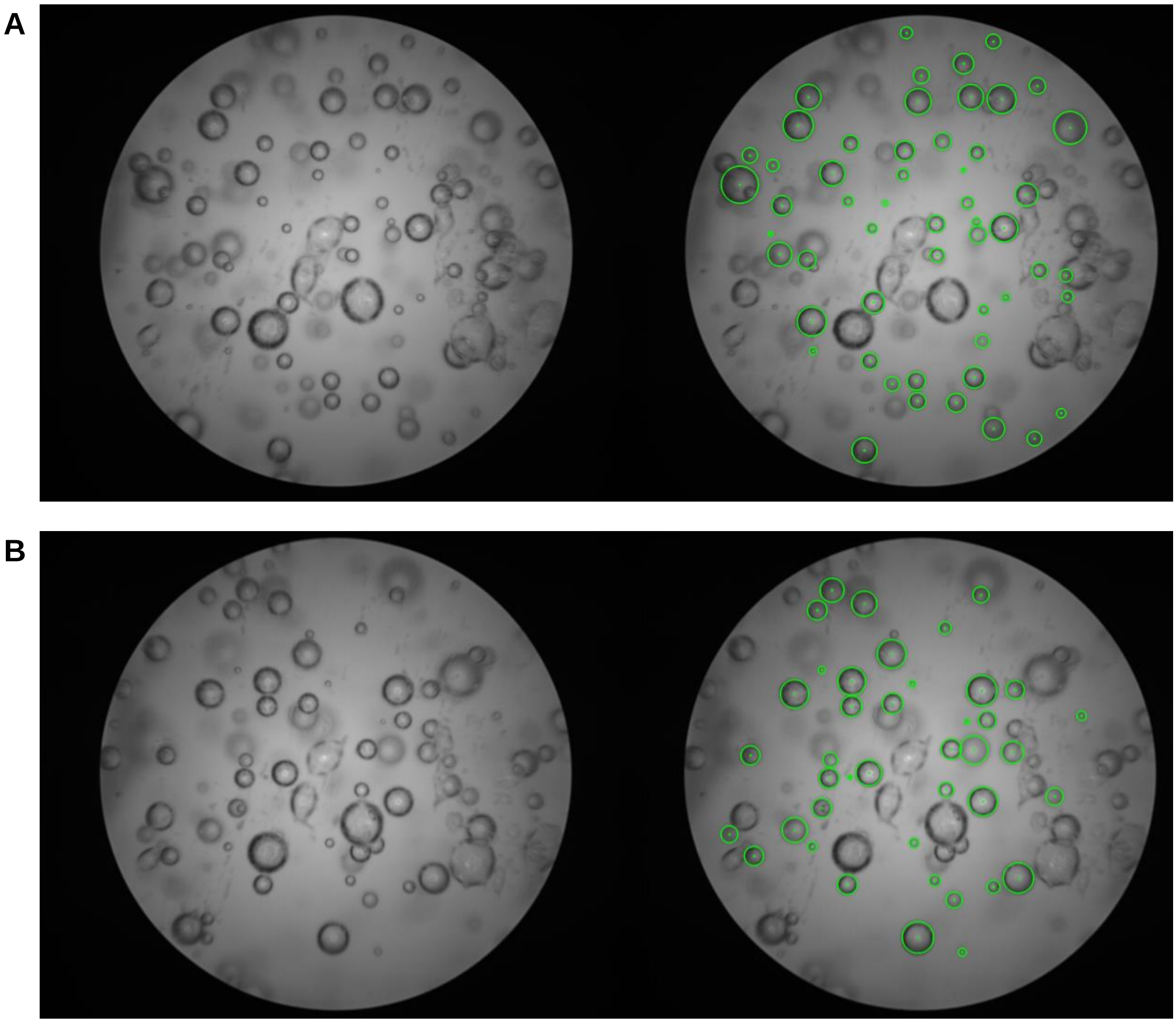

Figure 53: Example of a Sopat image analysis of two sequential taken images. The image A is directly taken before image B with a time difference of 200 ms. The left side shows the raw image, while the detected bubbles are highlighted in the right image.

For the bubble size distribution (BSD) measurement in unsaturated aqueous TEA (during CO_2 loading at a CO_2 gassing rate of 100 ml/min), the elapsed time between start of the CO_2 gassing and initialization of the Sopat measurement was ensured to be below 30 seconds. Nevertheless, the initially unsaturated aqueous TEA solution is further loaded with CO_2 during the Sopat measurement itself making it only possible to get an approximation of the BSD in unsaturated aqueous TEA. For each BSD, 200 images at a rate of 5 images per seconds were recorded, totaling a measuring time of 40 seconds. The obtained images were analyzed by the integrated image analysis software. Lognormal regressions were performed with the data analysis and graphing software Origin 2019b from OriginLab (Massachusetts, USA).

6.9. Adsorption Isotherms

For the characterization of the adsorption characteristics of Dowex® 1X8-50, different adsorption isotherms were applied to mixtures of resorcinol and 2,6-DHBA in 1 M aqueous TEA saturated with CO_2. The adsorbent mass concentration as well as molar ratio of resorcinol and 2,6-DHBA in 80 mM mixtures were varied. Adsorption isotherms are applied to fit the experimental data. Usually, thermodynamic models such as the ideal adsorbed solution theory is used to predict multicomponent adsorption. This method uses only single-solute isotherm parameters, but is not applicable to multisolute systems of unknown composition [169]. In these cases, empirical adsorption isotherms are applied. In the aqueous TEA solution, at least two adsorbates, resorcinol and 2,6-DHBA are present. Possible adsorption of dissolved inorganic carbon species, such as bicarbonate represent additional adsorbates. However, interference of these species was mostly neglected due to ensuring constant condition by not varying the TEA concentration. Therefore, different empirical adsorption isotherms for binary mixtures as well as the single solute Langmuir isotherm as control were applied (Eq. 32 - Eq. 36).

The single solute Langmuir isotherm represents the first and one of the simplest adsorption models to describe the complete adsorption on a surface [170]. In Eq. 27, the q_i gives the amount adsorbed on the surface, while $q_{m,i}$ represents the maximum capacity of the adsorbant. b_i gives the equilibrium constant and c_i the adsorbate concentration at equilibrium. For the binary mixture of resorcinol and 2,6-DHBA, the single solute Langmuir isotherm was applied for each adsorbate.

$$q_i = \frac{q_{m,i}\, b_i\, c_i}{1+b_i\, c_i} \qquad \text{Eq. 27}$$

Various empirical extended adsorption isotherms were created to describe multicomponent systems. These have, similar to the single solute Langmuir isotherm adsorption constants, constants for the capacity of different adsorption sites, which can differ for each component depending on the isotherm, and additional isotherm parameter. Butler and Ockrent (1930) created an extended Langmuir isotherm (Eq. 28) for multicomponent systems [171].

$$q_i = \frac{q_{m,i}\, b_i\, c_i}{1+\sum_{j=1}^{N} b_j\, c_j} \qquad \text{Eq. 28}$$

Similarly, Jain and Snoeyink (1973) described an extended Langmuir isotherm (Eq. 29 and Eq. 30), but only for binary mixtures with the assumption that a fraction of the adsorption sites, which are available for component 1 can also be occupied by component 2 [172].

$$q_1 = \frac{(q_{m,1} - q_{m,2})\, b_1\, c_1}{1 + b_1\, c_1} + \frac{q_{m,2}\, b_1\, c_1}{1 + b_1\, c_1 + b_2\, c_2} \qquad \text{Eq. 29}$$

$$q_2 = \frac{q_{m,2}\, b_2\, c_2}{1 + b_1\, c_1 + b_2\, c_2} \qquad \text{Eq. 30}$$

Similarly, several extended Freundlich isotherms exist. The extended Freundlich isotherm from DiGiano *et al.* (1978) is based on the assumption that all components have the same value of Freundlich exponent *n* and only differ in their Freundlich coefficients *K* (Eq. 31) [173].

$$q_i = \frac{K_i^{1/n}\, c_i}{\left(\sum_{j=1}^{N} K_j^{1/n}\, c_j\right)^{1-n}} \qquad \text{Eq. 31}$$

In contrast, the extended Freundlich isotherm from Sheindorf *et al.* (1981) only applies for a bisolute adsorbate system (Eq. 32 and Eq. 33) [174].

$$q_1 = \frac{K_1\, c_1}{\left(c_1 + K_{1,2}\, c_2\right)^{1-n_1}} \qquad \text{Eq. 32}$$

$$q_2 = \frac{K_2\, c_2}{\left(c_2 + K_{1,2}^{-1}\, c_1\right)^{1-n_2}} \qquad \text{Eq. 33}$$

In addition, the extended Tóth isotherm from Jaroniec and Tóth (1976) is applied to the experimental data (Eq. 34 and Eq. 35) [175].

$$q_i = \frac{q_m\, c_i}{\left[b_i + \left(c_i + b_{i,j}\, c_j\right)^n\right]^{1/n}} \qquad \text{Eq. 34}$$

$$b_{i,j} = \frac{b_i}{b_j} \qquad \text{Eq. 35}$$

The Fritz and Schlünder isotherm is one of the most versatile isotherms due to the wide range of isotherm parameters it covers. This isotherm was extended for multicomponent systems in 1974 by Fritz and Schlünder (Eq. 36) [176].

$$q_i = \frac{b_{1,i}\, c_i^{n_i}}{d_i + \sum_{j=1}^{N} b_{2,i,j}\, c_j^{m_{i,j}}} \qquad \text{Eq. 36}$$

Data fitting was performed in Origin 2021 from OriginLab (Massachusetts, USA) using the non-linear fitting tool.

7. Bibliography

1 J. Speight, *Lange's Handbook of Chemistry, Seventeenth Edition*, McGraw-Hill Education, New York, N.Y., 17th edn., 2016.

2 J. A. Kellum, Determinants of blood pH in health and disease, *Crit. Care*, 2000, **4**, 6–14.

3 L. Hermansen and J. B. Osnes, Blood and muscle pH after maximal exercise in man, *J. Appl. Physiol.*, 1972, **32**, 304–308.

4 R. Chester and T. Jickells, *Marine geochemistry*, Wiley, Chicester, 3rd edn., 2012.

5 S. C. Doney, V. J. Fabry, R. A. Feely and J. A. Kleypas, Ocean acidification: the other CO_2 problem, *Ann. Rev. Mar. Sci.*, 2009, **1**, 169–192.

6 S. M. Jarvis and S. Samsatli, Technologies and infrastructures underpinning future CO_2 value chains: A comprehensive review and comparative analysis, *Renewable Sustainable Energy Rev.*, 2018, **85**, 46–68.

7 GlobalData, *Global Urea Capacity and Capital Expenditure Outlook, 2020-2030*, 2020, https://store.globaldata.com/report/gdch0063mar--global-urea-capacity-and-capital-expenditure-outlook-2020-2030/#product-1924876.

8 M. Pérez-Fortes, A. Bocin-Dumitriu and E. Tzimas, CO_2 Utilization Pathways: Techno-Economic Assessment and Market Opportunities, *Energy Procedia*, 2014, **63**, 7968–7975.

9 F. Dalena, A. Senatore, A. Marino, A. Gordano, M. Basile and A. Basile, Chapter 1 - Methanol Production and Applications: An Overview, in *Methanol*, ed. A. Basile and F. Dalena, Elsevier, Amsterdam, Oxford, Cambridge, MA, 2017, pp. 3–28.

10 GlobalData, *Global production capacity of methanol 2018-2030*, 2020.

11 M. Pérez-Fortes, J. C. Schöneberger, A. Boulamanti and E. Tzimas, Methanol synthesis using captured CO_2 as raw material: Techno-economic and environmental assessment, *Appl. Energy*, 2016, **161**, 718–732.

12 A. S. Lindsey and H. Jeskey, The Kolbe-Schmitt Reaction, *Chem. Rev.*, 1957, **57**, 583–620.

13 G. L. Zabot, Chapter 11 - Decaffeination using supercritical carbon dioxide, in *Green sustainable process for chemical and environmental engineering and science*, ed. A. M. Asiri, Inamuddin and A. M. Isloor, Elsevier, Amsterdam, Netherlands, 2020, pp. 255–278.

14 J. A. Daniels, R. Krishnamurthi and S. S. H. Rizvi, A Review of Effects of Carbon Dioxide on Microbial Growth and Food Quality, *J. Food Prot.*, 1985, **48**, 532–537.

15 Y. E. Kim, J. A. Lim, S. K. Jeong, Y. I. Yoon, S. T. Bae and S. C. Nam, Comparison of Carbon Dioxide Absorption in Aqueous MEA, DEA, TEA, and AMP Solutions, *Bull. Korean Chem. Soc.*, 2013, **34**, 783–787.

16 *Pieter Tans, NOAA/GML (www.esrl.noaa.gov/gmd/ccgg/trends/) and Dr. Ralph Keeling, Scripps Institution of Oceanography (scrippsco2.ucsd.edu/)*.

17 T. J. Erb, Carboxylases in natural and synthetic microbial pathways, *Appl. Environ. Microbiol.*, 2011, **77**, 8466–8477.

18 D. R. Lide, *CRC handbook of chemistry and physics. A ready-reference book of chemical and physical data*, CRC, Boca Raton, Fla., London, 88th edn., 2008.

19 T. J. Erb, I. A. Berg, V. Brecht, M. Müller, G. Fuchs and B. E. Alber, Synthesis of C5-dicarboxylic acids from C2-units involving crotonyl-CoA carboxylase/reductase: the ethylmalonyl-CoA pathway, *Proc. Natl. Acad. Sci. U.S.A.*, 2007, **104**, 10631–10636.

20 T. J. Erb, V. Brecht, G. Fuchs, M. Müller and B. E. Alber, Carboxylation mechanism and stereochemistry of crotonyl-CoA carboxylase/reductase, a carboxylating enoyl-thioester reductase, *PNAS*, 2009, **106**, 8871–8876.

21 M. Hügler, R. S. Krieger, M. Jahn and G. Fuchs, Characterization of acetyl-CoA/propionyl-CoA carboxylase in Metallosphaera sedula. Carboxylating enzyme in the 3-hydroxypropionate cycle for autotrophic carbon fixation, *Eur J Biochem*, 2003, **270**, 736–744.

22 R. B. Durairaj, *Resorcinol. Chemistry, technology and applications*, Springer, Berlin, Heidelberg, 2005.

23 D. K. Hale, A. R. Hawdon, J. I. Jones and D. I. Packham, 671. The carboxylation of resorcinol and the separation of β-and γ-resorcylic acid by ion-exchange chromatography, *J. Chem. Soc.*, 1952, **0**, 3503–3509.

24 E. R. Stove, *2,6-dihydroxybenzoic acid and derivatives thereof*, British Patent, 302761, 1963.

25 T. Nakamatsu, Y. Nishida and N. Kometani, *Method for producing 2,6-dihydroxybenzoic acid*, US Patent, 5304677, 1994.

26 F. Müller and A. P. Applebyki, Weed Control, 2. Individual Herbicides, in *Ullmann's encyclopedia of industrial chemistry*, Wiley, Chichester, 2010.

27 H. Ruschig, J. Konig and D. Duwel, *gamma-resorcylic acid anilides and process for preparing them*, US Patent, 3449420, 1969.

28 E. M. May and F. Andrew, *Disazo gamma-resorcylic acid dye compositions*, US Patent, 3236829, 1966.

29 P. C. R. Soares-Santos, H. I. S. Nogueira, F. A. Almeida Paz, R. A. Sá Ferreira, L. D. Carlos, J. Klinowski and T. Trindade, Lanthanide Complexes of 2,6-Dihydroxybenzoic Acid: Synthesis, Crystal Structures and Luminescent Properties of [nBu4N]2[Ln(2,6-dhb)5(H2O)2] (Ln = Sm and Tb), *Eur. J. Inorg. Chem.*, 2003, **2003**, 3609–3617.

30 Reports Express, *Global 2,6-Dihydroxybenzoic acid (CAS 303-07-1) Market Report 2020*, 2020, https://reportsexpress.com/26-dihydroxybenzoic-acid-cas-303-07-1-market-report/, (accessed 3 March 2021).

31 Reports Express, *Global Dihydroxybenzenes (Catechol,Resorcinol,Hydroquinone) Market Report 2021*, 2021, https://reportsexpress.com/dihydroxybenzenes-catecholresorcinolhydroquinone-market-report/, (accessed 3 March 2021).

32 Enzymatic Carboxylation and Decarboxylation, in *Biocatalysis in organic synthesis 2*, ed. K. Faber, S. K. Au and E. M. Carreira, Thieme, Stuttgart, 2015.

33 C. Wuensch, S. M. Glueck, J. Gross, D. Koszelewski, M. Schober and K. Faber, Regioselective enzymatic carboxylation of phenols and hydroxystyrene derivatives, *Org. Lett.*, 2012, **14**, 1974–1977.

34 R. A. Sheldon and J. M. Woodley, Role of Biocatalysis in Sustainable Chemistry, *Chem. Rev.*, 2018, **118**, 801–838.

35 L. Pesci, S. M. Glueck, P. Gurikov, I. Smirnova, K. Faber and A. Liese, Biocatalytic carboxylation of phenol derivatives: kinetics and thermodynamics of the biological Kolbe-Schmitt synthesis, *The FEBS journal*, 2015, **282**, 1334–1345.

36 C. Wuensch, J. Gross, G. Steinkellner, A. Lyskowski, K. Gruber, S. M. Glueck and K. Faber, Regioselective ortho-carboxylation of phenols catalyzed by benzoic acid decarboxylases: a biocatalytic equivalent to the Kolbe–Schmitt reaction, *RSC Adv.*, 2014, **4**, 9673.

37 K. Kirimura and Y. Ishii, Enzymatic Kolbe–Schmitt Reaction for the Syntheses of Value-Added Compounds, in *Future directions in biocatalysis*, ed. T. Matsuda, Elsevier, Amsterdam, Cambridge, MA, 2017, pp. 135–147.

38 R. A. Sheldon, Atom utilisation, E factors and the catalytic solution, *Comptes Rendus de l'Académie des Sciences - Series IIC - Chemistry*, 2000, **3**, 541–551.

39 P. T. Anastas and J. C. Warner, *Green chemistry. Theory and practice*, Oxford Univ. Press, Oxford, 1st edn., 2000.

40 J. H. Clark, T. J. Farmer, L. Herrero-Davila and J. Sherwood, Circular economy design considerations for research and process development in the chemical sciences, *Green Chem.*, 2016, **18**, 3914–3934.

41 G. H. Kim, T.-S. Jung, W. H. Hong, J.-N. Kim and J.-D. Kim, Antisolvent Precipitation of Potassium Bicarbonate from $KHCO_3$ + H_2O + Ethanol/2-Propanol Systems in the CO_2 Capture Process, *Ind. Eng. Chem. Res.*, 2015, **54**, 8287–8294.

42 M. Yoshida, N. Fukuhara and T. Oikawa, Thermophilic, reversible gamma-resorcylate decarboxylase from Rhizobium sp. strain MTP-10005: purification, molecular characterization, and expression, *J. Bacteriol.*, 2004, **186**, 6855–6863.

43 M. Sato, N. Sakurai, H. Suzuki, D. Shibata and K. Kino, Enzymatic carboxylation of hydroxystilbenes by the γ-resorcylic acid decarboxylase from Rhizobium radiobacter WU-0108 under reverse reaction conditions, *J. Mol. Catal., B Enzym.*, 2015, **122**, 348–352.

44 C. Wuensch, N. Schmidt, J. Gross, B. Grischek, S. M. Glueck and K. Faber, Pushing the equilibrium of regio-complementary carboxylation of phenols and hydroxystyrene derivatives, *J. Biotechnol.*, 2013, **168**, 264–270.

45 L. Pesci, P. Gurikov, A. Liese and S. Kara, Amine-Mediated Enzymatic Carboxylation of Phenols Using CO_2 as Substrate Increases Equilibrium Conversions and Reaction Rates, *Biotechnol. J.*, 2017, **12**. DOI: 10.1002/biot.201700332.

46 I. M. Bernhardsen and H. K. Knuutila, A review of potential amine solvents for CO_2 absorption process: Absorption capacity, cyclic capacity and pKa, *Int. J. Greenh. Gas Control*, 2017, **61**, 27–48.

47 P. V. Danckwerts, The reaction of CO_2 with ethanolamines, *Chem. Eng. Sci.*, 1979, **34**, 443–446.

48 P. D. Vaidya and E. Y. Kenig, CO_2-Alkanolamine Reaction Kinetics: A Review of Recent Studies, *Chem. Eng. Technol.*, 2007, **30**, 1467–1474.

49 E. Jørgensen, C. Faurholt and N. A. Sörensen, Reactions between Carbon Dioxide and Amino Alcohols. II. Triethanolamine, *Acta Chem. Scand.*, 1954, **8**, 1141–1144.

50 J. Benitez-Garcia, G. Ruiz-Ibanez, H. A. Al-Ghawas and O. C. Sandall, On the effect of basicity on the kinetics of CO2 absorption in tertiary amines, *Chem. Eng. Sci.*, 1991, **46**, 2927–2931.

51 H. Guo, C. Li, X. Shi, H. Li and S. Shen, Nonaqueous amine-based absorbents for energy efficient CO2 capture, *Appl. Energy*, 2019, **239**, 725–734.

52 W. M. Budzianowski, Explorative analysis of advanced solvent processes for energy efficient carbon dioxide capture by gas–liquid absorption, *Int. J. Greenh. Gas Control*, 2016, **49**, 108–120.

53 G. Zhang, Y. Yang, G. Xu, K. Zhang and D. Zhang, CO2 capture by chemical absorption in coal-fired power plants: Energy-saving mechanism, proposed methods, and performance analysis, *Int. J. Greenh. Gas Control*, 2015, **39**, 449–462.

54 H. F. Svendsen, E. T. Hessen and T. Mejdell, Carbon dioxide capture by absorption, challenges and possibilities, *Chem. Eng. J.*, 2011, **171**, 718–724.

55 N. Lai, Q. Zhu, D. Qiao, K. Chen, L. Tang, D. Wang, W. He, Y. Chen and T. Yu, CO_2 Capture With Absorbents of Tertiary Amine Functionalized Nano-SiO_2, *Front. Chem.*, 2020, **8**, 146.

56 I. I. Alkhatib, L. M. Pereira, A. AlHajaj and L. F. Vega, Performance of non-aqueous amine hybrid solvents mixtures for CO_2 capture: A study using a molecular-based model, *J. CO2 Util.*, 2020, **35**, 126–144.

57 X. Zhang, Y. Huang, J. Yang, H. Gao, Y. Huang, X. Luo, Z. Liang and P. Tontiwachwuthikul, Amine-based CO_2 capture aided by acid-basic bifunctional catalyst: Advancement of amine regeneration using metal modified MCM-41, *Chem. Eng. J.*, 2020, **383**, 123077.

58 D. Kaufhold, F. Kopf, C. Wolff, S. Beutel, L. Hilterhaus, M. Hoffmann, T. Scheper, M. Schlüter and A. Liese, Reaktive Absorption von Kohlenstoffdioxid in helikalen Hohlfasermembrankontaktoren, *Chem. Ing. Tech.*, 2013, **85**, 476–483.

59 K. Terasaka and S. Fujioka, Applications of Fine Bubble Technology for Industry, Hamburg, 2014.

60 K. Terasaka, A. Hirabayashi, T. Nishino, S. Fujioka and D. Kobayashi, Development of microbubble aerator for waste water treatment using aerobic activated sludge, *Chem. Eng. Sci.*, 2011, **66**, 3172–3179.

61 M. Ughetti, D. Jussen and P. Riedlberger, The ejector loop reactor: Application for microbial fermentation and comparison with a stirred-tank bioreactor, *Eng. Life Sci.*, 2018, **18**, 281–286.

62 H. Tsuge, ed., *Micro- and nanobubbles. Fundamentals and applications*, CRC Press; Pan Stanford Publishing, Boca Raton, FL, 2015.

63 S. L. Al-Dulaimi and A. M. Al-Yaqoobi, Separation of oil/water emulsions by microbubble air flotation, *IOP Conf. Ser. Mater. Sci. Eng.*, 2021, **1076**, 12030.

64 N. A. Kazakis, A. A. Mouza and S. V. Paras, Experimental study of bubble formation at metal porous spargers: Effect of liquid properties and sparger characteristics on the initial bubble size distribution, *Chemical Engineering Journal*, 2008, **137**, 265–281.

65 S. Dey, A. Bhattacharya, P. Kumar and A. Malik, High-rate CO 2 sequestration using a novel venturi integrated photobioreactor and subsequent valorization to microalgal lipids, *Green Chem.*, 2020, **22**, 7962–7973.

66 S. Seo, B. Lages and M. Kim, Catalytic CO2 absorption in an amine solvent using nickel nanoparticles for post-combustion carbon capture, *Journal of CO2 Utilization*, 2020, **36**, 244–252.

67 J.-H. Bang, K. Song, S. Park, C. Jeon, S.-W. Lee and W. Kim, Effects of CO2 Bubble Size, CO2 Flow Rate and Calcium Source on the Size and Specific Surface Area of CaCO3 Particles, *Energies (Basel)*, 2015, **8**, 12304–12313.

68 J. Reardon, T. Bucholz, M. Hulvey, J. Tuttle, A. Shaffer, D. Pulvirenti, L. Weber, K. Killian and A. Zaks, Low Energy CO_2 Capture Enabled by Biocatalyst Delivery System, *Energy Procedia*, 2014, **63**, 301–321.

69 Z. Liang, W. Rongwong, H. Liu, K. Fu, H. Gao, F. Cao, R. Zhang, T. Sema, A. Henni, K. Sumon, D. Nath, D. Gelowitz, W. Srisang, C. Saiwan, A. Benamor, M. Al-Marri, H. Shi, T. Supap, C. Chan, Q. Zhou, M. Abu-Zahra, M. Wilson, W. Olson, R. Idem and P. Tontiwachwuthikul, Recent progress and new developments in post-combustion carbon-capture technology with amine based solvents, *Int. J. Greenh. Gas Control*, 2015, **40**, 26–54.

70 S. M. Benson and T. Surles, Carbon Dioxide Capture and Storage: An Overview With Emphasis on Capture and Storage in Deep Geological Formations, *Proc. IEEE*, 2006, **94**, 1795–1805.

71 B. Smit, *Introduction to carbon capture and sequestration*, Imperial College Press, London, Singapore, 2014.

72 J. Martin, L. Eisoldt and A. Skerra, Fixation of gaseous CO_2 by reversing a decarboxylase for the biocatalytic synthesis of the essential amino acid l-methionine, *Nat. Catal.*, 2018, **1**, 555–561.

73 *US Department of Energy's National Energy Technology Laboratory, Carbon Capture Technology Program Plan 2013*.

74 T. Yoshida, Y. Hayakawa, T. Matsui and T. Nagasawa, Purification and characterization of 2,6-dihydroxybenzoate decarboxylase reversibly catalyzing nonoxidative decarboxylation, *Arch. Microbiol.*, 2004, **181**, 391–397.

75 L. B. Gregory and W. G. Scharmann, Carbon Dioxide Scrubbing by Amine Solutions, *Ind. Eng. Chem.*, 1937, **29**, 514–519.

76 I. C. Tommasi, Carboxylation of Hydroxyaromatic Compounds with HCO_3^- by Enzyme Catalysis: Recent Advances Open the Perspective for Valorization of Lignin-Derived Aromatics, *Catalysts*, 2019, **9**, 37.

77 J. Ren, P. Yao, S. Yu, W. Dong, Q. Chen, J. Feng, Q. Wu and D. Zhu, An Unprecedented Effective Enzymatic Carboxylation of Phenols, *ACS Catal.*, 2016, **6**, 564–567.

78 T. Matsui, T. Yoshida, T. Yoshimura and T. Nagasawa, Regioselective carboxylation of 1,3-dihydroxybenzene by 2,6-dihydroxybenzoate decarboxylase of Pandoraea sp. 12B-2, *Appl. Microbiol. Biotechnol.*, 2006, **73**, 95–102.

79 A. R. Da Lopes Silva, A. Jhones dos Santos and C. A. Martínez-Huitle, Electrochemical measurements and theoretical studies for understanding the behavior of catechol, resorcinol and hydroquinone on the boron doped diamond surface, *RSC Adv.*, 2018, **8**, 3483–3492.

80 C. Ortega-Moo, J. Garza and R. Vargas, The substituent effect on the antioxidant capacity of catechols and resorcinols, *Theor. Chem. Acc.*, 2016, **135**. DOI: 10.1007/s00214-016-1932-7.

81 J. W. Mason and B. F. Dodge, Doctoral dissertation, Yale University, 1936.

82 T. L. Donaldson and Y. N. Nguyen, Carbon Dioxide Reaction Kinetics and Transport in Aqueous Amine Membranes, *Ind. Eng. Chem. Fund.*, 1980, **19**, 260–266.

83 Y. Li and A. E. Mather, Correlation and Prediction of the Solubility of CO_2 and H_2S in Aqueous Solutions of Triethanolamine, *Ind. Eng. Chem. Res.*, 1996, **35**, 4804–4809.

84 F.-Y. Jou, F. D. Otto and A. E. Mather, Equilibria of H_2S and CO_2 in triethanolamine solutions, *Can. J. Chem. Eng.*, 1985, **63**, 122–125.

85 R. L. Kent and B. Elsenberg, Better Data for Amine Treating, *Hydrocarbon Processing*, 1976, **55**, 87–90.

86 A. B. López, M. D. La Rubia, J. M. Navaza, R. Pacheco and D. Gómez-Díaz, Carbon Dioxide Absorption in Triethanolamine Aqueous Solutions: Hydrodynamics and Mass Transfer, *Chem. Eng. Technol.*, 2014, **37**, 419–426.

87 C. B. Andersen, Understanding Carbonate Equilibria by Measuring Alkalinity in Experimental and Natural Systems, *J. Geosci. Educ.*, 2002, **50**, 389–403.

88 L. Pesci, Doctoral dissertation, TUHH Universitätsbibliothek, 2017.

89 T. Matsui, T. Yoshida, T. Hayashi and T. Nagasawa, Purification, characterization, and gene cloning of 4-hydroxybenzoate decarboxylase of Enterobacter cloacae P240, *Arch. Microbiol.*, 2006, **186**, 21–29.

90 X. Zhang, J. Ren, P. Yao, R. Gong, M. Wang, Q. Wu and D. Zhu, Biochemical characterization and substrate profiling of a reversible 2,3-dihydroxybenzoic acid decarboxylase for biocatalytic Kolbe-Schmitt reaction, *Enzyme Microb. Technol.*, 2018, **113**, 37–43.

91 K. J. Laidler and P. S. Bunting, [9] The kinetics of immobilized enzyme systems, in *Isotopic probes and complex enzyme systems*, ed. D. L. Purich, Academic Press, New York, NY, 1980, pp. 227–248.

92 X. Sheng and F. Himo, Theoretical Study of Enzyme Promiscuity: Mechanisms of Hydration and Carboxylation Activities of Phenolic Acid Decarboxylase, *ACS Catal.*, 2017, **7**, 1733–1741.

93 M. Goto, H. Hayashi, I. Miyahara, K. Hirotsu, M. Yoshida and T. Oikawa, Crystal structures of nonoxidative zinc-dependent 2,6-dihydroxybenzoate (gamma-resorcylate) decarboxylase from Rhizobium sp. strain MTP-10005, *J. Biol. Chem.*, 2006, **281**, 34365–34373.

94 C. Wuensch, T. Pavkov-Keller, G. Steinkellner, J. Gross, M. Fuchs, A. Hromic, A. Lyskowski, K. Fauland, K. Gruber, S. M. Glueck and K. Faber, Regioselective Enzymatic β-Carboxylation of para-Hydroxy- styrene Derivatives Catalyzed by Phenolic Acid Decarboxylases, *Adv. Synth. Catal.*, 2015, **357**, 1909–1918.

95 X. Sheng, Y. Patskovsky, A. Vladimirova, J. B. Bonanno, S. C. Almo, F. Himo and F. M. Raushel, Mechanism and Structure of γ-Resorcylate Decarboxylase, *Biochemistry*, 2018, **57**, 3167–3175.

96 X. Sheng, K. Plasch, S. E. Payer, C. Ertl, G. Hofer, W. Keller, S. Braeuer, W. Goessler, S. M. Glueck, F. Himo and K. Faber, Reaction Mechanism and Substrate Specificity of Iso-orotate Decarboxylase: A Combined Theoretical and Experimental Study, *Front. Chem.*, 2018, **6**, 608.

97 X. Sheng, W. Zhu, J. Huddleston, D. F. Xiang, F. M. Raushel, N. G. J. Richards and F. Himo, A Combined Experimental-Theoretical Study of the LigW-Catalyzed Decarboxylation of 5-Carboxyvanillate in the Metabolic Pathway for Lignin Degradation, *ACS Catal.*, 2017, **7**, 4968–4974.

98 L.-E. Meyer, K. Plasch, U. Kragl and J. von Langermann, Adsorbent-Based Downstream-Processing of the Decarboxylase-Based Synthesis of 2,6-Dihydroxy-4-methylbenzoic Acid, *Org. Process Res. Dev.*, 2018, **22**, 963–970.

99 D. Hülsewede, L.-E. Meyer and J. von Langermann, Application of In Situ Product Crystallization and Related Techniques in Biocatalytic Processes, *Chemistry (Weinheim an der Bergstrasse, Germany)*, 2019, **25**, 4871–4884.

100 J. V. Kilmartin and L. Rossi-Bernardi, Inhibition of CO2 combination and reduction of the Bohr effect in haemoglobin chemically modified at its alpha-amino groups, *Nature*, 1969, **222**, 1243–1246.

101 J. V. Kilmartin and L. Rossi-Bernardi, The binding of carbon dioxide by horse haemoglobin, *Biochem. J.*, 1971, **124**, 31–45.

102 J. V. Kilmartin and L. Rossi-Bernardi, Interaction of hemoglobin with hydrogen ions, carbon dioxide, and organic phosphates, *Physiol. Rev.*, 1973, **53**, 836–890.

103 T. J. Andrews, M. R. Badger and G. H. Lorimer, Factors affecting interconversion between kinetic forms of ribulose diphosphate carboxylase-oxygenase from spinach, *Arch. Biochem. Biophys.*, 1975, **171**, 93–103.

104 W. Wallace Cleland, †, T. John Andrews, ‡, Steven Gutteridge, §, Fred C. Hartman, ⊥ and and and George H. Lorimer*, Mechanism of Rubisco: The Carbamate as General Base.

105 G. H. Lorimer, M. R. Badger and T. J. Andrews, The activation of ribulose-1,5-bisphosphate carboxylase by carbon dioxide and magnesium ions. Equilibria, kinetics, a suggested mechanism, and physiological implications, *Biochemistry*, 1976, **15**, 529–536.

106 G. H. Lorimer and H. M. Miziorko, Carbamate formation on the epsilon-amino group of a lysyl residue as the basis for the activation of ribulosebisphosphate carboxylase by CO2 and Mg2+, *Biochemistry*, 1980, **19**, 5321–5328.

107 V. L. Linthwaite, J. M. Janus, A. P. Brown, D. Wong-Pascua, A. C. O'Donoghue, A. Porter, A. Treumann, D. R. W. Hodgson and M. J. Cann, The identification of carbon dioxide mediated protein post-translational modifications, *Nature communications*, 2018, **9**, 3092.

108 A. S. Kertes and C. J. King, Extraction chemistry of fermentation product carboxylic acids, *Biotechnol. Bioeng.*, 1986, **28**, 269–282.

109 C. S. López-Garzón and A. J. J. Straathof, Recovery of carboxylic acids produced by fermentation, *Biotechnology advances*, 2014, 873–904.

110 L.-E. Meyer, K. Plasch, U. Kragl and J. von Langermann, Adsorbent-Based Downstream-Processing of the Decarboxylase-Based Synthesis of 2,6-Dihydroxy-4-methylbenzoic Acid, *Org. Process Res. Dev.*, 2018, **22**, 963–970.

111 H. M. Laun, Rheological properties of aqueous polymer dispersions, *Angew. Makromol. Chem.*, 1984, **123**, 335–359.

112 N. Willenbacher and K. Georgieva, Rheology of Disperse Systems, in *Product design and engineering*, ed. U. Bröckel, W. Meier and G. Wagner, Wiley-VCH, Weinheim, 2013, pp. 7–49.

113 R. L. Gustafson, R. L. Albright, J. Heisler, J. A. Lirio and O. T. Reid, Adsorption of Organic Species by High Surface Area Styrene-Divinylbenzene Copolymers, *Ind. Eng. Chem. Prod. Res. Dev.*, 1968, **7**, 107–115.

114 S. E. Charm and B. L. Wong, Shear effects on enzymes, *Enzyme Microb. Technol.*, 1981, **3**, 111–118.

115 E. D'Imprima, D. Floris, M. Joppe, R. Sánchez, M. Grininger and W. Kühlbrandt, *Protein denaturation at the air-water interface and how to prevent it*, 2019.

116 A. Staby, I. H. Jensen and I. Mollerup, Comparison of chromatographic ion-exchange resins, *J. Chromatogr. A*, 2000, **897**, 99–111.

117 A. S. Bommarius and M. F. Paye, Stabilizing biocatalysts, *Chemical Society reviews*, 2013, **42**, 6534–6565.

118 M. Dias Gomes and J. M. Woodley, Considerations when Measuring Biocatalyst Performance, *Molecules*, 2019, **24**, 3573.

119 P. Tufvesson, J. Lima-Ramos, M. Nordblad and J. M. Woodley, Guidelines and Cost Analysis for Catalyst Production in Biocatalytic Processes, *Org. Process Res. Dev.*, 2011, **15**, 266–274.

120 R. Schäfer, C. Merten and G. Eigenberger, Bubble size distributions in a bubble column reactor under industrial conditions, *Exp. Therm. Fluid Sci.*, 2002, **26**, 595–604.

121 A. A. Mouza, G. K. Dalakoglou and S. V. Paras, Effect of liquid properties on the performance of bubble column reactors with fine pore spargers, *Chemical Engineering Science*, 2005, **60**, 1465–1475.

122 M. Iwakiri, K. Terasaka, S. Fujioka, M. Schlüter, S. Kastens and S. Tanaka, Mass Transfer from a Shrinking Single Microbubble Rising in Water, *Japanese J. Multiphase Flow*, 2017, **30**, 529–535.

123 P. W. Atkins, J. de Paula and M. Bär, *Physikalische Chemie*, Wiley-VCH Verl., Weinheim, 5th edn., 2013.

124 P. S. Epstein and M. S. Plesset, On the Stability of Gas Bubbles in Liquid-Gas Solutions, *J. Chem. Phys.*, 1950, **18**, 1505–1509.

125 S. Tanaka, S. Kastens, S. Fujioka, M. Schlüter and K. Terasaka, Mass transfer from freely rising microbubbles in aqueous solutions of surfactant or salt, *Chemical Engineering Journal*, 2020, **387**, 121246.

126 S. Matthes, B. Thomas, D. Ohde, M. Hoffmann, P. Bubenheim, A. Liese, S. Tanaka, K. Terasaka and M. Schlueter, Hydrodynamic and Mass Transfer Correlation in a Microbubble Aerated Stirred Tank Reactor, *J. Chem. Eng. Jpn.*, 2020, **53**, 577–584.

127 F. Y. Ushikubo, M. Enari, T. Furukawa, R. Nakagawa, Y. Makino, Y. Kawagoe and S. Oshita, Zeta-potential of Micro- and/or Nano-bubbles in Water Produced by Some Kinds of Gases, *IFAC Proceedings Volumes*, 2010, **43**, 283–288.

128 M. Takahashi, Zeta potential of microbubbles in aqueous solutions: electrical properties of the gas-water interface, *The journal of physical chemistry. B*, 2005, **109**, 21858–21864.

129 Hideki Tsuge, Characteristics of Microbubbles, in *Micro- and nanobubbles*, ed. H. Tsuge, CRC Press; Pan Stanford Publishing, Boca Raton, FL, 2015, pp. 3–10.

130 A. Prins and K. van't Riet, Proteins and surface effects in fermentation: foam, antifoam and mass transfer, *Trends Biotechnol.*, 1987, **5**, 296–301.

131 B. Thomas, D. Ohde, S. Matthes, C. Engelmann, P. Bubenheim, K. Terasaka, M. Schlüter and A. Liese, Comparative investigation of fine bubble and macrobubble aeration on gas utility and biotransformation productivity, *Biotechnology and bioengineering*, 2021, **118**, 130–141.

132 L. Parkinson, R. Sedev, D. Fornasiero and J. Ralston, The terminal rise velocity of 10-100 microm diameter bubbles in water, *Journal of colloid and interface science*, 2008, **322**, 168–172.

133 G. G. Stokes, *On the effect of the internal friction of fluids on the motion of pendulums*, Pitt Press Cambridge, 1851.

134 J. S. Hadamard, Mouvement permanent lent d'une sphère liquid et visqueuse dans un liquide visqueux, *CR Hebd. Seances Acad. Sci. Paris*, 1911, **152**, 1735–1738.

135 W. Rybczynski, On the translatory motion of a fluid sphere in a viscous medium, *Bull. Acad. Sci., Cracow, Series A*, 1911, **40**, 33–78.

136 N. A. Kazakis, A. A. Mouza and S. V. Paras, Coalescence during bubble formation at two neighbouring pores: An experimental study in microscopic scale, *Chem. Eng. Sci.*, 2008, **63**, 5160–5178.

137 N. Räbiger, M. Schlüter, A. Mersmann, H. D. Dahl, A. Luke, P. Walzel and E. Musemic, L4 Blasen und Tropfen in technischen Apparaten, in *VDI-Wärmeatlas*, Springer Vieweg, Berlin, Heidelberg, 2013, pp. 1413–1458.

138 Y. Maham, C.-N. Liew and A. E. Mather, Viscosities and Excess Properties of Aqueous Solutions of Ethanolamines from 25 to 80°C, *J. Solution Chem.*, 2002, **31**, 743–756.

139 P. Snabre and F. Magnifotcham, I. Formation and rise of a bubble stream in a viscous liquid, *Eur. Phys. J. B*, 1998, **4**, 369–377.

140 G. Besagni, F. Inzoli, G. de Guido and L. A. Pellegrini, The dual effect of viscosity on bubble column hydrodynamics, *Chemical Engineering Science*, 2017, **158**, 509–538.

141 Z. Najmi, G. Ebrahimipour, A. Franzetti and I. M. Banat, In situ downstream strategies for cost-effective bio/surfactant recovery, *Biotechnol. Appl. Biochem.*, 2018, **65**, 523–532.

142 F. C. Boogerd, P. Bos, J. G. Kuenen, J. J. Heijnen and R. G. van der Lans, Oxygen and carbon dioxide mass transfer and the aerobic, autotrophic cultivation

of moderate and extreme thermophiles: a case study related to the microbial desulfurization of coal, *Biotechnology and bioengineering*, 1990, **35**, 1111–1119.

143 P. N. C. Royce and N. F. Thornhill, Estimation of dissolved carbon dioxide concentrations in aerobic fermentations, *AIChE J.*, 1991, **37**, 1680–1686.

144 P. Talbot, M. P. Gortares, R. W. Lencki and J. de La Noüe, Absorption of CO_2 in algal mass culture systems: a different characterization approach, *Biotechnology and bioengineering*, 1991, **37**, 834–842.

145 Y. Liu, H. A. Li and R. Okuno, Measurements and Modeling of Interfacial Tension for CO 2 /CH 4 /Brine Systems under Reservoir Conditions, *Ind. Eng. Chem. Res.*, 2016, **55**, 12358–12375.

146 E. L. Cussler, *Diffusion. Mass transfer in fluid systems*, Cambridge Univ. Press, Cambridge, 3rd edn., 2009.

147 R. Sander, Compilation of Henry's law constants (version 4.0) for water as solvent, *Atmos. Chem. Phys.*, 2015, **15**, 4399–4981.

148 I. H. Lehrer, Gas Hold-Up and Interfacial Area in Sparged Vessels, *Ind. Eng. Chem. Process Des. Dev.*, 1971, **10**, 37–40.

149 B. Thitakamol and A. Veawab, Foaming Behavior in CO_2 Absorption Process Using Aqueous Solutions of Single and Blended Alkanolamines, *Ind. Eng. Chem. Res.*, 2008, **47**, 216–225.

150 B. Thitakamol, A. Veawab and A. Aroonwilas, Foaming in amine-based CO_2 capture process: Experiment, modeling and simulation, *Energy Procedia*, 2009, **1**, 1381–1386.

151 Y. Cho and J. Laskowski, Effect of flotation frothers on bubble size and foam stability, *Int. J. Miner. Process.*, 2002, **64**, 69–80.

152 G. L. Collins, M. Motarjemi and G. J. Jameson, A method for measuring the charge on small gas bubbles, *Journal of colloid and interface science*, 1978, **63**, 69–75.

153 C. Oliveira and J. Rubio, Zeta potential of single and polymer-coated microbubbles using an adapted microelectrophoresis technique, *Int. J. Miner. Process.*, 2011, **98**, 118–123.

154 W. Huo, X. Zhang, K. Gan, Y. Chen, J. Xu and J. Yang, Effect of zeta potential on properties of foamed colloidal suspension, *J. Eur. Ceram. Soc.*, 2019, **39**, 574–583.

155 A. S. Bommarius and A. Karau, Deactivation of formate dehydrogenase (FDH) in solution and at gas-liquid interfaces, *Biotechnol. Prog.*, 2005, **21**, 1663–1672.

156 S. Bhagia, R. Dhir, R. Kumar and C. E. Wyman, Deactivation of Cellulase at the Air-Liquid Interface Is the Main Cause of Incomplete Cellulose Conversion at Low Enzyme Loadings, *Scientific reports*, 2018, **8**, 1350.

157 R. Gehle, Protein recovery by continuous flotation, *Appl Microbiol Biotechnol*, 1984, **20**. DOI: 10.1007/BF00252591.

158 M. Stieß, *Mechanische Verfahrenstechnik 1*, Springer, Berlin, Heidelberg, 1995.

159 M. Ali, H. M. Ishqi and Q. Husain, Enzyme engineering: Reshaping the biocatalytic functions, *Biotechnology and bioengineering*, 2020, **117**, 1877–1894.

160 M. Miyazaki, M. Shibue, K. Ogino, H. Nakamura and H. Maeda, Enzymatic synthesis of pyruvic acid from acetaldehyde and carbon dioxide, *Chem. Commun.*, 2001, 1800–1801.

161 M. Miyazaki, K. Ogino, M. Shibue, H. Nakamura and H. Maeda, A One-Pot, Two-Step Enzymatic Synthesis of L-Lactic Acid from Acetaldehyde, *Chem. Lett.*, 2002, **31**, 758–759.

162 M. Wieser, T. Yoshida and T. Nagasawa, Carbon dioxide fixation by reversible pyrrole-2-carboxylate decarboxylase and its application, *J. Mol. Catal., B Enzym.*, 2001, **11**, 179–184.

163 M. Wieser, N. Fujii, T. Yoshida and T. Nagasawa, Carbon dioxide fixation by reversible pyrrole-2-carboxylate decarboxylase from Bacillus megaterium PYR2910, *Eur. J. Biochem.*, 1998, **257**, 495–499.

164 T. Yoshida, K. Fujita and T. Nagasawa, Novel reversible indole-3-carboxylate decarboxylase catalyzing nonoxidative decarboxylation, *Bioscience, biotechnology, and biochemistry*, 2002, **66**, 2388–2394.

165 S. M. Glueck, S. Gümüs, W. M. F. Fabian and K. Faber, Biocatalytic carboxylation, *Chemical Society reviews*, 2010, **39**, 313–328.

166 G. Bertani, Studies on lysogenesis. I. The mode of phage liberation by lysogenic Escherichia coli, *J. Bacteriol.*, 1951, **62**, 293–300.

167 S. Hackbusch, N. Noirungsee, J. Viamonte, X. Sun, P. Bubenheim, J. E. Kostka, R. Müller and A. Liese, Influence of pressure and dispersant on oil biodegradation by a newly isolated Rhodococcus strain from deep-sea sediments of the gulf of Mexico, *Mar. Pollut. Bull.*, 2020, **150**, 110683.

168 L. A. Tribe, C. L. Briens and A. Margaritis, Determination of the volumetric mass transfer coefficient (k_La) using the dynamic "gas out-gas in" method: Analysis of errors caused by dissolved oxygen probes, *Biotechnol. Bioeng.*, 1995, **46**, 388–392.

169 J. U. Keller and R. Staudt, *Gas adsorption equilibria. Experimental methods and adsorptive isotherms*, Springer, New York, 2005.

170 P. W. Atkins, *Physical chemistry*, Oxford Univ. Press, Oxford, 6th edn., 2001.

171 J. A. V. Butler and C. Ockrent, Adsorption from Solutions containing Two Solutes, *Nature*, 1930, **125**, 853–854.

172 J. S. Jain and V. L. Snoeyink, Adsorption from Bisolute Systems on Active Carbon, *J. Water Pollut. Control Fed.*, 1973, **45**, 2463–2479.

173 F. A. Digiano, G. Baldauf, B. Frick and H. Sontheimer, A simplified competitive equilibrium adsorption model, *Chem. Eng. Sci.*, 1978, **33**, 1667–1673.

174 C. Sheindorf, M. Rebhun and M. Sheintuch, A Freundlich-type multicomponent isotherm, *J. Colloid Interface Sci.*, 1981, **79**, 136–142.

175 M. Jaroniec and J. Töth, Adsorption of gas mixtures on heterogeneous solid surfaces: I. Extension of Tóth isotherm on adsorption from gas mixtures, *Colloid Polym. Sci.*, 1976, **254**, 643–649.

176 W. Fritz and E.-U. Schluender, Simultaneous adsorption equilibria of organic solutes in dilute aqueous solutions on activated carbon, *Chemical Engineering Science*, 1974, **29**, 1279–1282.

8. Appendix

Matlab Script for Dissolution of Bubbles:

```
clc; clear;
%% single microbubble mass transfer
%Date modified: 2020/12/11
FileName = input('Input file name:','s');%

%% Constants
R = 8.314; %Ideal gas constant [J K/mol]
g = 9.81; %Gravitatinal acceleration [m/s2]
Patm = 1.013*10^5; %Atmospheric pressure [Pa]
T = 30 + 273.15; %Temperature [K]
gamma = 62.8*10^-3; %Surface tension [N/m] (G. Vázquez, E. Alvarez, R. Rendo, E. Romero, J. M. Navaza, J. Chem. Eng. Data 1996, 41, 806.)
mu = 1.2659*10^-3; %Dynamic Viscosity [Pa s] (J.-J. Ko, T.-C. Tsai, C.-Y. Lin, H.-M. Wang, M.-H. Li, J. Chem. Eng. Data 2001, 46, 160.)
rho = 1018.2; %Liquid density [kg/m3] (J.-J. Ko, T.-C. Tsai, C.-Y. Lin, H.-M. Wang, M.-H. Li, J. Chem. Eng. Data 2001, 46, 160.)
h = 0.152; % Reactor height [m] (0.116 = Distance between surface and Sopat / 0.152 = Distance between top of sparger and surface)

%Henry's constant H [mol/m3/Pa] Sander, 2015
H(1) = 1.2*10^-5; %O2 1.2E-5
H(2) = 6.4*10^-6; %N2 6.4E-6
H(3) = 3.46*10^-4; %CO2 3.4E-4 (P. V. Danckwerts, The Chemical Engineer 1966, 244.)
%Diffusion coefficient D [m2/s] 1964_Himmelblau_Diffusion of dissolved gases in liquids
```

```
D(1) = 2.2*10^-9; %O2
D(2) = 2.0*10^-9; %N2
D(3) = 1.14*10^-9; %CO2 (water: 1.9*10^-9) (J.-J. Ko, T.-C. Tsai, C.-Y. Lin, H.-M. Wang, M.-H. Li, J. Chem. Eng. Data 2001, 46, 160.)
%% Initial dissolved gas concentration
S = 1; %Saturation ratio [-]
y(1) = 0; %0.21; %Oxygen: O2. Ex. Air; 0.21
y(2) = 0; %0.79; %Nitrogen: N2. Ex. Air:0.79
y(3) = 1; %Carbon dioxide: CO2. Ex. CO2: 0.0004
Cbulk(1) = H(1)*y(1)*(Patm+rho*g*h)*S;
Cbulk(2) = H(2)*y(2)*(Patm+rho*g*h)*S;
Cbulk(3) = H(3)*y(3)*(Patm+rho*g*h)*S;
DO = Cbulk(1)*32; DN = Cbulk(2)*28;

%% Time step & simulated duration
dt = 0.01; %Time step [s]
tMax = 300; %Total duration of simulated time [s]
CalMax = tMax/dt;

%% Initial bubble diameterdB = zeros(1,CalMax);
dB(1) = 140*10^-6;%Initial bubble diameter [m]

%% Mole fraction of the gas in the microbubble
yB = zeros(3,CalMax);
Bubble = 'CO2'; %Gas in the bubble Ex. Air, N2, O2, CO2
yB(1,1)= 0; %Oxygen Ex. Air: 0.21vol% O2
yB(2,1)= 0; %Nitorogen Air: 0.79vol% N2
yB(3,1)= 1; %Carbon dioxide
```

```
%% Set Functions
PB = @(dB) Patm + rho * g * h + (4 * gamma./dB); %bubble pressure
uB = @(dB) rho*g*dB.^2/(18*mu); %Rising velocity of bubble
nB = @(dB) PB(dB)*(pi * dB^3)/(6* R * T); %Mole of the gas(es) in the bubble
Re = @(dB) dB*uB(dB) * rho/mu; %Reynolds number
Sc = @(D) mu/rho/D;
Sh = @(dB,D) 2 + 0.6*(Re(dB))^(1/2)*Sc(D)^(1/3); %Ranz-Marshall's equation
kL = @(dB,D) Sh(dB,D)*D/dB;
A = @(dB) pi*dB^2; %Surface area of the bubble
dn =@(dB,D,Y,H,C) kL(dB,D)*A(dB)*(Y*H*PB(dB)-C)*dt; %Dissolving amout of gas

%% for roop: Runge-Kutta 4th order method
for i = 1:CalMax
    d = dB(i); y1 = yB(1,i); y2 = yB(2,i); y3 = yB(3,i);
    k1(1)=dn(d,D(1),y1,H(1),Cbulk(1)); %O2
    k1(2)=dn(d,D(2),y2,H(2),Cbulk(2)); %N2
    k1(3)=dn(d,D(3),y3,H(3),Cbulk(3)); %CO2
    dB1(i)=(6*(nB(d)-(k1(1)+k1(2)+k1(3)))*R*T/pi/PB(d))^(1/3); %

    k2(1)=dn(dB1(i),D(1),y1,H(1),Cbulk(1));%O2
    k2(2)=dn(dB1(i),D(2),y2,H(2),Cbulk(2));%N2
    k2(3)=dn(dB1(i),D(3),y3,H(3),Cbulk(3));%CO2
    dB2(i)=(6*(nB(d)-(k2(1)+k2(2)+k2(3))/2)*R*T/pi/PB(d))^(1/3); %

    k3(1)=dn(dB2(i),D(1),y1,H(1),Cbulk(1));%O2
    k3(2)=dn(dB2(i),D(2),y2,H(2),Cbulk(2));%N2
    k3(3)=dn(dB2(i),D(3),y3,H(3),Cbulk(3));%CO2
```

```
    dB3(i)=(6*(nB(d)-(k3(1)+k3(2)+k3(3))/2)*R*T/pi/PB(d))^(1/3);

    k4(1)=dn(dB3(i),D(1),yB(1,i),H(1),Cbulk(1));
    k4(2)=dn(dB3(i),D(2),yB(2,i),H(2),Cbulk(2));
    k4(3)=dn(dB3(i),D(3),yB(3,i),H(3),Cbulk(3));

    %Calculate the mole of each gase
    n(1,i) = nB(d)*y1-(k1(1)+2*k2(1)+2*k3(1)+k4(1))/6;
    n(2,i) = nB(d)*y2-(k1(2)+2*k2(2)+2*k3(2)+k4(2))/6;
    n(3,i) = nB(d)*y3-(k1(3)+2*k2(3)+2*k3(3)+k4(3))/6;
    ntotal = n(1,i)+n(2,i)+n(3,i); %Mole of the MB(i+1)

    %Calculate the mole fraction and diameter
    y1 = n(1,i)/ntotal; y2 = n(2,i)/ntotal; y3 = n(3,i)/ntotal;
    dB(i+1) = (6*(ntotal)*R*T/pi/PB(d))^(1/3);
    yB(1,i+1) = y1; yB(2,i+1) = y2; yB(3,i+1) = y3;

    if ntotal < 0 || i == CalMax
        dfin = d;
        break
    else
        continue
    end
end
%% Plot results
t = 0:dt:i*dt; % generate time vector
FontSize = 14;
tfin = t(i);
```

```
tlim = tfin*1.1; %XŽ²"Time",Ì”CˆÓ,Ì�Å‘å’l[s]

%% Diameter vs time
figure
plot(t,dB(1:i+1)*1e+6,'LineWidth',2);xlim([0 tlim]); ylim([0 dB(1)*10^6*1.2]);
xlabel('Time [s]','FontSize',FontSize);
ylabel('Diameter [\mum]','FontSize',FontSize);
ax = gca; ax.FontSize = FontSize; ax.LineWidth = 2; ax.TickLength = [0.02 0.035];
str = {[num2str(Bubble) '-MB'],['Bulk DO: ',num2str(round(DO,1)), ' mg/L'],...
    ['Bulk DN: ',num2str(round(DN,1)), ' mg/L'],['Saturation ratio = ',num2str(S)],...
    ['Dissolution time \tau = ', num2str(round(tfin,1)), ' s']};
TextX = tfin*3/5; TextY = dB(1)*9/10*10^6; text(TextX,TextY,str,'FontSize',12);
saveas(gcf,[num2str(Bubble),'-bubble_Diameter.png']);%Set view and save figure
writematrix([t(1:1/dt:i+1).' dB(1:1/dt:i+1).'],[num2str(FileName),'-Diameter.csv'])

%% Position vs time
figure;
Pos = 0;
u = uB(dB(1:i+1));
for p =1:length(t)-1
    Pos(p+1) = Pos(p)+u(p)*dt;
end
plot(t,Pos,'LineWidth',2);%ylim([0 PB(1)*10^6*1.1]);
xlim([0 tlim]);
xlabel('Time [s]','FontSize',FontSize);
ylabel('Position [m]','FontSize',FontSize);
ax = gca; ax.FontSize = FontSize; ax.LineWidth = 2; ax.TickLength = [0.02 0.035];
saveas(gcf,[num2str(Bubble),'-bubble_Position.png']);%Set view and save figure
```

```
%writematrix([t(1:1/dt:i+1).' Pos(1:1/dt:i+1).'],[num2str(FileName),'-Position.csv'])
%% Mole fraction vs time
figure
plot(t,yB(1,1:i+1),'LineWidth',2);xlim([0 tlim]);ylim([0 1]); hold on
plot(t,yB(2,1:i+1),'--','LineWidth',2); hold on
plot(t,yB(3,1:i+1),':','LineWidth',2);
xlabel('Time [s]','FontSize',FontSize); ylabel('Mole fraction [-]','FontSize',FontSize);
ax = gca; ax.FontSize = FontSize; ax.LineWidth = 2; ax.TickLength = [0.02 0.035];
legend({'O2','N2','CO2'},'Location','best');
saveas(gcf,[num2str(Bubble),'-bubble_MoleFraction.png']);%Set view and save figure
hold off
writematrix([t(1:1/dt:i+1).' yB(1,1:1/dt:i+1).'...
    yB(2,1:1/dt:i+1).' yB(3,1:1/dt:i+1).'],[num2str(FileName),'-MoleFraction.csv'])
%% Output
```